Finite element analysis of hot rolling processes

O. Soto
E. Oñate
R. Codina

Publicación CIMNE Nº 40, Octubre 1993

Finite element analysis of hot rolling processes

O. Soto
E. Oñate
R. Codina

Publicación CIMNE Nº 40, Octubre 1993

Centro Internacional de Métodos Numéricos en Ingeniería
Gran Capitán s/n, 08034 Barcelona, España

Index

NOTATION AND MAIN VARIABLES

In all the work we use Einstein's notation (index summation convention). The vectorial or tensorial continuous fields are denoted by boldface characters, otherwise, their components are denoted in normal characters. The main variables and other mathematical conventions are listed below.

$\boldsymbol{\sigma}$: Stress tensor

p: Pressure, defined as $p = \frac{-\sigma_{kk}}{3}$

$\boldsymbol{\tau}$: Deviatoric stress tensor defined as $\boldsymbol{\tau} = \boldsymbol{\sigma} + p\mathbf{I}$

$\mathbf{I}$: Identity tensor

$\mathbf{u}$: Velocity vector

$\mathbf{s}$: Displacement vector

$\boldsymbol{\varepsilon}$: Material strain tensor

$\dot{\boldsymbol{\varepsilon}}$: Strain rate tensor

(a, b): L^2 internal product defined as $\int_\Omega a \cdot b \, d\Omega$

$L^2(\Omega)$: Space of square integrable functions over domain Ω

$H^m(\Omega)$: Sobolev space of functions whose distributional derivates of order up to m belong to $L^2(\Omega)$

$H_0^m(\Omega)$: Space of functions belonging to $H^m(\Omega)$ with zero trace on the boundary $\partial\Omega$

F_h: Discrete element finite space associated to the continuous space F, such that $F_h = \{f \in F|, \ f|_{\Omega^e} \in P_m(\Omega^e)\}$

Ω^e: Finite element partition of Ω

$P_m(\Omega^e)$: Set of complete polynomials of degree m in Ω^e

∇: Gradient operator

ε: Simmetric gradient operator defined as: $\varepsilon(\cdot) = \frac{1}{2}(\nabla(\cdot) + (\cdot)\nabla)$

The rest of the notation is explained in the text.

1. INTRODUCTION

The numerical simulation of hot rolling forming processes is very important for the metallurgic industry. This is an eficient and economic tool to simulate the rolling process and to predict the evolution of some parameters like the velocity field, temperatures, strains, stresses and rolling forces. In this way, computer simulations are becoming a necessary tool in the design and optimization of hot rolling processes [2,3,4,5,21,25,26,27].

In this publication an incompresible flow based formulation to simulate hot rolling processes is presented. First, some theorical aspects about the process are shown as well as numerical solution using the finite element method. Finally, some numerical examples are presented.

2. THEORICAL ASPECTS ABOUT THE HOT ROLLING PROCESS

In this section the continuous thermomechanical equations that describe the roll process are presented. Some important aspects like the treatment of free surface and friction effects are discussed in more detail.

2.1 Thermomechanical coupled problem

The hot rolling process is a non-linear complex problem, in the sense that the equilibrium and energy equations are coupled through the constitutive law as it will be described below. Also, it will be shown the analogy with incompresible fluid flow which arises from the constitutive law.

2.1.1 Equilibrium equation

Let Ω be open and bounded domain of $\mathbb{R}^{nd}$ (nd =2 or 3) occupied by a continuous medium. The differential equation describing the dynamical equilibrium of the continuoum is [1]:

$$\nabla \cdot \boldsymbol{\sigma} + \rho\ \mathbf{b} = \rho \frac{d\mathbf{u}}{dt} \text{ in } \Omega \times (0, t_f) \qquad (1a)$$

with boundary and initial conditions:

$$\begin{aligned} \mathbf{u} &= \overline{\mathbf{u}} \text{ on } \Gamma_u \times (0,t_f) \\ \mathbf{n}\cdot\boldsymbol{\sigma} &= \overline{\boldsymbol{\sigma}} \text{ on } \Gamma_\sigma \times (0,t_f) \\ \mathbf{u}(\mathbf{x},0) &= \mathbf{u}^0(\mathbf{x}) \text{ in } \Omega \times \{0\} \end{aligned} \tag{1b}$$

In above $(0,t_f)$ is a time interval; $\Gamma_u = \{\mathbf{x} \in \partial\Omega | \mathbf{u}(\mathbf{x},t) = \overline{\mathbf{u}}(\mathbf{x},t)\ \forall t \in (0,t_f)\}$, where $\overline{\mathbf{u}}(\mathbf{x},t)$ is a given function; $\Gamma_\sigma = \{\mathbf{x} \in \partial\Omega | (\mathbf{n}\cdot\boldsymbol{\sigma}) = \overline{\boldsymbol{\sigma}}(\mathbf{x},t)\ \forall t \in (0,t_f)\}$ $\overline{\boldsymbol{\sigma}}(\mathbf{x},t)$ is a given function; $\overline{\Gamma_\sigma \bigcup \Gamma_u} = \partial\Omega$ and $\Gamma_\sigma \bigcap \Gamma_u = \emptyset$; $\mathbf{u}^0(\mathbf{x})$ is the given initial velocity field; ρ is the density; $\mathbf{u}$ the velocity field; $\boldsymbol{\sigma}$ the stress field; $\mathbf{b}$ the volumetric forces; $\mathbf{n}$ is the unit exterior normal to Ω and $\partial\Omega$ its contours.

2.1.2 Constitutive law for metals at high temperatures

The physical properties of metals at high temperatures depend basically of the strain, strain rate and temperature fields [2,3]. The strain of metals can be descomposed in two parts, one elastic ε^e and one viscoplastic ε^{vp} as follows:

$$\varepsilon = \varepsilon^e + \varepsilon^{vp} \tag{2}$$

In rolling processes, the elastic strain is much smaller than the viscoplastic or creep strain and it can be neglected [4,5]. The viscoplastic strains are given by a constitutive law which defines the strain rate as follows [4,5,6] :

$$\dot{\varepsilon}_{ij}^{vp} = \gamma\langle\phi(F)\rangle\frac{\partial Q}{\partial\sigma_{ij}} \tag{3}$$

where F is the yield function for the material, Q the plastic potential, ϕ a certain function that defines the model and $\langle\cdot\rangle$ is the Macauley bracket, defined by $\langle f\rangle = f$ if $f \geq 0$ and $\langle f\rangle = 0$ if $f < 0$. The constant γ is the fluidity parameter ($\gamma = 0$ describes ideal plasticity, see Figure 1 below). The function ϕ can be chosen to be of power type without lost of generality [4,5,6].

For the yield surface description we take the Von Mises criterium and assume associate plasticity, i.e.

$$F = Q = \bar{\sigma} - \sigma_y = \sqrt{3}\sqrt{J_2} - \sigma_y \tag{4}$$

where J_2 is the second invariant of the deviatoric stress tensor defined as:

$$J_2 = \frac{1}{2}\tau_{ij}\tau_{ij} \tag{5}$$

The yield stress σ_y is a function of the material temperature, strain and strain rate. For high temperature conditions, the following expressions have been implemented in this work [2,3,6]:

•*Hajduk model*

$$\sigma_y = K_0 \; K_T \; K_\varepsilon \; K_{\dot{\varepsilon}} \tag{6}$$

where

$$K_T = A_1 \exp(-m_1 T)$$
$$K_\varepsilon = A_2 \; (\overline{\varepsilon} + \overline{\varepsilon}_0)^{m_2}$$
$$K_{\dot{\varepsilon}} = A_3 \; \dot{\overline{\varepsilon}}^{m_3}$$

parameters A_1, A_2, A_3 and m_1, m_2, m_3 are common for a particular group of metals while K_0 varies according to the material composition [2]. T is the temperature in Kelvin degrees, $\overline{\varepsilon}$ is the equivalent strain defined as:

$$\overline{\varepsilon} = \sqrt{\frac{2}{3}\varepsilon_{ij}\varepsilon_{ij}} \tag{7}$$

and $\overline{\varepsilon}_0$ has the physical meaning of an initial equivalent strain which gives minimum value of σ_y for the case $\overline{\varepsilon} = 0$. $\dot{\overline{\varepsilon}}$ is the equivalent strain rate defined as:

$$\dot{\overline{\varepsilon}} = \sqrt{\frac{2}{3}\dot{\varepsilon}_{ij}\dot{\varepsilon}_{ij}} \tag{8}$$

Values of the K_0, A_1, m_1, A_2, m_2, A_3, m_3 for some materials can be found in [2].

•*Sellars-Tegart model*

Sellars and Tegart proposed for the interpolation of high temperature data:

$$Z = \dot{\overline{\varepsilon}} \exp(\frac{Q}{RT}) = C[\sinh(\alpha\sigma_y)]^n \tag{9}$$

where Z is the Zener-Hollomon parameter, Q is an activation energy usually independent of temperature and in many case also independent of strain. From (9) σ_y is obtained as:

$$\sigma_y = \frac{1}{\alpha}\log\left[\left(\frac{Z}{C}\right)^{\frac{1}{n}} + \sqrt{\left(\frac{Z}{C}\right)^{\frac{2}{n}} + 1}\right] \tag{10}$$

This equation is strain independent, therefore it is valid only for high strain rate. Values of α, n and C for different materials can be found in [2,5,7].

•*Sellars-Tegart modified model*

This model is obtained taking (9) as [3]:

$$Z = \dot{\bar{\varepsilon}} \exp(\frac{Q}{RT}) = C \exp(\alpha \sigma_y) \tag{11}$$

then,

$$\sigma_y = D \log(Z) - B \tag{12}$$

D, B and Q are strain dependent and some values can be found in reference [3]. This equation is valid for $0.5 < \dot{\bar{\varepsilon}} < 650\ s^{-1}$.

Combining equations (3), (4) and (5), the constitutive law can be rewritten as:

$$\dot{\varepsilon}_{ij} = \gamma < (\sqrt{3}\sqrt{J_2} - \sigma_y)^n > \frac{\sqrt{3}}{2\sqrt{J_2}} \tau_{ij} \tag{13}$$

Taking in account that τ_{ij} are the deviatoric stress tensor components, the volumetric strain rate is zero:

$$\dot{\varepsilon}_{ii} = 0 \tag{14}$$

Finally, from the deviatoric stress definition ($\tau_{ij} = \sigma_{ij} + p\ \delta_{ij}$) and after some mathematical manipulations, the constitutive equation can be rewritten as:

$$\sigma_{ij} = -p\ \delta_{ij} + \frac{2\sqrt{J_2}}{\gamma < (\sqrt{3}\sqrt{J_2} - \sigma_y)^n > \sqrt{3}}\ \dot{\varepsilon}_{ij} \tag{15}$$

2.1.3 Incompressible flow analogy

The constitutive law of a Newtonian fluid is [1,8]:

$$\sigma_{ij} = -p\ \delta_{ij} + \lambda \dot{\varepsilon}_{ii} + 2\mu \dot{\varepsilon}_{ij} \tag{16}$$

in addition, if we impose fluid incompressibility:

$$\dot{\varepsilon}_{ii} = \nabla \cdot \mathbf{u} = 0 \tag{17}$$

(16) is rewritten as:

$$\sigma_{ij} = -p\ \delta_{ij} + 2\mu \dot{\varepsilon}_{ij} \tag{18}$$

Comparing (15) with (18), the constitutive law of an incompressible fluid is equal to the constitutive law of a viscoplastic material taking for the fluid the following non-Newtonian viscosity (from (5), (15), (18), replacing $\tau_{ij} = 2\mu\dot{\varepsilon}_{ij}$ and assuming that $(\sqrt{3}\sqrt{J_2} - \sigma_y)^n > 0$):

$$\mu = \frac{\sigma_y + (\dot{\bar{\varepsilon}}/3\gamma)^{\frac{1}{n}}}{3\dot{\bar{\varepsilon}}} \tag{19}$$

the assumption $(\sqrt{3}\sqrt{J_2} - \sigma_y)^n > 0$ implies that the material is always over the yield surface and $\sigma_{ij} < \infty$, which is realistic in hot rolling processes. In addition, the incompressibility condition is imposed in both problems (equations (14) and (17)). In conclusion, the constitutive behaviour of incompressible non-Newtonian fluids and viscoplastic materials is analogous.

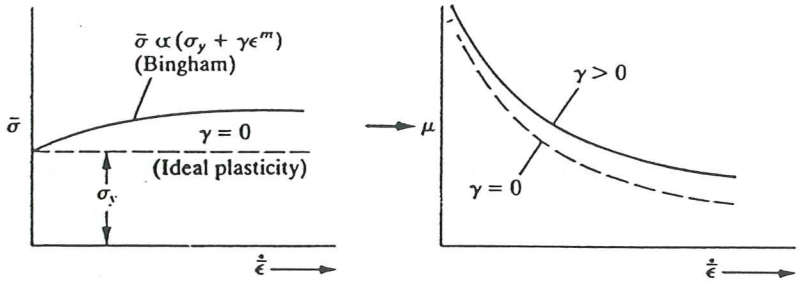

Figure 1 Relationship among strain rate, stress and viscosity for viscoplastic materials [20]

As a final remark, (19) is only valid for high strain rates (material over the yield surface). Figure 1 shows graphically the constitutive behaviour for this type of materials.

2.1.4 Incompressible flow or Stokes equations

Replacing the constitutive law for an incompresible flow (18) (or for a viscoplastic material) into the equilibrium equation (1a) and assuming that the inertial forces can be neglected (i.e. viscous dominated flow which is obvious in hot rolling problems) the equilibrium equation for a viscoplastic material can be rewritten as (in an Eulerian system):

$$\rho\frac{\partial \mathbf{u}}{\partial t} + \nabla p - \nabla \cdot \Big(2\mu\, \varepsilon(\mathbf{u})\Big) = \rho \mathbf{b} \text{ in } \Omega \times (0, t_f) \tag{20}$$

with the boundary and initial conditions given in equation (1b).

This equation together with the incompressibility constraint should to be solved to find the velocity field of hot rolled material, and then, by means of the constitutive law (equations (18) and (19)), the stress field can be obtained. However, the viscosity of the material depends not only on the velocity field, but also on the temperature and displacement fields (see equations (6), (10), (12) and (19)). Therefore, the velocity field must be solved coupled with the temperature and displacement fields. This type of problems with non-linear viscosities can only be solved numerically [6].

2.1.5 Energy or temperature equation

The equation describing the energy conservation of a continuous medium is [1,8]:

$$\frac{de}{dt} = \boldsymbol{\sigma} : \dot{\boldsymbol{\varepsilon}} - \nabla \cdot \mathbf{q} + \rho r \text{ in } \Omega \times (0, t_f) \tag{21}$$

where Ω and $(0, t_f)$ are defined in section 2.1.1. For hot rolling problems, this can be rewritten in terms of the temperature T taking into account the material incompressibility, assuming the thermal expansion coefficient equal zero, and replacing Fourier laws ($\mathbf{q} = -k\nabla T$) and the constitutive equation (18), i.e.

$$\rho c_p \Big(\frac{\partial T}{\partial t} + (\mathbf{u} \cdot \nabla) T \Big) - \nabla \cdot (k \nabla T) = 2\mu \dot{\boldsymbol{\varepsilon}} : \dot{\boldsymbol{\varepsilon}} + \rho r = Q \text{ in } \Omega \times (0, t_f) \tag{22a}$$

with

$$\begin{aligned} T &= \overline{T} \text{ on } \Gamma_T \times (0, t_f) \\ \mathbf{n} \cdot \nabla T &= \overline{\mathbf{q}} \text{ on } \Gamma_q \times (0, t_f) \\ T(\mathbf{x}, 0) &= T_0(\mathbf{x}) \text{ in } \Omega \times \{0\} \end{aligned} \tag{22b}$$

where $\Gamma_T = \{\mathbf{x} \in \partial\Omega | T(\mathbf{x}, t) = \overline{T}(\mathbf{x}, t) \; \forall t \in (0, t_f)\}$ and $\overline{T}(\mathbf{x}, t)$ is a given function; $\Gamma_q = \{\mathbf{x} \in \partial\Omega | (\mathbf{n} \cdot \nabla T)(\mathbf{x}, t) = \overline{\mathbf{q}}(\mathbf{x}, t) \; \forall t \in (0, t_f)\}$, with $\overline{\mathbf{q}}(\mathbf{x}, t)$ being a given function; $\overline{\Gamma_T \bigcup \Gamma_q} = \partial\Omega$ and $\Gamma_T \bigcap \Gamma_q = \emptyset$; c_p is the specific heat at constant pressure and k the thermal diffusivity coefficient.

2.1.6 Treatment of the free surface. Computation of displacements and strains calculation

The displacement field must be solved to calculate the equivalent strain. Also, we need to compute the domain occupied by the material at each time step to

solve the equilibrium and temperature equations. In this section, two different approachs for these computations will be presented.

•*Eulerian approach*

This is the so called pseudo-concentration method. The basic idea is to define a scalar function $\psi(\boldsymbol{x})$ over the computational domain Ω ($\Omega = \Omega_m \bigcup \Omega_f$, $\Omega_m \bigcap \Omega_f = \emptyset$, Ω_m: part of the domain occupied by the material, Ω_f = part of the domain occupied by air or "fictitious material"), in such a manner that its value in certain point indicates the presence or absence of fluid (or viscoplastic material). The position of the fluid front is defined by the isovalue contour $\psi(\mathbf{x}) = \psi_c$. The conservation of the pseudo-concentration in any control volume $V_t \subset \Omega$ which is moving with the divergence free velocity field $\mathbf{u}$, can be written as:

$$\frac{\partial \psi}{\partial t} + \mathbf{u} \cdot \nabla \psi = 0 \text{ in } \Omega \times (0, t_f) \tag{23a}$$

with

$$\begin{aligned} \psi(\mathbf{x}, t) &= \overline{\psi}(\mathbf{x}, t) \; \mathbf{x} \in \Gamma_i \times (0, t_f) \\ \psi(\mathbf{x}, 0) &= \psi_0(\mathbf{x}) \; \mathbf{x} \in \Omega \\ \Gamma_i &= \{\mathbf{x} \in \partial\Omega |\; \mathbf{u}(\mathbf{x}, t) \cdot \mathbf{n} < 0\} \end{aligned} \tag{23b}$$

$\overline{\psi}$ is a given function; $\psi_0(\mathbf{x})$ should define the initial position of the fluid front and $\mathbf{n}$ is the external unit vector normal to Ω. More details about this method can be found in [6,9,10,11,12,13]. The equation below defines the material front, but does not provide information about the displacement and strain fields. To obtain the equivalent strain field (this is necessary for the constitutive law), some authors propose to solve the following equation [9,10]:

$$\frac{\partial \overline{\varepsilon}}{\partial t} + \mathbf{u} \cdot \nabla \overline{\varepsilon} = \dot{\overline{\varepsilon}} \text{ in } \Omega \times (0, t_f) \tag{24a}$$

with

$$\begin{aligned} \overline{\varepsilon}(\mathbf{x}, t) &= \overline{\overline{\varepsilon}}(\mathbf{x}, t) \; \mathbf{x} \in \Gamma_i \times (0, t_f) \\ \overline{\varepsilon}(\mathbf{x}, 0) &= \overline{\varepsilon}_0(\mathbf{x}) \; \mathbf{x} \in \Omega \\ \Gamma_i &:= \{\mathbf{x} \in \partial\Omega | \mathbf{u} \cdot \mathbf{n} < 0\} \end{aligned} \tag{24b}$$

where $\overline{\overline{\varepsilon}}$ is a known function and $\overline{\varepsilon}_0$ defines an initial equivalent strain field.

•*Lagrangian approach*

The displacement s of a material particle m is given by:

$$\mathbf{s}^m(t) = \mathbf{x}^m(t) - \mathbf{X}^m \; t \in [0, t_f] \tag{25}$$

where $\mathbf{x}^m(t)$ are the spatial coordinates of the particle m at time t, and $\mathbf{X}^m$ the material coordinates ($\mathbf{X}^m = \mathbf{x}^m(0)$). The particle velocity can be computed as:

$$\frac{d\mathbf{x}^m}{dt} = \mathbf{u}^m \text{ for } t \in (0, t_f) \tag{26}$$

then,

$$\mathbf{x}^m(t) = \int_0^t \mathbf{u}^m(t')\, dt' + \mathbf{X}^m \text{ for } t \in [0, t_f] \tag{27}$$

Then, the material strain tensor for each particle can be computed using the following expression [1] (Supresing the super-index m):

$$\boldsymbol{\varepsilon} = \frac{1}{2}(\nabla \mathbf{s} + \mathbf{s}\nabla + \nabla \mathbf{s} : \mathbf{s}\nabla) \tag{28}$$

or in indicial notation:

$$\varepsilon_{ij} = \frac{1}{2}\left(\frac{\partial s_i}{\partial X_j} + \frac{\partial s_j}{\partial X_i} + \frac{\partial s_k}{\partial X_i}\frac{\partial s_k}{\partial X_j}\right) \tag{29}$$

Then, basically the velocity field is integrated along the particle trajectories to obtain the displacement and strain field. Finally, if spatial coordinates of each material particle for each time $t \in [0, t_f]$ are known, then we obviously also know the domain accupied by the fluid at that time.

2.2 Physical aspects of friction

In this section we shall present two models. The first is based the Coulombs law and Avitzur micromechanical model [2]. The second, simulates the presence of a lubricant between the contact surfaces.

2.2.1 Friction model based on Avitzur's micromechanical model and Coulomb's law

The Avitzur's micromechanical model basically states that the friction force F between the contact surfaces raises directly proportional to the vertical force P until a constant force F is reached [2,4,5] (See Figure 2a). Analogous to plasticity

theory, the Coulomb's law states an slip criterion that can be represented in the space of normal and tangencial stresses as shown in Figure 2b. The stress states which lie within the slip surface produce only reversible motion, while the stress states on the slip surface produce irreversible relative motion [2,4,5]. In our problem we assume that the stresses are always on the slip surface, and a friction rule that combines Avitzur's model and Coulomb law is adopted. This is presented graphically in Figure 2c.

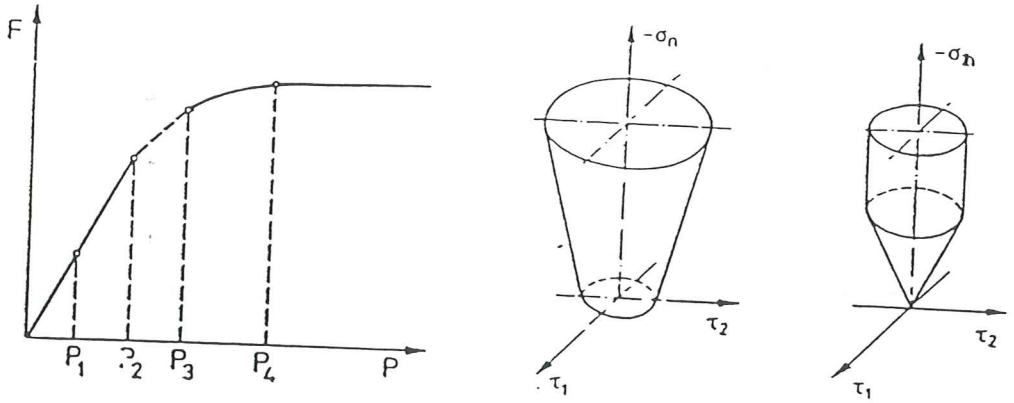

Figure 2 a)P normal vs F friction. b)Coulomb's law. c)Slipping criterium

Mathematically, the friction law can be written as:

$$\tau_n = \begin{cases} \xi\sigma_n, & \text{if } \sigma_n \leq \sigma_y \\ m\sigma_y/\sqrt{3}, & \text{if } \sigma_n > \sigma_y \end{cases} \tag{30}$$

where τ_n is the shear stress between the contact surfaces, σ_n the normal stress, ξ the Coulomb coefficient, $m < 1.0$ the friction factor to take in account the surface slip, and $\sigma_y/\sqrt{3}$ denotes the maximum shear stress that the material can withstand according to the Von Mises yield criterion.

2.2.2 Flow friction - Lubricant approach

This approach assumes the presence of a lubricant between the contact surfaces. The lubricant viscosity is smaller than the viscosity of the hot rolling material, and this generates flow velocity profiles similar to those produced by the friction between a fluid an a solid surface. The velocity gradient is very high in the lubricant region, thus simulating a jump between the velocity at the roll and material surfaces (one surface slips over the other). The shear stress between the two surfaces is obtained from the constitutive law for an incompressible fluid (equation (18)) using the lubricant viscosity.

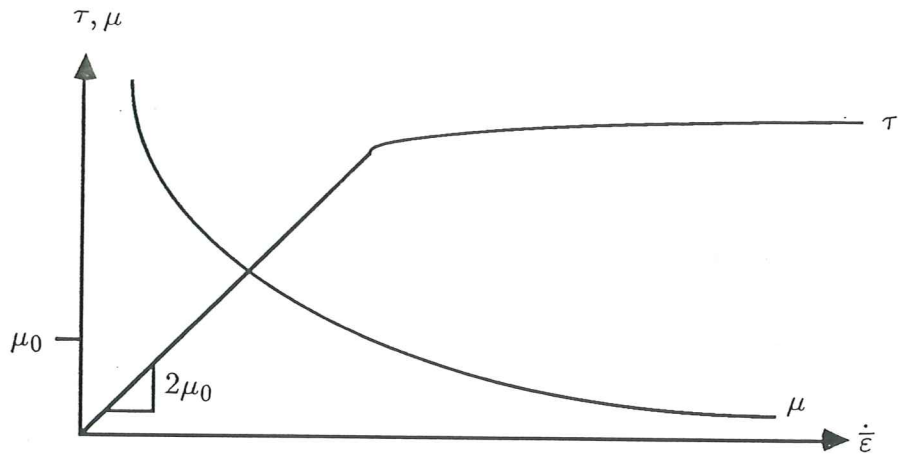

Figure 3 Flow friction - Lubricant approach

In this model, the shear stress is directly proportional to the strain rate and a cut-off value for high strain rate values must be defined. This is given automatically if we impose that the lubricant viscosity be always small than the viscosity computed using (19). This friction law is graphically represented in Figure 3.

3. NUMERICAL SOLUTION USING THE FLOW APPROACH

In this section the numerical solution of the non-linear thermomechanical problem sketched above will be presented.

3.1 Stokes and continuity equations

Let Ω_m be the domain occupied by the hot material (metal). Let Ω_f be the domain occupied by a circundant fictitious fluid. The flow domain Ω where the equilibrium and energy equations will be solved is defined as: $\Omega = \Omega_m \bigcup \Omega_f$ and $\Omega_m \bigcap \Omega_f = \emptyset$. The variational form, "weak" form, of the stationary Stokes problem (equations (17) and (20)) consist in finding $\mathbf{u} \in U$ and $p \in Q/Z$ such that

$$\begin{aligned} a(\mathbf{u},\mathbf{v}) - b(p,\mathbf{v}) &= l(\mathbf{v}) \quad \forall \mathbf{v} \in V \\ b(q,\mathbf{u}) &= 0 \quad \forall q \in Q \end{aligned} \tag{31a}$$

with

$$\begin{aligned} U &= \{\mathbf{u} \in H^1(\Omega) | \mathbf{u} = \overline{\mathbf{u}} \text{ on } \Gamma_u\} \\ V &= \{\mathbf{v} \in H^1(\Omega) | \mathbf{v} = 0 \text{ on } \Gamma_u\} \\ Q &= \{q \in L^2(\Omega)\} \\ Z &= \{q \in Q | b(q,\mathbf{v}) = 0 \ \forall \mathbf{v} \in V\} \end{aligned} \tag{31b}$$

The multilinear forms are:

$$\begin{aligned} a(\mathbf{u},\mathbf{v}) &= \int_\Omega 2\mu\ \varepsilon(\mathbf{u}) :\ \varepsilon(\mathbf{v})\ d\Omega \\ b(q,\mathbf{v}) &= \int_\Omega \nabla\cdot\mathbf{v}\ d\Omega \\ l(\mathbf{v}) &= \int_\Omega \rho\mathbf{b}\cdot\mathbf{v}\ d\Omega \end{aligned} \tag{32}$$

3.1.1 Incompresibility treatment - Iterative penalty method

This method is used to eliminate the pressure in the problem, thus obtaining a considerable reduction in computing time and memory (See [14]). Penalization methods also avoid the use of partial pivoting to solve the system of equations resulting from (31) and reduce the number of equation.

The classical penalty method consist in perturbing the continuity equation with a small term containing the pressure:

$$\epsilon p + \nabla\cdot\mathbf{u} = 0 \text{ in } \Omega \tag{33}$$

with $\epsilon > 0$ being a small number. The classical penalization presents some problems for non-Newtonian fluids [6,15]. If the penalization parameter ϵ is too large the incompressibility condition is not satisfied, while for too small values the resulting system is ill-conditioned [6,7,15]. To avoid this problem, we will use an iterative penalty method proposed in [6,15], which can be written as:

$$\epsilon(p^i - p^{i-1}) + \nabla\cdot\mathbf{u} = 0 \text{ in } \Omega \tag{34}$$

where index i indicates the iteration number. In this manner, the incompressibility constraint is satisfied iteratively, and the penalty parameter can be larger than in the classical approach. In addition, since the solution of the coupled non-Newtonian flow problem requires an iterative algorithm, then the iterative penalization only introduces a small additional effort and it does not involve additional iterations to satisfy the incompresibility constraint.

The weak form of Stokes problem with iterative penalization is written as: Given $p^0 \in Q_0$, for $i = 1, 2, \ldots$ find $(\mathbf{u}^i, p^i) \in V \times Q_0$ such that

$$\begin{aligned} a(\mathbf{u},\mathbf{v}) - b(p,\mathbf{v}) &= l(\mathbf{v}) && \forall \mathbf{v} \in V \\ \epsilon(p^i, q) + b(q,\mathbf{u}) &= \epsilon(p^{i-1}, q) && \forall q \in Q \end{aligned} \tag{35a}$$

with

$$Q_0 = \{q \in Q | \int_\Omega q \, d\Omega = 0\} \tag{35b}$$

where $(\cdot,\cdot)$ is the inner product in L^2. The system of equations (35) was obtained by penalizing in the weak form ("weak penalization"). If the penalization is introduced first in the continuous problem and then the weak form is obtained ("strong penalization") the method would present serious problems (see [14,15] for details). Other penalization procedure is the so called "artificial compressibility" method, which is phisically grounded. This assumes a small compressibility in the fluid, then the continuity equation can be written as:

$$\frac{1}{c^2}\frac{\partial p}{\partial t} + \nabla \cdot \mathbf{u} = 0 \tag{36}$$

where c is the sound velocity. If $c \to \infty$ the incompressibility is reached. From (36), the incompressibility constraint is satisfied if $\nabla \cdot \mathbf{u} \approx \frac{1}{c^2}$.

In this work the iterative penalization approach has been adopted. The magnitude order for the penalization parameter was found heuristically as $10^{-9}\mu - 10^{-6}\mu$.

Now, let Ω^e be a regular finite element partition of the domain Ω, with index e ranging from 1 to the number of elements N_{el}. If the test functions are chosen in the conforming finite element spaces associated to the partition Ω^e, $V_h \subset V$ and $Q_h \subset Q$, and the space of trial solutions in the conforming finite element spaces associated to the partition Ω^e, $U_h \subset U$ and $Q_{0,h} \subset Q_0$, the following system of equations (including the temporal term in the weak formulation) is obtained:

$$\begin{aligned} \mathbf{M_v}\frac{\partial \mathbf{u_n}}{\partial t} + (\tau \mathbf{H^t M_p^{-1} H} + \mathbf{K})\mathbf{u_n} &= \mathbf{F} \\ \mathbf{M_p} p_m^i + \tau \mathbf{H u_n} &= \mathbf{M_p} p_m^{i-1} \end{aligned} \tag{37}$$

where $\tau = 1/\epsilon$, $\mathbf{u_n} = (\mathbf{u}_1, \mathbf{u}_2, ..., \mathbf{u}_n)^t$ and $p_m = (p_1, p_2, ..., p_m)^t$ (n = number of mesh velocity nodes and m = number of mesh pressure nodes).

The different elemental matrices for the two dimensional case can be seen in Box I, where N_i and $\overline{N}_i$ are the basis interpolation functions for the velocity and pressure spaces respectively. To solve the temporal derivate in (37), the trapezoidal rule is used (see section 3.4)

As defined in 3.1, the domain of solution includes a fictitious material. Values for fictitious material properties should to be chosen so that they do not produce

BOX I: Elemental matrices for equation (37)

$$M^e_{v_{ij}} = \int_{\Omega^e} \rho \begin{bmatrix} N_i N_j & 0 \\ 0 & N_i N_j \end{bmatrix} \quad ; M^e_{p_{ij}} = \int_{\Omega^e} [\overline{N}_i \overline{N}_j \quad]$$

$$H^e_{ij} = \int_{\Omega^e} [\overline{N}_i \partial_1 N_j \quad \overline{N}_i \, \partial_2 N_j \,] \quad ; F^e_i = \int_{\Omega^e} \rho \, [\, N_i b_1 \quad N_i b_2 \,]^t$$

$$K^e_{ij} = \int_{\Omega^e} \mu \begin{bmatrix} 2\partial_1 N_i \, \partial_1 N_j + \partial_2 N_i \, \partial_2 N_j & \partial_2 N_i \, \partial_1 N_j \\ \partial_1 N_i \, \partial_2 N_j & 2\partial_2 N_i \, \partial_2 N_j + \partial_1 N_i \, \partial_1 N_j \end{bmatrix}$$

ill-conditioning and do not influence the metal flow. Recommended values are [6,11,12,13]:

$$\begin{aligned} \mu_{fic} &= 10^{-6} \mu_{real} \\ (\rho c_p)_{fic} &= 10^{-3} (\rho c_p)_{real} \\ k_{fic} &= 10^{-3} k_{real} \end{aligned} \tag{38}$$

Finally, the finite element used to interpolate the velocity and pressure fields must satisfy the LBB condition (div-stable elements). In this work the Q_2/P_1 element has been used [6,14,18].

3.2 Temperature equation

The weak formulation of the temperature equation (22) can be written as: Given $T(\mathbf{x}, 0) = T_0$ for $\mathbf{x} \in \Omega$, find $T \in \Upsilon$ such that

$$\rho c_p (v, \frac{\partial T}{\partial t}) + \rho c_p (v, (\mathbf{u} \cdot \nabla) T) + (\nabla v, k \nabla T) = (v, Q) \; \forall v \in V \tag{39a}$$

with

$$\begin{aligned} V &= \{ v \in H^1(\Omega) | \;\; v|_{\Gamma_T} = 0 \} \\ \Upsilon &= \{ T \in L^2(0, t_f; H^1(\Omega)) | \;\; T|_{\Gamma_T} = \overline{T}, \; t \in (0, t_f) \} \end{aligned} \tag{39b}$$

BOX II: Elemental matrix terms for equation (42)

$$M^e_{ij} = \int_{\Omega^e} \rho c_p [\hat{N}_i N_j] \qquad ; L^e_{ij} = \int_{\Omega^e} \rho c_p [\hat{N}_i \, u_k \, \partial_k N_j]$$

$$K^e_{ij} = \int_{\Omega^e} k [\partial_k N_i \, \partial_k N_j] \qquad ; \tilde{K}^e_i = \int_{\Omega^e} -k [\tilde{N}_i \, \partial^2_{kk} N_j]$$

$$Q^e_i = \int_{\Omega^e} [\hat{N}_i (\sigma_{kl} \dot{\epsilon}_{kl} + \rho r)]$$

3.2.1 Convection difusion treatment - SUPG method

To avoid oscillations in case of convection dominated flow (Peclet number greater than 1 $Pe = \rho c_p U/k > 1.0$), the SUPG method (Streamline Upwinding Petrov-Galerkin) is used, here the traditional Galerkin test functions N_i are modified in the flow direction as:

$$\hat{N}_i = N_i + \tilde{N}_i = N_i + \frac{\alpha^e h^e}{2\|\mathbf{u}\|} \mathbf{u} \cdot \nabla N_i \tag{40}$$

where α_e is a function of the elemental Peclet number and h^e is a typical element dimension. More details about this method can be found in references [6,15,16,17,18,19,20]. The weak formulation using SUPG is rewritten as:

$$\rho c_p (\hat{v}, \frac{\partial T}{\partial t}) + \rho c_p (\hat{v}, (\mathbf{u} \cdot \nabla) T) + (\nabla v, k \nabla T) - \sum_{e=1}^{N_{el}} (\tilde{v}^e, \nabla \cdot (k \nabla T)) = (\hat{v}, Q) \; \forall v \in V$$

$$\hat{v} = v + \tilde{v} = v + \frac{\alpha^e h^e}{2\|\mathbf{u}\|} \mathbf{u} \cdot \nabla v \tag{41}$$

Now, let Ω^e be a regular finite element partition of the domain Ω, with index e ranging from 1 to the number of elements N_{el}. If test and trial functions are chosen in the conforming finite element space associated to the partition Ω^e $V_h \subset V$ and $\Upsilon_h \subset \Upsilon$, the following system of equations is obtained:

$$\mathbf{M} \frac{\partial T_n}{\partial t} + (\mathbf{L} + \mathbf{K} + \tilde{\mathbf{K}}) T_n = \mathbf{Q} \tag{42}$$

where $T_n = (T_1, T_2, ..., T_n)^t$, n = number of mesh nodes. In Box II the element matrix terms are shown.

In above formulation, the radiation boundary condition:

$$\nabla T \cdot \mathbf{n} = q = \beta(T - T_e) \text{ in } \Gamma_{q_e} \tag{43}$$

has not been considered. The heat conduction to air is simulated automatically by chosing the flow and air domains. On the other hand, the conduction to the roll is neglected. This is a good approximation for normal rolling speeds, where the contact time is ≤ 1 s [21]. The temporal derivates in (42) are solved using the trapezoidal rule explained below.

3.3 Free surface and strain field computation

As we see in 2.1.6, two different approaches for this computation are proposed. In this section we shall show their numerical solutions.

3.3.1 Eulerian computation - Pseudo-concentration method

The equation (23) is purely convective. Then the use of a method to avoid convection dominated oscillations is mandatory. In this work the SUPG method, described in 3.2.1, is used. Defining the test function $\hat{v} = v + \eta v$ with ηv being a specific function of the element length, type and velocity (see [6,15,16,17,18,19,20]), the weak form of (23) can be written as: Given $\psi(\mathbf{x}, 0) = \psi_0$ $\mathbf{x} \in \Omega$, find $\psi \in \Psi$ such that

$$(\hat{v}, \frac{\partial \psi}{\partial t}) + (\hat{v}, (\mathbf{u} \cdot \nabla)\psi) = 0 \ \forall v \in V \tag{44a}$$

$$\begin{aligned} V &= \{v \in H^1(\Omega) |\ \ v|_{\Gamma_i} = 0\} \\ \Psi &= \{\psi \in L^2(0, t_f; H^1(\Omega)) |\ \ \psi|_{\Gamma_i} = \overline{\psi}\ \forall t \in (0, t_f)\} \end{aligned} \tag{44b}$$

Now, let Ω^e be a regular finite element partition of domain Ω, with index e ranging from 1 to the number of elements N_{el}. If test and trial functions are chosen in the conforming finite element space associated to the partition Ω^e, $V_h \subset V$ and $\Psi_h \subset \Psi$, the following system of equations is obtained:

$$\mathbf{M}\frac{\partial \psi_n}{\partial t} + \mathbf{L}\psi_n = \mathbf{0} \tag{45}$$

where $\psi_n = (\psi_1, \psi_2, ..., \psi_n)^t$, n = number of mesh nodes. The element matrix terms are equal to the temperature matrix terms in equation (42), taking $\rho = c_p = 1.0$ (see Box II). The temporal derivates are solved using the trapezoidal rule as it will show in Section 3.4.

3.3.2 Lagrangian computation

The idea is to work with two finite element meshes. The first is the spatial mesh where the equilibrium and energy equation are solved (Finite element discretization of flow domain Ω). The second is the lagrangian or material mesh. This mesh discretizes the hot metal (domain Ω_m) and moves with it. Then, the material particle trajectories coinciding with the nodal points of the material mesh are computed and, therefore, the displacement field of the metal is obtained. The procedure is as follow: Given a $\mathbf{u}_n$ (velocities on the spatial mesh, (see equation (37)) do the following steps:

i)Obtain velocities of material mesh

The material mesh velocity vectors $\mathbf{u}_n^m$ (nodal point velocities) are computed using the spatial interpolation functions (trial functions of the spatial finite element discretization) as follows:

$$u_k^m = (N_j(\xi^m)^e \; u_{kj}), \quad k = 1, nd \; , \; j = 1, nn \tag{46}$$

where u_k^m is the k velocity component of the material nodal point m; e is the spatial mesh element such that $\mathbf{x}^m \in \overline{\Omega}^e$ ($\Omega^e \subset \Omega$ is the spatial domain of element e); N_j is the spatial interpolation function of nodal point j; $(\xi^m)^e$ is the natural coordinate vector of $\mathbf{x}^m$ in e; u_{kj} is the k velocity component of spatial mesh nodal point j; nd is the problem dimension (2 or 3) and nn the number of spatial mesh nodes. To calculate $(\xi^m)^e$ the non-linear system resulting from spatial coordinate interpolation is solved, i.e.

$$x_k^m(t^{n-1}) = (N_j(\xi^m)^e \; x_{kj}), \; k = 1, nd \; , \; j = 1, nn \tag{47}$$

where x_k^m is the k component of the spatial position vector for particle m; t^{n-1} is the $n-1$ time step (t^n is the actual time step $0 \leq t^{n-1} < t_f$); and x_{kj} is the kth component of position vector of the jth spatial node. Then, for each material node, we have to solve (47) for each spatial mesh element until $(\mathbf{s}^m)^e$ ranges into the isoparametical space chosen for the spatial elements. To solve (47) we use the Newton-Raphson method [20]. To save computer time, the spatial nodal position $\mathbf{x}_i$ closer to $\mathbf{x}^m(t^{n-1})$ is obtained and (47) is solved only for the set of elements e such that $\mathbf{x}_i \in \Omega^e$.

ii)Obtain the displacement field

The new spatial position for each material node is obtained by solving

numerically (27) with a Runge-Kutta method. Then

$$\mathbf{x}^m(t^n) = \mathbf{x}^m(t^{n-1}) + \int_{t^{n-1}}^{t^n} \mathbf{u}^m(t)dt \tag{48}$$

The displacement of each material node (nodal points of the material mesh) is calculated as:

$$\mathbf{s}^m(t^n) = \mathbf{x}^m(t^n) - \mathbf{X}^m \tag{49}$$

iii)Obtain the equivalent strain at spatial nodes

The spatial nodal point displacements can be interpolated from the material nodal point displacements by using the trial functions of the lagrangian mesh:

$$\mathbf{s} = M_j \mathbf{s}_\mathbf{j}^\mathbf{m} \quad , \quad j = 1, nm \tag{50}$$

Then, the Green-Lagrange strain tensor on the spatial nodal points can be calculated using (29) as:

$$\varepsilon_{kl}^f = \frac{\partial M_j(\xi^f)}{\partial X_k} u_{lj}^m + \frac{\partial M_j(\xi^f)^M}{\partial X_l} u_{kj}^m + (\frac{\partial M_j(\xi^f)^M}{\partial X_k} u_{ij}^m)(\frac{\partial M_j(\xi^f)^M}{\partial X_l} u_{ij}^m) \tag{51}$$

where ε_{kl}^f is the kl component of the strain tensor evaluated at spatial node f; M is the material mesh element such that $\mathbf{x}^f \in \Omega^M(t^n)$ ($\Omega^M(t^n)$ is the spatial domain occupied by M at actual time step); M_j is the material mesh interpolation function associated to the material node j; $(\xi^f)^M$ is the natural coordinate vector of the spatial node f in M; and nm the number of material mesh nodes. To calculate $(\xi^f)^M$, the non-linear system resulting from the material coordinate interpolation is solved as:

$$x_k^f = M_j(\xi^f)^M \; x_{kj}(t^n), \; k = 1, nd \; , \; j = 1, nm \tag{52}$$

where x_k^f is the kth component of the position vector for the spatial node f; and $x_{kj}(t^n)$ is the spatial position vector of material node j at the actual time step. Then, as (47), equation (52) has to be solved for each spatial node, and for each material mesh element until $(\xi^f)^M$ ranges into the isoparametical space chosen for the material elements. To solve (52) the Newton-Raphson method [20] is used. To save computer time, the material nodal position $\mathbf{x}_i$ closer to $\mathbf{x}^f(t^{n-1})$ is obtained and (52) is solved only for the set of elements M such that $\mathbf{x}_i \in \Omega^M$. With above procedure, not only the strain and displacement fields are obtained, but also the set of spatial nodes i such that $\mathbf{x}_i \in \Omega_m$, and, therefore, the free surface of the material (hot metal). Finally, for continuous rolling processes, the material position at $0 \leq t^n \leq t_f$ is obtained by superposing the position of the different Lagrangian mesh positions from 0 to t^{n-1}; this is $\Omega_m(t^n) = \Omega_m(0) \bigcup \Omega_m(t_1) \bigcup ... \Omega_m(t^{n-1})$.

3.4 Temporal discretization

To solve the temporal derivate of equations (37), (42) and (45), the trapezoidal rule is used (θ method). Then, the temporal derivate is replaced by a finite difference, and the matrices have to be evaluated at time steps n and $n+1$ (i.e. solution at time n is known and we look for solution at $n+1$), as follow:

$$\frac{x^{n+1}-x^n}{\Delta t} \approx \theta F^{n+1} + (1-\theta)F^n \quad \text{for} \quad 0.0 \leq \theta \leq 1.0 \tag{53}$$

For $\theta \geq 0.5$ the method is inconditionally stable. for $\theta < 0.5$ the method is conditionally stable, and it can be proved that for $\theta = 0.0$ the critical time step is of the penalty parameter order [6,7,14,15,20,24]. Furthermore, the approximation order of the method is second for Crank-Nicolson $\theta = 0.5$, and linear for $\theta = 0.0$ (forward Euler) and $\theta = 1.0$ (backward Euler). Furthermore, the backward Euler scheme is more dissipative, which is good to supress the oscillating harmonics associated to the series expansion of the parabolic equation solutions [15]. In most of the examples presented in Section 4., the backward Euler scheme was used. More details about the trapezoidal rule can be found in references [14,15,20,24].

3.5 Friction computations

The frictional stress is simulated by inserting a narrow layer of elements between the roll and metal contact surfaces (friction elements). The viscosity in these elements is calculated in such a way that the shear stress that is given by the constitutive law ($\tau_{ij} = 2\mu\dot{\varepsilon}_{ij}$) be equal to that given by the chosen friction model.

3.5.1 Avitzur - Coulomb model

This model is obtained computing the viscosity and the yield stress at the friction elements as:

$$\sigma_y = 1.5 \frac{\dot{\bar{\varepsilon}}}{\dot{\varepsilon_\tau}} \xi p \tag{54}$$

$$\mu_f = \frac{\sigma_y}{3\,\dot{\bar{\varepsilon}}} < \frac{m\sigma_y}{2\sqrt{3}\dot{\varepsilon_\tau}} \tag{55}$$

where $\dot{\varepsilon_\tau} = \sqrt{\dot{\varepsilon_{ij}}\dot{\varepsilon_{ij}}}$ for $i \neq j$, and μ_f is the viscosity at each friction element.

3.5.2 Lubricant approach

This model is obtained calculating the viscosity at friction elements as:

$$\mu_f = \min(\mu, \mu_0) \tag{56}$$

where μ_0 is a given "lubricant" viscosity, and μ the metal viscosity calculated with the constitutive law.

3.6 Stress field computation

The material stress field is calculated from the velocity and pressure fields using the constitutive equation for incompressible fluids (18). The deviatoric stress tensor at each elemental gauss points τ^g_{kl} is calculated from the velocity field, by using the spatial interpolation functions as:

$$\tau^g_{kl} = \mu(\partial_k N_i \; u^i_l + \partial_l N_i \; u^i_k) \text{ for } i = 1...n_u \; k, l = 1, ...n_d \tag{57}$$

where n_u is the number of velocity nodes and n_d the problem dimension (2 or 3). Finally, the stress field is obtained at mesh nodal points by smoothing the stress field at the gauss points. This is by solving the following equation system:

$$(N_i, \tau^n_{kl}) = (N_i, \tau^g_{kl}) \; \forall i \tag{58}$$

where N_i are the spatial interpolation functions and τ^n_{kl} is the stress field at the nodal points. Because of the type of elements used in this formulation, pressure nodal points do not coincide with spatial mesh nodal points. Then, the pressure field has to be smoothed too.

As a final remark, the smoothing can be performed by three different methods: Diagonal matrix (Lumped), consistent matrix (Consistent) or using a closed integration rule to solve (58) (Quadrature). In the numerical examples presented in Section 4, diagonal matrix smoothing (Lumped) is used.

3.7 Roll force and torque computation

The normal τ_{nn} and tangencial τ_{nt} deviatoric stress components at the roll nodes are computed from the deviatoric stress field by:

$$\tau^i_{nn} = (\boldsymbol{\tau}^i \cdot \mathbf{n}^i_r) \cdot \mathbf{n}^i_r \text{ and } \tau^i_{nt} = (\boldsymbol{\tau}^i \cdot \mathbf{n}^i_r) \cdot \mathbf{t}^i_r \tag{59}$$

where index i indicates the number of the roll node, $\mathbf{n}_r^i$ is the normal unitary vector at roll node i and $\mathbf{t}_r^i$ the tangencial unit vector. Each roll node has an adjacent surface area a^i, and the roll's normal force F_n^i, roll's tangencial force F_t^i and roll's torque M^i at each contact node are calculated by:

$$F_n^i = (-p^i + \tau_{nn}^i)a^i; \quad F_t^i = \tau_{nt}^i a^i; \quad M^i = F_t^i \, r \tag{60}$$

where p^i is the pressure at node i and r the roll radius. Above computation is performed only at roll nodes in contact with the hot metal.

Finally the roll force and torque are computed by adding the roll forces and torques at each contact node and performing a rotation to the spatial reference axis.

3.8 Microstructural changes

The microstructural changes that occur during rolling process influence the product's mechanical properties. The grain size of the ferrite phase, produced by transformation during cooling, determines the material's mechanical properties. This ferritic grain size is determined by the residual strain and grain size of austenite phase prior to transformation. Therefore, it is important to model the structural changes occuring during austenitic phase [26]. In this section we present a numerical strategy to compute the changes taking place within the austenitic phase by using the finite element model described before.

Plastic deformation of metal results in dislocations within the metal's crystal structure which increase the internal energy within the structure. If the dislocation density reaches a critical level, and enough thermal energy is given, the deformed metal grains nucleate and recristallize forming new dislocation-free (and generally smaller) grains with lower energy states [26]. The critical dislocation density level is reached if a critical plastic strain ε_c, given by [2,26]:

$$\varepsilon_c = a \, \varepsilon_p \tag{61}$$

is exceded. In (61) a is a material dependent constant between 0.67 and 0.86, and ε_p is the strain for which the peak yield stress is reached (see Figure 4), given by:

$$\varepsilon_p = A \, d_0^{1/2} \, Z^n \tag{62}$$

where A and n are material constants, d_0 is the initial grain size, and Z the Zener-Hollomon parameter given by (9). With further deformation, the new

crystal structure becomes distorted, accumulating dislocations, and recrystallizes again [26]. This recrystallization occuring during deformation is termed dynamic recrystallization. These microstructural changes leave the metal in a unstable state and provide the driving force for static recrystallization and recovery to take place after deformation pass. If the temperature is sufficiently high, grain growth occurs after static recrystallization [26]. The whole recrystallization process can be described by Sellers experimental model, as follows:

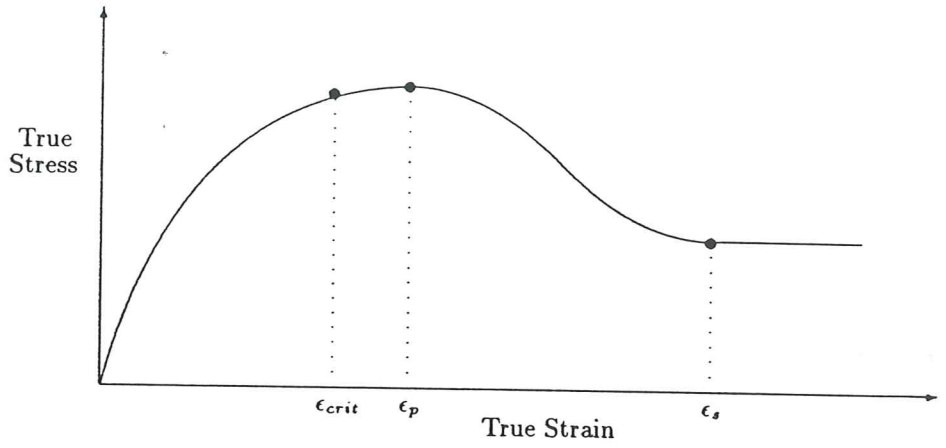

Figure 4 Stress/strain behaviour during steady state deformation at elevated temperatures [26]

Dynamic recrystallization

It occurs during the deformation process. Dynamic recrystallization starts when the strain ε reaches the ε_c value of (61) (see Figure 4). If the strain increases, the yield stress increases as the material work-hardens. The flow stress reaches a maximum at $\varepsilon = \varepsilon_p$, and a steady state flow stress is reached, at $\varepsilon = \varepsilon_s$, when softening due to recrystalization balances work-hardening.

Then the dynamic recrystallization occurs during deformation and $\varepsilon_c \leq \varepsilon \leq \varepsilon_s$ where ε_s is given by:

$$\varepsilon_s \approx 2\ \varepsilon_p \tag{63}$$

The volume fraction recrystallized X_V follows Avrami's equation:

$$X_V = 1 - \exp(-2.996(\frac{\varepsilon - \varepsilon_c}{\varepsilon_s - \varepsilon_c})) \tag{64}$$

The dynamic recrystallized grain size is given by:

$$\begin{aligned} d_{rex} &= D\ d_0^{0.67}\ \varepsilon^{-1} \quad \text{for} \quad \varepsilon < \varepsilon^* \\ d_{rex} &= D^*\ Z^{-u} \quad \text{for} \quad \varepsilon \geq \varepsilon^* \end{aligned} \tag{65}$$

where D and u are constants, $D^* = 3.6 \cdot 10^{-3} D$ and ε^* is given by:

$$\varepsilon^* = 0.57\ d_0^{0.17}\ \varepsilon_p \tag{66}$$

the value for ε^* is greater than ε_c ($d_0 \approx 300\ \mu m$). The average grain size, is then given by:

$$d_{ave} = X_V\ d_{rex} + (1 - X_V)\ d_0 \tag{67}$$

Static recrystallization

This occurs after deformation. The volume fraction staticaly recrystallized X_V is given by Avrami's equation:

$$X_V = 1 - \exp(\log(1 - F)(t/t_f)^k) \tag{68}$$

where t_f is the time for some specific fraction F of recrystallization and k is a constant given by:

$$k = \begin{cases} 2 & , \text{if } \varepsilon < \varepsilon_c \\ 1 & , \text{if } \varepsilon \geq \varepsilon_c \end{cases} \tag{69}$$

The time for fifty percent of recrystallization, $t_{0.5}$, for C-Mn steels is given by:

$$\begin{aligned} t_{0.5} &= B\varepsilon^{-m} d_0^p Z^q \exp(\frac{Q_{rex}}{RT}) \quad \text{for} \quad \varepsilon < \varepsilon_c \\ t_{0.5} &= B' Z^r \exp(\frac{Q_{rex}}{RT}) \quad \text{for} \quad \varepsilon \geq \varepsilon_c \end{aligned} \tag{70}$$

where B, B', p, q and r are constants, and Q_{rex} is the reactivation energy for recrystallization.

The recrystallization grain size d_{rex} and average grain size d_{ave} are also given by (65) and (67) respectively. The static recrystallization is assumed to be complete for $X_V \geq 0.95$, followed by grain growth.

Grain Growth

When static recrystallization is complete ($X_V \geq 0.95$), the grain size raises as a function of time t and temperature, as follow [2,26]:

$$d = (d_{rex}^{10} + A' t \exp(\frac{-Q_{gg}}{RT}))^{\frac{1}{10}} \tag{71}$$

where A' and Q_{gg} are constants.

3.8.1 Implementation of microstructural changes

For hot rolling problems, there is not need to compute the dynamic recrystallization parameters (grain size, recrystallization fraction, etc.) [2,26,27]. This is due to the independece of the final grain size after the rolling pass (grain size for static recrystallization and grain growth) with the dynamic recrystallization parameters. The only important thing is to determinate the temperature and residual strain after the deformation state to start the static recrystallization computation [26].

BOX III. Microstructural Changes Algorithm

- Obtain T, $\bar{\varepsilon}$ and $\dot{\bar{\varepsilon}}$ from the finite element model (see BOX IV)
- Compute Z with (9)
- Compute ε_c and ε_p with (61) and (62)
- Compute k and $t_{0.5}$ with (69) and (70)
- Compute X_V with (68)
- Compute ε^* with (66)
- Compute d_{rex} with (65)
- IF $X_V < 0.95$ THEN
  - Compute grain size with (67)
- ELSE (Recrystalization has finished)
  - Compute grain size with (71)
- END IF

In Box III the general algorithm to calculate the recrystalization and grain growth is presented.

3.9 Coupled solution - Block iterative strategy

Box IV shows the iterative algorithm used for the solution of hot rolling process including the computation of static recrystallization changes.

BOX IV. General Algorithm

- Set the initial condition $\mathbf{u_n}^0$, T_n^0 and initial metal spatial position ($x^0 \in \Omega_m$ or ψ_n^0)
- $t := 0$
- WHILE $t < t_f$ DO:
  - $t \leftarrow t + \triangle t$
  - $i := 0$
  - WHILE (not converged) DO:
    - $i \leftarrow i + 1$
    - Obtain $\mathbf{u_n^i}$ and p_n^i by solving the time discretized form of (37)
    - Actualize properties (μ, c_p, k) whith the new velocity field $\mathbf{u_n^i}$
    - Obtain the displacement field $\mathbf{s}^i$ with Lagrangian method (Section 3.3.2), and the equivalent strain field $\overline{\varepsilon}^i$
    - Actualize properties (μ, c_p, k) whith the new equivalent strain and strain rate fields $\overline{\varepsilon}^i$
    - Obtain T_n^i by solving the time discretized form of (42)
    - Actualize properties (μ, c_p, k) whith the new temperature field T_n^i
    - IF $\|\mathbf{u_n^i} - \mathbf{u_n^{i-1}}\|_{L^2} \leq TOL\|\mathbf{u_n^i}\|_{L^2}$ and $\|T_n^i - T_n^{i-1}\|_{L^2} \leq TOL\|T_n^i\|_{L^2}$ THEN (converged)
  - END WHILE (not converged)
  - $\mathbf{u_n^t} \leftarrow \mathbf{u_n^i}$
  - $T_n^t \leftarrow T_n^i$
  - Obtain ψ_n^t, if necessary, by solving the time discretized form of (45)
  - Compute microstructural changes (grain size, BOX III)
  - Compute roll force and torque
- END WHILE $t < t_f$
- END

4. TEST VALIDATION AND NUMERICAL EXAMPLES

In this section we present a test validation and two numerical examples. The experimental data to compare with numerical results was provided by the Institut Fur Werkstoffumformung (Technische Universitat Clausthal) [3]. The visioplasticity method [2,25] was used to obtain the experimental data, and the numerical results were obtained by the model described in this report.

For all of the following examples, a plastic behaviour was adopted for the material ($\gamma = 0$ in (19)).

4.1 Example I: 2D hot rolling problem - Test validation

The hot rolling test chosen to perform the numerical simulation was named PROBE 40. The main geometrical conditions can be seen in table A-1 (See Appendix A). The geometry and boundary conditions for the numerical simulation were extracted from the experimental conditions, and they are sketched in Figure 4.1a. The finite element mesh for the problem can be observed in Figure 4.1b, and the deformed specimen used in the experiment is shown in Figure 4.1c.

4.1.1 Material properties

The Sellars-Tegart modified model (section 2.1.2) was used to interpolate the material properties at high temperature. Most values of the physical properties were taken from [3], and they are the following:

$$\begin{aligned} k &= 17.0 + 1.09 * 10^{-2} * T \quad (W/K.m) \\ a &= 4.80 * 10^{-6} - 0.70 * 10^{-9} * T + 1.64 * 10^{-12} * T^2 \\ c_p &= \frac{k}{\rho * a} \\ \rho &= 7.430 \; gr/cm^3 \end{aligned} \tag{72}$$

Also, the constant values for the constitutive model (see Section 2.1.2) are the following: $D = 40.79 \; N/mm^2$, $C = -520.06 \; N/mm^2$, $Q = 413.296 \; KJ/mol$. In addition, numerical simulations were also performed with $D = 15.44 \; N/mm^2$, $C = -85.04 \; N/mm^2$, $Q = 311.818 \; KJ/mol$ to investigate the sensibility of the model with respect to the material properties. All above values were taken from [3], and they correspond with two different values of strain.

Moreover, two friction coeficients between the slab and the roll surface $\xi = 0.35$ and $\xi = 0.04$ were taken.

The main variables compared were the velocity field, the temperature of the slab, the strain and strain rate invariant, the stress field and the rolling force and torque.

4.1.2 Velocity field

Figure 4.1.2a shows the normalized velocity distribution (v_i/v_0, $v_i = v_x, v_y, |v|$) along a line. In Figures 4.1.2b, 4.1.2c and 4.1.2d the same experimental results are plotted. Taking into account the diferent scales between numerical and experimental plots, and that the experimental measurements were taken along a flow line and the numerical results along a straight line, we can observe that both results are similar not only quantitatively but also qualitatively. The v_x/v_0 velocity component increases at the roll entrance, and slightly decreases at the exit due to material expansion. The v_y/v_0 component increases (in absolute value) at the roll entrance, and it raises at the exit (due to material expansion).

Figures 4.1.2e, 4.1.2f, 4.1.2g and 4.1.2h show the normalized velocity contours. Taking into account that the numerical results are presented only for one half of the slab, we can observe the coincidence between experimental and numerical velocity contours.

4.1.3 Temperature

Figures 4.1.3a and 4.1.3b show the numerical and experimental temperature results. Numerical results obtained with c_p and k calculated according to equation (72) (Figure 4.1.3a Top-Right), are close to experimental data (Figure 4.1.3b). The experimental temperature along slab surface falls down at the roll entrance due to the radiation between slab and roll. This phenomenon was not simulated numerically.

4.1.4 Strain

In Figure 4.1.4a Top-Left, we can observe the computations for the Von Mises strain distribution along a section (See Figure 4.1.2a Bottom-Right to identify the section). These results can be compared with these of Figure 4.1.4b where the experimental effective strain is plotted. Taking into account that the effective strain is equal to 2/3 the Von Mises strain and the graphic scales, we can observe that graphics are qualitatively and quantitatively similar.

In Figures 4.1.4c and 4.1.4d the numerical and experimental strain contours are respectively shown. Bearing in mind that the Von Mises strain is not equal to the effective strain (See above), and that the numerical contours are presented only for one half of the slab, we can observe that the experimental and numerical strain

contours are similar at the roll zone. However, the numerical contours present a strain concentration zone at the right top corner of the slab, this can be due to the differences in the friction coeficient or material properties.

4.1.5 Strain rate

In Figures 4.1.5a we show the numerical Von Mises strain rate along section A-A' (See Figure 3.1a to identify the section). This should be compared with results of Figure 4.1.5b, which shows the experimental effective strain rate. Normalizing the numerical strain rate, and taking into account the different graphic scales and the difference between Von Mises and effective strain rate (See 4.1.4), we can observe that numerical and experimental graphics are qualitatively and quantitatively similar.

In Figures 4.1.5c and 4.1.5d numerical and experimental strain rate contours are respectively shown. Both present a concentration zone at the first contact region between roll and slab. It can be observed that the numerical and experimental contours are quite similar, taking into account that the numerical results are presented only for one half of the slab.

4.1.6 Stresses

Figure 4.1.6a shows the stress variation along a section (See Figure 4.1.1a Bottom-Right to identify the section). Experimental data is shown in Figures 4.1.6b, 4.1.6c and 4.1.6d. In general the stresses calculated numerically are of the order of magnitude of those calculated by the visioplasticity method [3,25] (Observe the difference in units). In addition, the general graphic tendencies are similar (except for the experimental values of σ_x *or* $s11$ stress for which we believe the sign convention has been changed). In general, experimental stresses are smoother than numerical ones, this can be due to the fact that experimental stresses were calculated along the flow lines.

In Figures 4.1.6e to 4.1.6j the numerical and experimental stress contours are plotted. The stress concentration zones are similar in both cases, but the general contour shapes are not much alike.

4.1.7 Roll force and torque

Figure 4.1.7 shows the force and torque time evolution. The behaviour of

both variables coincide with that expected (See [7]). The experimental values are presented in Table A-1. The experimental F/M values are 89.82 (Bottom roll) and 102.84 (Top roll). The numerical final force and torque value computed using the stress field and the first group of constitutive law constants (See 4.1.1) are: $F = 29491\ N/cm$; $M = 326.48\ Nm/cm$, and $F/M = 90.33$. If we multiply the numerical values by the slab's width ($12.47\ cm$), the results are of same order of magnitude than experimental values. However, the force and torque magnitudes obtained can be changed by computing the stress field with the second constitutive law constants, this leads to numerical results very close to experimental data. For this last case, the friction coeficient was $\xi = 0.04$ (The friction factor for both cases was $m = 1.0$). The numerical and experimental rolling force and torque multiplied by slab's width $12.47cm$ are:

Experimental	Numerical
$F = 0.630\ MN$	$F = 0.513\ MN$
$M = 7014.2\ NM - 6126.1\ NM$	$M = 6643.8\ NM$

Thus, the rolling force and torque present a strong dependency with respect to the constitutive law. This is confirmed in the next numerical example.

4.2 Example II: 2D hot rolling problem

In this example we will show the influence of different constitutive laws in force and torque calculation and the behaviour of friction elements. Also, the free surface and microstructural changes computation will be presented.

The geometry and boundary conditions are equal to the Example I above. The constitutive laws that we will use are not only strain rate and temperature dependent, but also strain dependent. These are the Hajduk model (equation (6), and the modified Sellars-Tegart model (equation (12)) with the following strain dependent constants [3]:

$$\begin{aligned} D[N/mm^2] &= 4.5986 + 236.63\bar{\varepsilon} - 554.17\bar{\varepsilon}^2 + 562.53\bar{\varepsilon}^3 - 202.80\bar{\varepsilon}^4 \\ C[N/mm^2] &= 84.122 - 3902.6\bar{\varepsilon} + 10617.0\bar{\varepsilon}^2 - 14917.0\bar{\varepsilon}^3 + 7882.6\bar{\varepsilon}^4 \\ Q[KJ/mol] &= 320.61 + 220.75\bar{\varepsilon} + 250.58\bar{\varepsilon}^2 - 378.86\bar{\varepsilon}^3 \end{aligned} \tag{73}$$

Above equations are valid for $0.5 < \dot{\bar{\varepsilon}} < 650\ s^{-1}$ and for $0.05 < \bar{\varepsilon} < 0.8$. For the lower bound, $0.5 < \dot{\bar{\varepsilon}}$ and $0.05 < \bar{\varepsilon}$, a cut-off value of $\mu = 10^5\ N \cdot s/cm^2$ was taken for the viscosity; for $\bar{\varepsilon} \geq 0.8$ the following values were taken for the constants: $D = 44.16\ N/mm^2$, $C = -652.01\ N/mm^2$, $Q = 460.894\ KJ/mol$ and for $\bar{\varepsilon} \leq 0.05$ $D = 15.44\ N/mm^2$, $C = -85.04\ N/mm^2$, $Q = 311.818\ KJ/mol$. For the case $\dot{\bar{\varepsilon}} \geq 650\ s^{-1}$ a cut-off value of $\dot{\bar{\varepsilon}} = 650\ s^{-1}$ was done.

The Hajduk model constants were taken from [2], these were (see equation (6)): $A_1 = 17.07$, $m_1 = 0.00284$, $A_2 = 1.647$, $m_2 = 0.217$, $A_3 = 0.789$, $m_3 = 0.104$, $K_0 = 166.2\ N/mm^2$, $\bar{\varepsilon}_0 = 0.4$.

4.2.1 Stress fields

In Figures 4.2.1a and 4.2.1b we show the stress fields using the constitutive law referenced above. In general, the stress field obtained with the Hajduk model is of one order of magnitude greater than this obtained with modified Sellars-Tegart model. This can be due to the fact that the computed yield stress with Hajduk model is greater than that computed with the modified Sellars-Tegart model. This is confirmed in Figure 4.2.1c, where it can be observed that even the equivalent strain rate is equal for both model, the viscosity is higher for the Hajduk model (see equation (19)).

Therefore, the computed rolling force and torque are higher for Hajduk model than for modified Sellars-Tegart model. These are:

Hajduk model	Mod.Sellars-Tegart
$F = 4.623\ MN$	$F = 0.353\ MN$
$M = 54192\ NM$	$M = 4140.1 NM$

This shows the strong dependence between the rolling force and torque and the constitutive law. As a final remark, it can be observed that if the deviatoric stress field in XX and YY directions (Figure 4.2.1a) are added, the resultant field is practically zero, which confirms the material incompressibility (see equation (18)).

4.2.2 Behaviour of friction elements

In this section is showed the behaviour of both friction approaches: i.e. Avitzur Coulomb and Lubricant approach. For the simulation of both friction approaches,

the modified Sellars-Tegart constitutive law (with the parameters presented in Section 4.2) was used. The friction parameter's values for Avitzur model were $\xi = 0.1$, $m = 1.0$ and the lubricant viscosity was $\mu_0 = 10^7$.

Figure 4.2.2a shows the velocity vertical profiles (at roll inlet and outlet) produced by both friction approaches. The two friction elements simulate very well the velocity jump between the roll and metal surfaces (one surface slips over the other).

Figures 4.2.2b and 4.2.2c display the stress along the contact surfaces (roll surface and metal surface), using the different friction elements implemented in this work. The shear stress computed using the lubricant approach (Figure 4.2.2b bottom-left) is smoother than that computed using the Avitzur Coulomb approach (Figure 4.2.2b top-left). In addition, the former is more realistic from a physical point of view. At the inlet section, the metal is pushed into the roll and high shear stresses develop; then the metal accelerates due to the incompressibility and the shear stress decreases. The pressure fields are quite similar for both approaches (Figure 4.2.2b top and bottom-rigth). On the other hand, the distribution of deviatoric horizontal and vertical stresses is quite different for both approaches (Figure 4.2.2c). For the lubricant approach, these stresses satisfy the material incompressibility in a better manner ($\tau_{xx} + \tau_{yy} = 2\mu\nabla \cdot \mathbf{u} = 0$).

The rolling force and torque are similar for both friction approaches, these are:

Avitzur Coulomb	Lubricant
$F = 0.348\ MN$	$F = 0.353\ MN$
$M = 4828\ NM$	$M = 4140\ NM$

The rolling force and torque present a stronger dependency respect to the constitutive law than respect to the friction parameters. The magnitude order of the rolling force and torque is the same for different friction parameters (This does not happen for different constitutive laws, as shown in section 4.2.1). For the lubricant approach using different lubricant viscosity μ_0 the following values are obtained:

$\mu_0(dy.s/cm^2)$	$Force(MN)$	$Torque(NM)$
10^8	0.346	4355.3
10^6	0.356	3164.7

For the Avitzur Coulomb approach using different Coulomb's coefficients the

following values are obtained:

ξ	$Force(MN)$	$Torque(NM)$
0.10	0.348	4828.0
0.04	0.349	3321.2

However, non-realistic roll stress distributions are obtained if an incorrect friction parameter is chosen. This can be observed in Figure 4.2.2d, where the shear stress increases at outlet section (Figure 4.2.2d bottom-left) which does not make physical sense. Furthermore, the velocity profile at the outlet section (Figure 4.2.2d top-right) indicates that metal is still pushed by roll, which does not agree with experimental evidence.

4.2.3 Computation of free surface

Figure 4.2.3 shows the free surface evolution using the Lagrangian and the Eulerian methods. It can be observed that the position of the material front is basically the same for both methods. However, the Lagrangian method provides information about the displacement and strain field at each time step. In addition, the Eulerian method presents numerical problems in some cases due to the parabolic differential equation that has to be solved. Problems like numerical oscillation in zones where velocity field is almost perpendicular to the pseudo-concentration gradient, and the difficulties to identify the inflow (Γ_i see equation (23b)) at each time step to prescribe the pseudo-concentration, are critical in the 3D case as it will be presented in the next numerical example.

4.2.4 Microstructural changes

In Figure 4.2.4a can be observed the grain size distribution due to static recrystallization for several time steps (Note that at the material front position, the fictitious fluid grain size is zero). The parameter values for Sellars-Tegart model were [2] $a = 0.8$, $A = 4.9 \cdot 10^{-4}$, $d_0 = 300[\mu M]$, $n = 0.15$, $D = 0.5[\mu M]^{0.33}$, $B = 2.5 \cdot 10^{-19}$, $B' = 1.06 \cdot 10^{-15}$, $p = 2$, $q = 0$, $r = -0.6$, $Q_{rex} = 300[KJ/mol]$, $A' = 5.02 \cdot 10^{53}$ for $T < 1000^\circ C$ and $A' = 3.87 \cdot 10^{32}$ for $T \geq 1000^\circ C$, and $Q_{gg} = 914[KJ/mol]$ and $400[KJ/mol]$ respectively for the same cases that A'.

At the roll section, no recrystallization is presented due to the high strain rate values. After deformation, recrystallization occurs due to the high temperature and residual strain and low strain rates. Figure 4.2.4b shows the values of temperature, equivalent strain, equivalent strain rate and grain size for time 0.30s.

This values confirm the experimental result: the higher the temperature is, the larger the strain and the lower the strain rate are, and also more recrystallization occurs [2]. Finally, the surface grain size is larger than the interior grain size, due to the temperature distribution. This also agrees with experimental evidence [26].

4.2.5 Other results

Figure 4.2.5 shows the velocity, viscosity and equivalent strain rate fields for time=0.40s. The viscosities are lower at the roll section where high equivalent strain rate values occur, which is agree with the theory. Cut-off values for the viscosity are imposed at zones where the strain rate values are small to avoid ill conditioning of the equations (See eq. (19)).

4.3 Example III: 3D hot rolling problem

The principal aim of this example is to show the advantages of the Lagrangian method to compute the free surface position for 3D hot rolling problems. Also, some other 3D results are shown.

The geometry and spatial mesh of the problem is presented in Figure 4.3. due to symmetry, only one quarter of the slab is simulated. The initial and boundary conditions are similar to the 2D case presented above. The modified Sellars-Tegart model, with the same parameter's values chosen for Example II, was adopted.

4.3.1 Free surface and displacement time evolution

Figure 4.3.1a shows the free surface evolution using the Lagrangian method. In Figure 4.3.1b the same result is presented with the Eulerian method. The Lagrangian method gives more realistic slab shapes than the Eulerian one. In addition, the Eulerian method presents numerical oscillation at the front of the slab. This can be due to the fact that the velocity is almost perpendicular to the surface tracking in the "z" direction.

In Figure 4.3.1c the deformed lagrangian mesh at differents time step can be observed. The displacement field and the strain tensor are obtained from this deformed mesh. Also, the final slab shape is obtained.

4.3.2 Stress field

Figure 4.3.2 displays the stress and pressure fields at the contact surface (roll and metal). The results are very realistic, and the incompressibility constraint is satisfied (see plots for deviatoric stress XX and deviatoric stress YY). The shear stress behaviour is analogous to the 2D case. In the first part the metal is pushed into the roll (high shear stress), after the metal increases the velocity due to the incompressibility and the shear stress decreases. Also, the pressure field is very realistic; it presents high positive values at the roll section, and high negative values at inlet and outlet section. This negative values are due to the metal expansion (swelling effect).

4.3.3 Other results

Figure 4.3.3 shows the temperature, velocity, viscosity and equivalent strain rate fields at time=0.20s. The behaviour of these fields are similar to the 2D cases.

5. CONCLUSIONS

In general, the finite element model developed for hot rolling processes provides results that are according to the problem's physics and close to the experimental data. The principal variables: velocity, temperature, and displacement fields, present a good behaviour. Several constitutive laws for metals at high temperature have been implemented and evaluated. Two friction approaches have been considered and a model to computed microstructural changes has been implemented. The principal conclusion from the numerical examples are shown below.

The stress and pressure fields depend on the chosen model to interpolate high temperature properties of metals. The Hajduk model yields to stresses values larger than the modified Sellars-Tegart model. However, both model present similar strain, strain rate and temperature fields. Then, the differences are due to the fact that the yield stress computed with the Hajduk model is larger than that computed with the modified Sellars-Tegart model. This conclusion are so far only valid for the parameter's values used in this work.

The roll's force and torque present values are very close to the experimental data. These values strongly depend on the chosen constitutive law. In general,

the modified Sellars-Tegart model to compute the yield stress at high temperature values leads to force and torque results closer to the experimental data.

The strain rate and viscosity fields present a good behaviour. Large strain rate and small viscosity values are obtained at the roll section. This makes physical sense.

Both friction elements provide velocity profiles and stress distributions that also make physical sense. The friction parameters can be varied in a short range to adjust the roll's force and torque values. However, these valuse are not strongly dependent on friction parameters, i.e., large friction parameter variations result in small force and torque variations. Finally, even though both friction approaches produce similar values of force and torque, the stress distribution at the roll surface is smoother and more physical for the lubricant approach than for the Avitzur Coulomb model.

The free surface computation using the Lagrangian method provides better results than the Eulerian method in the 3D case. This first approach shows good behaviour for slow creeping flows. In addition, with the Lagrangian methodology the displacement and strain fields can be computed and the numerical problems of the Eulerian method are avoided. Computations of the equivalent strain field using an Eulerian approach presents the same problems than the Eulerian free surface. The equation to be solved is parabolic and the avoidance of numerical oscillations requires the definition of a smooth initial equivalent strain field [9], which does not make much physical sense. In addition, the inflow has to be calculated at each time step to prescribe the equivalent strain, which is not trivial for 3D cases. Moreover, the strain field computation using the Lagrangian method presents good results and avoids the problems of Eulerian method. In addition, the non-linear part of the strain tensor can be easily computed.

Computation of the microstructural changes (grain size) can be performed very easily from the thermomechanical variables given by the finite element model. The grain size distribution agree with the experimental evidence, i.e., the austenitic grain size is larger at the surface of the slab than in the interior. Moreover, the recrystallization results are directly proportional to the temperature and the strain fields, and inversely proportional to the strain rate field.

In conclusion, the numerical formulation developed and the corresponding computer code for the analisys of hot rolling processes seems to be a powerful tool for enhanced design and analisys of practical hot rolling operations.

ACKNOWLEDGEMENTS

The authors acknowledge the support received from the Brite-Euram programme of EEC and the Ministerio de Industria Espanõl through the CONFOSIM project.

REFERENCES

[1] L.E.MALVERN. "Introduction to the Mechanics of Continuous medium", Prentice Hall 1969.

[2] T.RODICK. *"Numerical Analysis of Thermomechanical Processes during Deformation of Metals at High Temperature"*, Ph.D. Thesis. University of Wales, 1989.

[3] R.KRENGEL. "Untersuchung des Warmwalzprozesses mit der visioplastischen Methode",IWU-Bericht 9. Institut Fur Werkstoffumformung, 1988.

[4] O.C.ZIENKIEWICZ, P.C.JAIN and E.OÑATE. "Flow of solids during forming and extrusion: Some aspects of numerical solution", *Int.J.Solids Structures*,1978,Vol.14,15-38

[5] O.C.ZIENKIEWICZ, E.OÑATE and J.C.HEINRICH. "A general formulation for coupled thermal flow of metals using finite elements", *Int.J.For Numerical Methods in Engineering*,1981,Vol.17,1497-1514

[6] R.CODINA. *"A Finite Element Model for Incompressible Flow Problems"*, Doctoral Thesis. UPC Barcelona, 1992.

[7] O.SOTO, E.OÑATE and R.CODINA. "Simulación numérica del proceso de laminado de metales en caliente, Informe Técnico CIMNE No.IT-67, junio 1992.

[8] I.G.CURRIE "Fundamental Mechanics of Fluids, McGraw-Hill 1974.

[9] E. DVORKIN and E. PETOCZ. "On the modelling of 2D metal forming processes using the flow formulation and pseudo-concentrations technique", COMPLAS III Conference, Barcelona 1992.

[10] J.M.WARREN *"The Analysis of Extrusion and Deep-Drawing Processes using*

the Finite Element Method", Ph.D. thesis. University of Wales, 1987.

[11] E. THOMPSON. "Use of the pseudo-concentrations to follow creeping viscous flows during transient analysis", *Int.J.for Numerical Methods in Fluid.* 1986, Vol.6,749-761.

[12] E. THOMPSON. "Transient analysis of metal forming operations using pseudo-concentrations", NUMIFORM 86 Conference, Gothenburg 25-29 August 1986.

[13] E. THOMPSON. "Transient analysis of forging operations by the pseudo-concentration method", *Int.J.for Numerical Methods in Engineering.* 1988, Vol.25,177-189.

[14] C.CUVELIER and A.SEAGAL. "Finite Element Methods and Navier Stokes Equations",D.Reidel Publishing Company,Dordrecht,Holland,1986.

[15] R.CODINA. "A Finite Element Formulation for Viscous Incompressible Flows", Monografia CIMNE No.16, January 1993.

[16] R.CODINA, U.SCHAFER, E.OÑATE, M.CERVERA and O.SOTO. "A Finite Element Model to Track Free Surfaces of Viscous Incompressible Flows, Congreso Internacional de Mecánica Computacional, Concepción Chile, 1992.

[17] R.CODINA, U.SCHAFER and E.OÑATE. "Mould filling simulation using finite elements", Publicación CIMNE No.24, diciembre 1992.

[18] R.CODINA, E.OÑATE and M.CERVERA. "A penalty finite element method for non-Newtonian creeping flows",CIMNE Report No.13,1991.

[19] E.OÑATE, F.QUINTANA, R.CODINA and J.MIQUEL. "Finite element formulation for incompressible and compressible flows",Publicación CIMNE No.14, October 1991.

[20] O.C.ZIENKIEWICZ and R.L.TAYLOR. "The Finite Element Method",Fourth Edition. Vol,2. McGraw-Hill,1989

[21] G.C.CORNFIELD and R.H.JOHNSON. "Theorical prediction of plastic flow in hot rolling including the effect of various temperature distributions", *Journal of the Iron and Steel Institute*, August 1973,567-573.

[22] O.SOTO, E.OÑATE and R.CODINA. "Rolling Test Numerical Validation

Performance", Informe CIMNE n.22, Enero,1993.

[23] CIMNE "programa CIMROLL- Manual del usuario", Informe técnico CIMNE IT-93, marzo 1993.

[24] O.C.ZIENKIEWICZ and K.MORGAN. "Finite Element and Approximation", John Wiley and Sons, Inc. 1983.

[25] NATSUO HATTA and JUN-ICHI KOKADO. "Analysis of stress in block during rolling by visioplasticity method", 1979.

[26] H.C.BOWLES, C.D.MERCER and J.B.MARTIN. "Numerical simulation of recrystallization during hot rolling", Report No.179 CERECAM, University of Cap Town, South Africa, January 1992.

[27] J.H.BEYNON, A.R.S.PONTER C.M.SELLARS. "Metallographic verification of computer modelling of hot rolling", Proceedings of the Euromech 233 Colloquium, Sophia Antipolis, France, August 29-31, 1988.

[28] J.P.CESCUTTI, E.WEY and J.L.CHENOT "Finite element calculation of hot forging with continuous remeshing", Proceedings of the Euromech 233 Colloquium, Sophia Antipolis, France, August 29-31, 1988.

APPENDIX I. TABLES AND FIGURES.

1 **********

PROBENNUMMER	:	PROBE 39/40	
ABMESSUNGEN VOR DER UMFORMUNG : DICKE	:	24.10	MM
GESAMTBREITE	:	124.70	MM
BREITE NR 39	:	62.30	MM
BREITE NR 40	:	62.40	MM
ABMESSUNGEN NACH DER UMFORMUNG : DICKE	:	20.15	MM
GESAMTBREITE	:	126.15	MM
BREITE NR 39	:	63.05	MM
BREITE NR 40	:	63.10	MM
BERASTERTE PROBENHAELFTE	:	40	
RASTERGROESSE	:	1.00 * 1.00	MM
RASTERAUFBRINGUNG MIT	:	KODAK KTFR 1 : 3	
RASTER-AETZUNG	41.8 G FECL36H20 AUF 100 ML H20 / 39 BAUME		
ZWISCHENSCHICHT	BAYER LEUKONIN BLAU : GROSSE DICKE/TROCKEN		
RASTER-RAUHTIEFE : VOR	:	*****	
NACH	:	*****	
SCHUTZGAS (TECHNISCH REIN)	:	LINDE ARGON 4.8	
OFENTEMPERATUR	:	1200	C
HEIZBEGINN	:	11.10	UHR
HEIZENDE	:	11.55	UHR
ERWAERMUNGSZEIT	:	45	MIN
ABKUEHLUNG AN LUFT AUF	:	1000	C
UEBERSETZUNG	:	13.6 : 1	-
WALZENRADIUS	:	146.5	MM
MOTORDREHZAHL (BEIDE ANTRIEBE)	:	200	UPM
UMFANGSGESCHWINDIGKEIT WALZE	:	0.2256	M/S
HYDRAULIKDRUCK FLACHZYLINDER	:	400	BAR
HYDRAULIKDRUCK HUBZYLINDER	:	100	BAR
LUMISCRIPT :			
PYROMETER TEMPERATUR EIN	:	955.0	C
PYROMETER TEMPERATUR AUS	:	970.0	C
WALZKRAFT	:	0.630	MN
DREHMOMENT UNTEN	:	7014.2	NM
DREHMOMENT OBEN	:	6126.1	NM
WALZGUTGESCHWINDIGKEIT EIN	:	0.1948	M/S
WALZGUTGESCHWINDIGKEIT AUS	:	0.2473	M/S
GEMESSENE WALZENDREHZAHL	:	14.35	UPM

X/Y-SCHREIBER :

ZEIT [S]	TEMPERATUR [C]	OBEN	MITTE	UNTEN
0.0	OFENAUSTRITT	1200	1200	1200
42.0	ABKUEHLUNG	1050	1050	1010
52.1	BEGINN WALZSPALT	1010	1020	970
-	MINIMUM-WALZSPALT	935	1015	940
53.7	ENDE WALZSPALT	950	1000	940

GESAMT-WALZZEIT : 1.7 [S]

Table A-1: Experimental conditions.

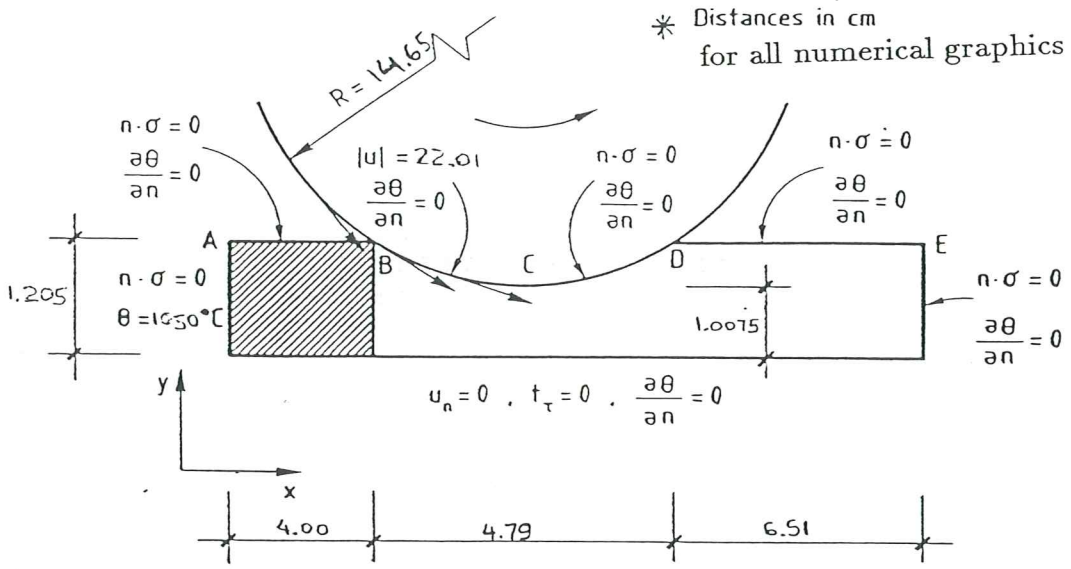

Figure 4.1a Geometry and boundary conditions.

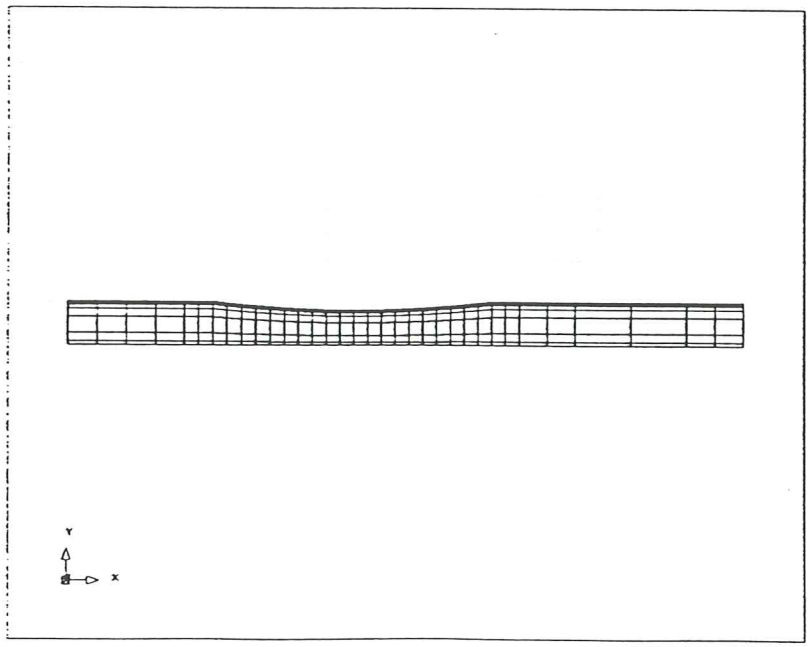

Figure 4.1b Finite element mesh (210 Q2/P1 elements, 903 nodal points).

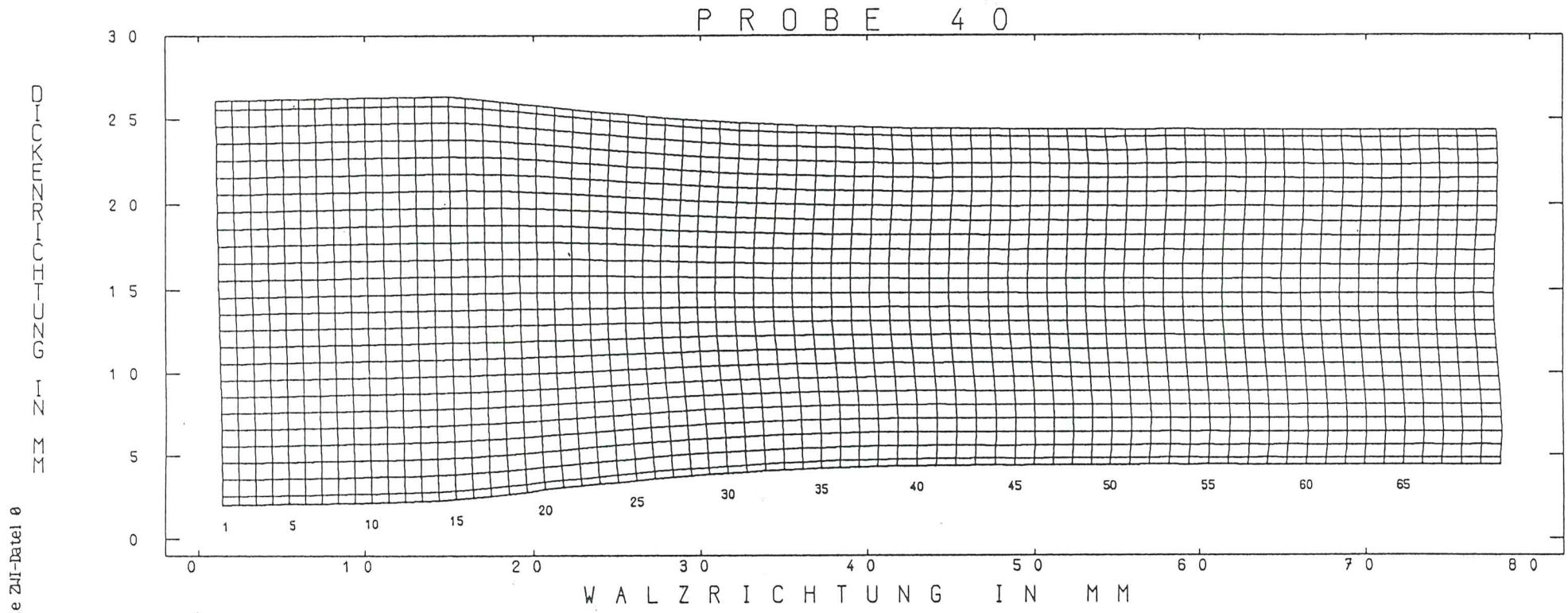

Figure 4.1c Deformed specimen.

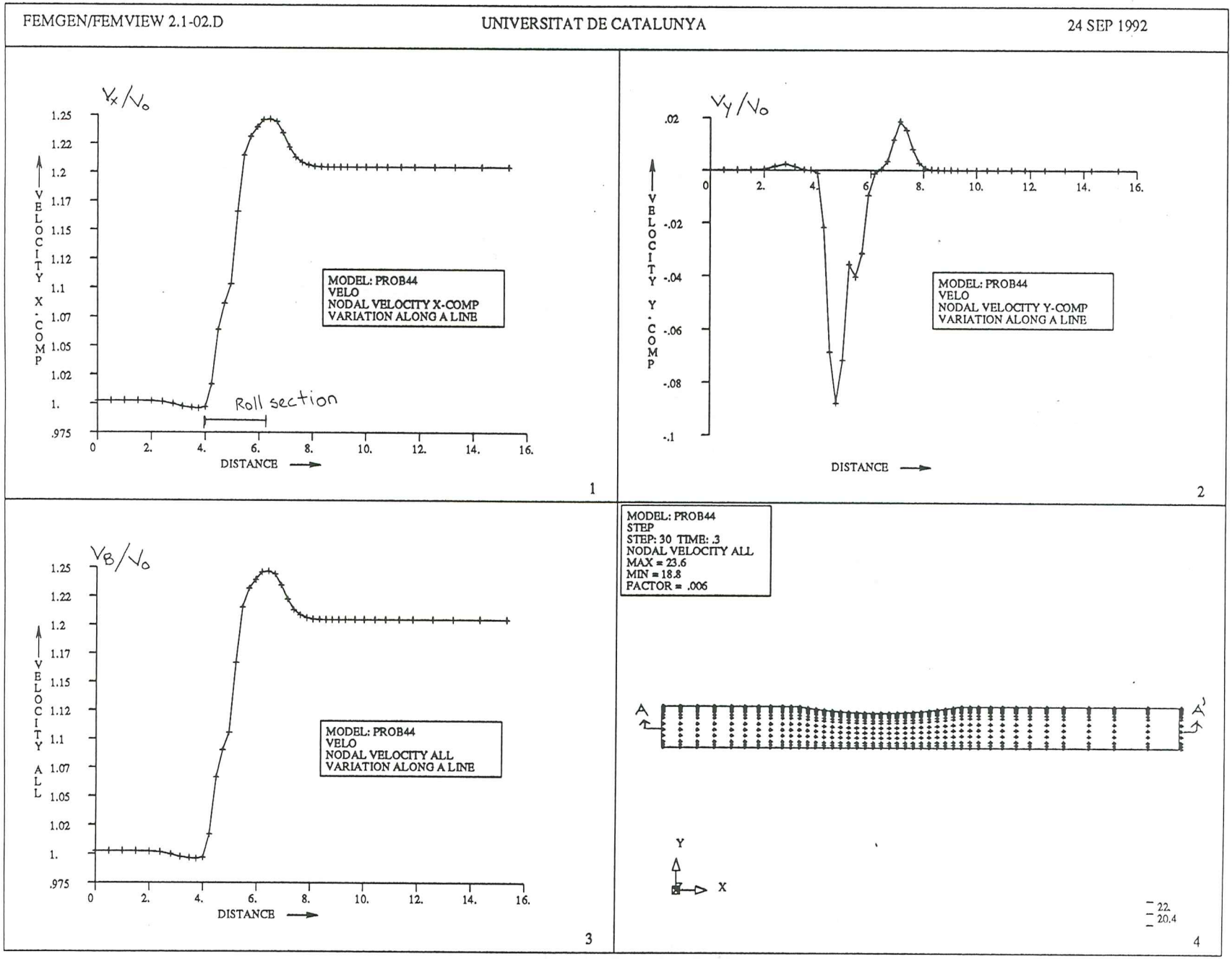

Figure 4.1.2a Numerical normalized velocity (Variation along section A-A').

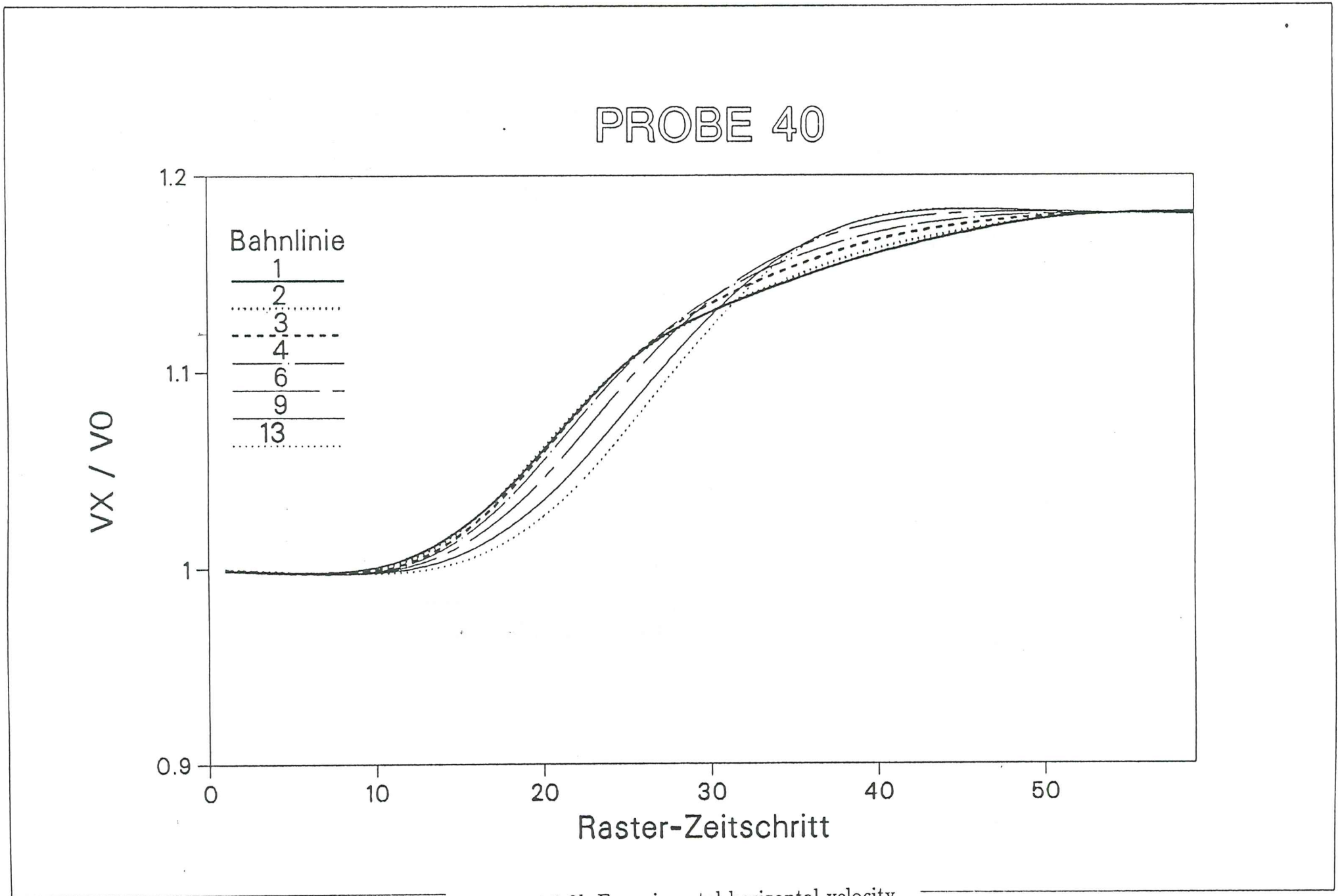

Figure 4.1.2b Experimental horizontal velocity.

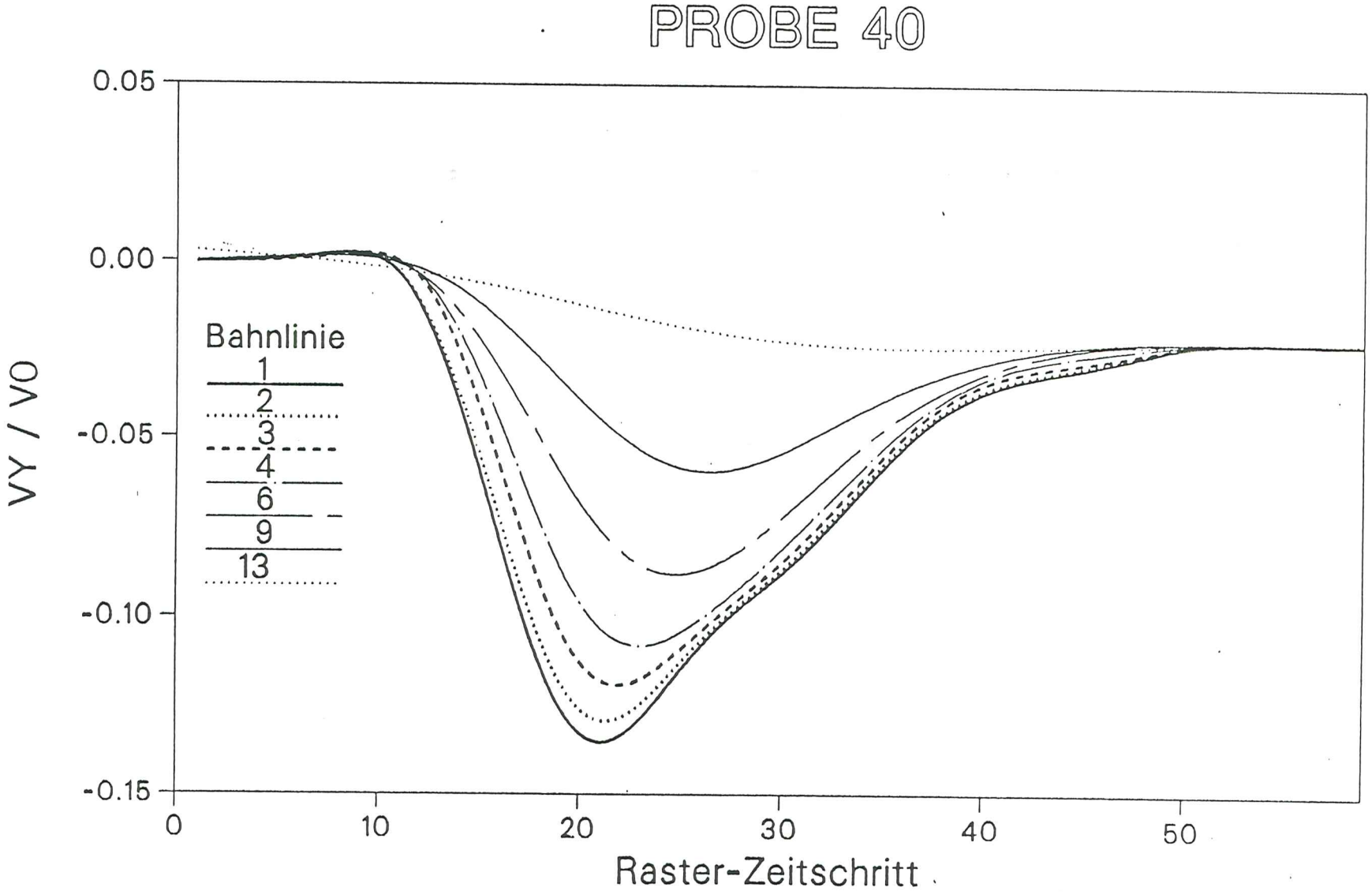

Figure 4.1.2c Experimental vertical velocity.

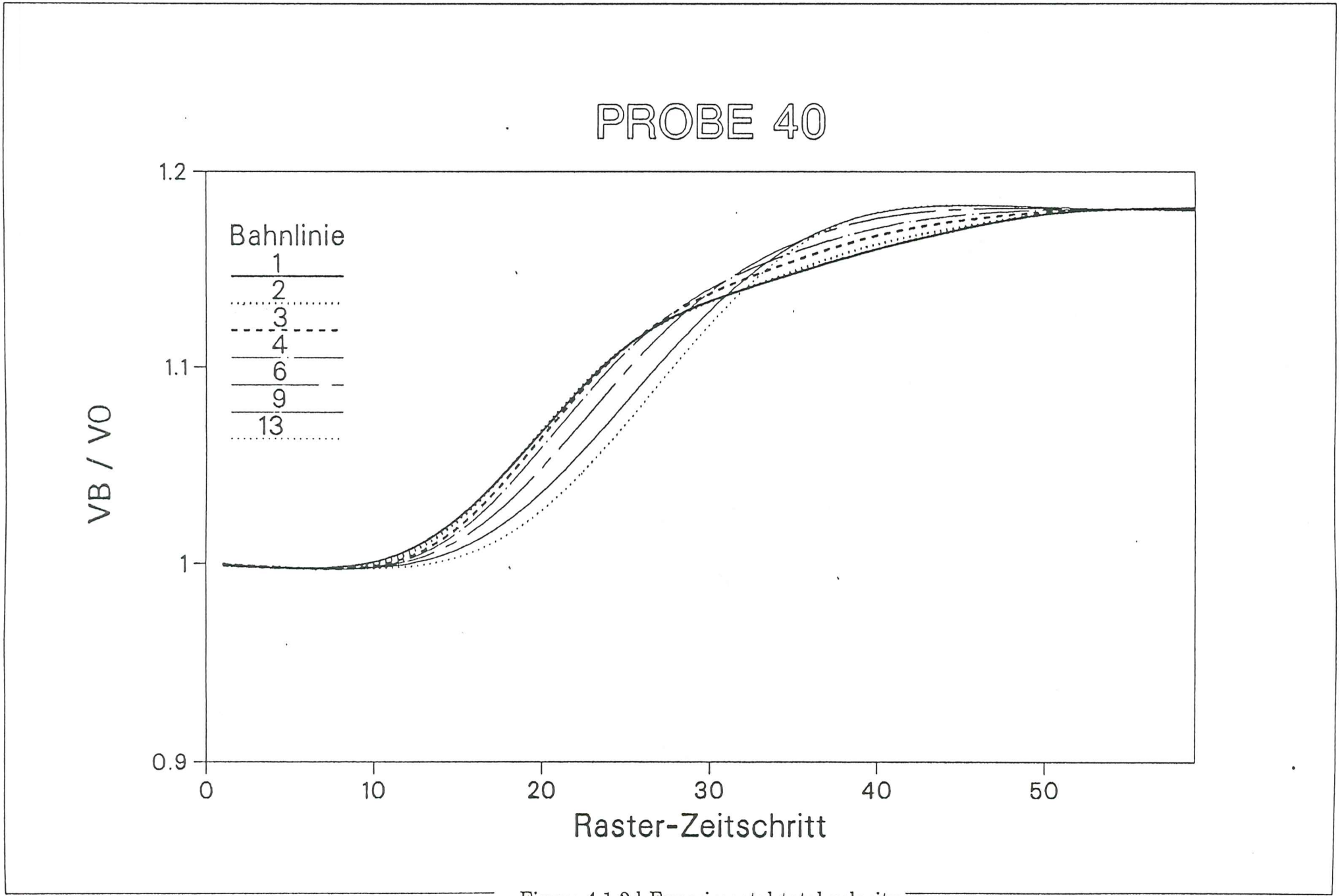

Figure 4.1.2d Experimental total velocity.

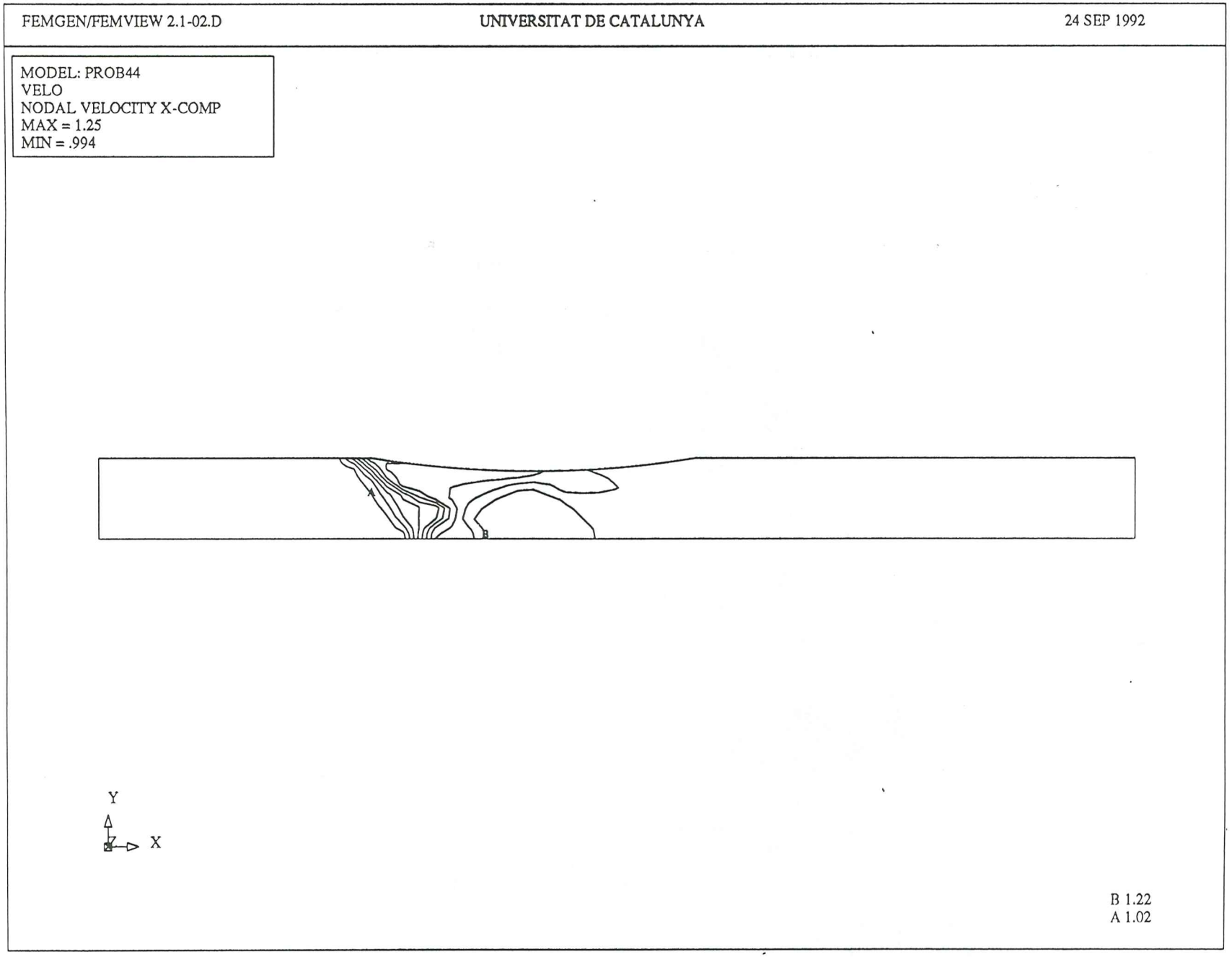

Figure 4.1.2e Numerical horizontal velocity contours.

PROBE 40

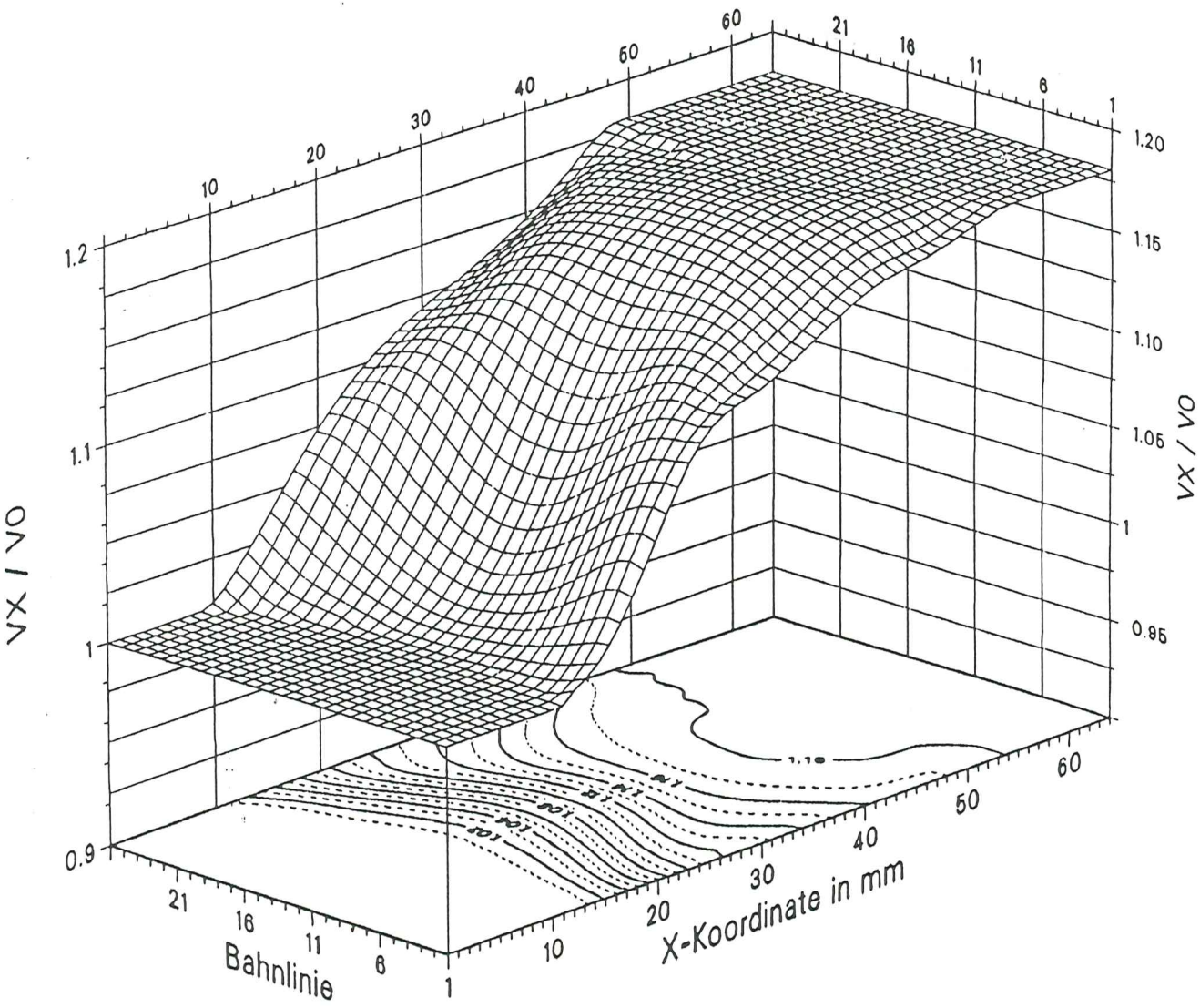

Figure 4.1.2f Experimental horizontal velocity contours.

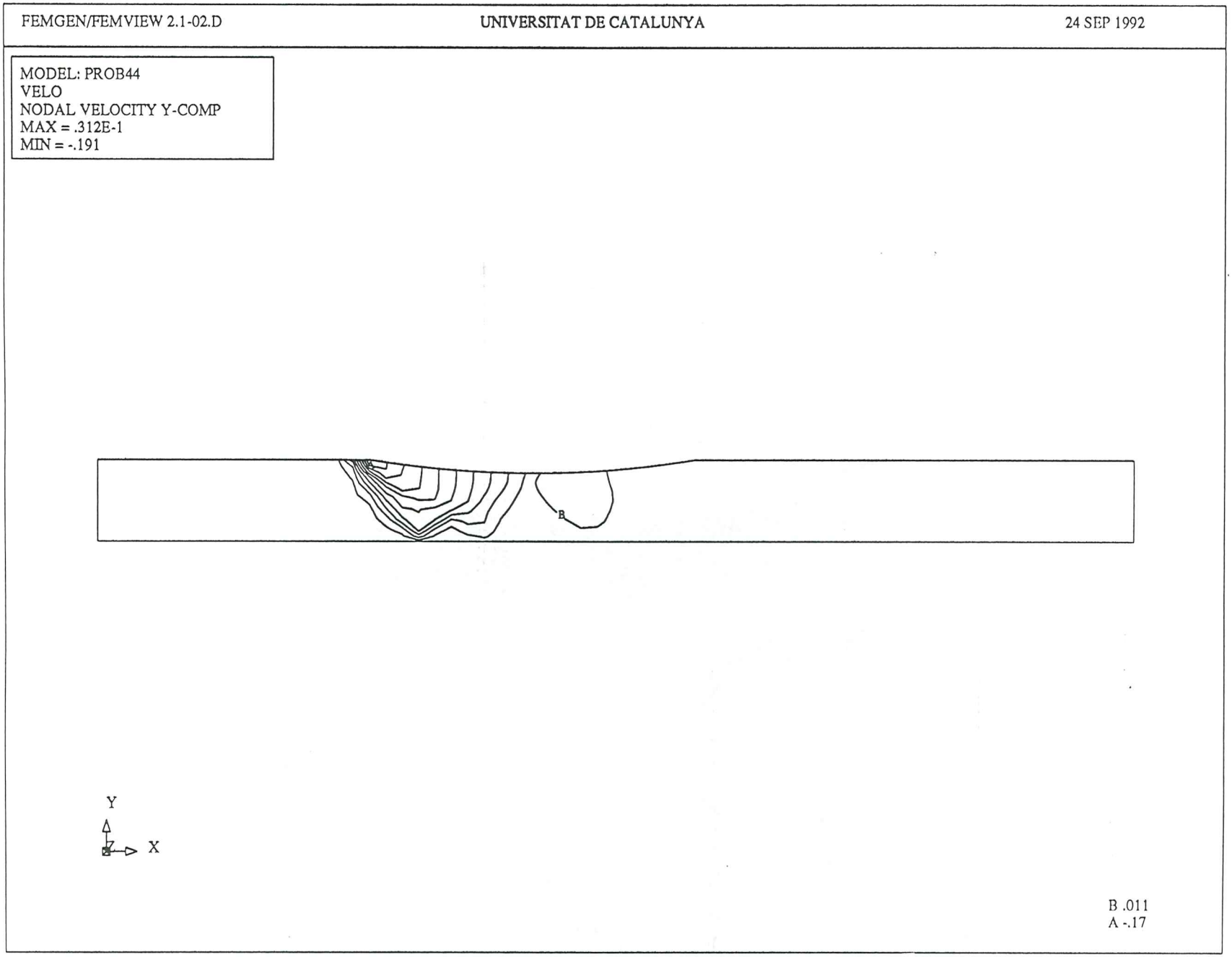

Figure 4.1.2g Numerical vertical velocity contours.

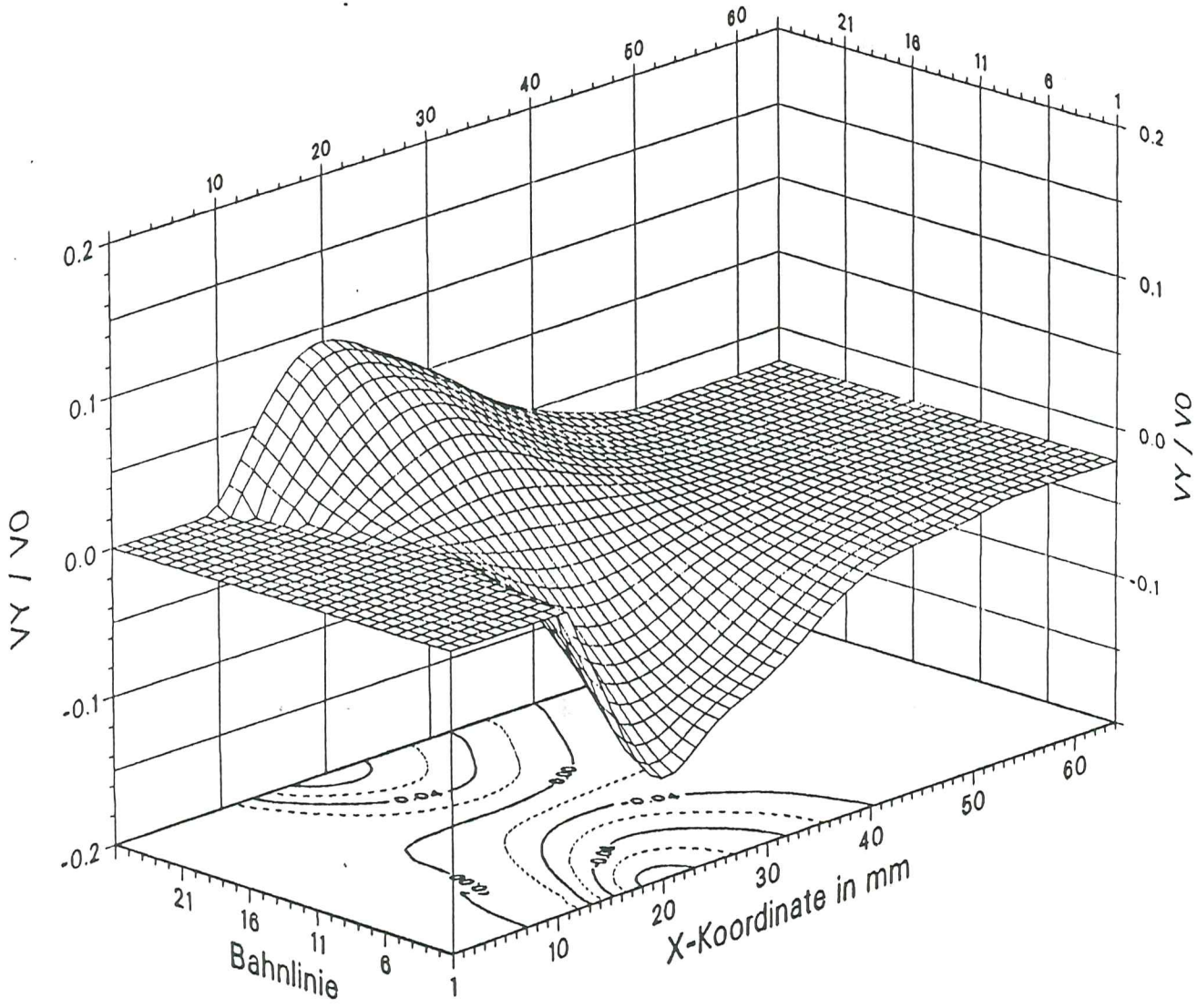

Figure 4.1.2h Experimental vertical velocity contours.

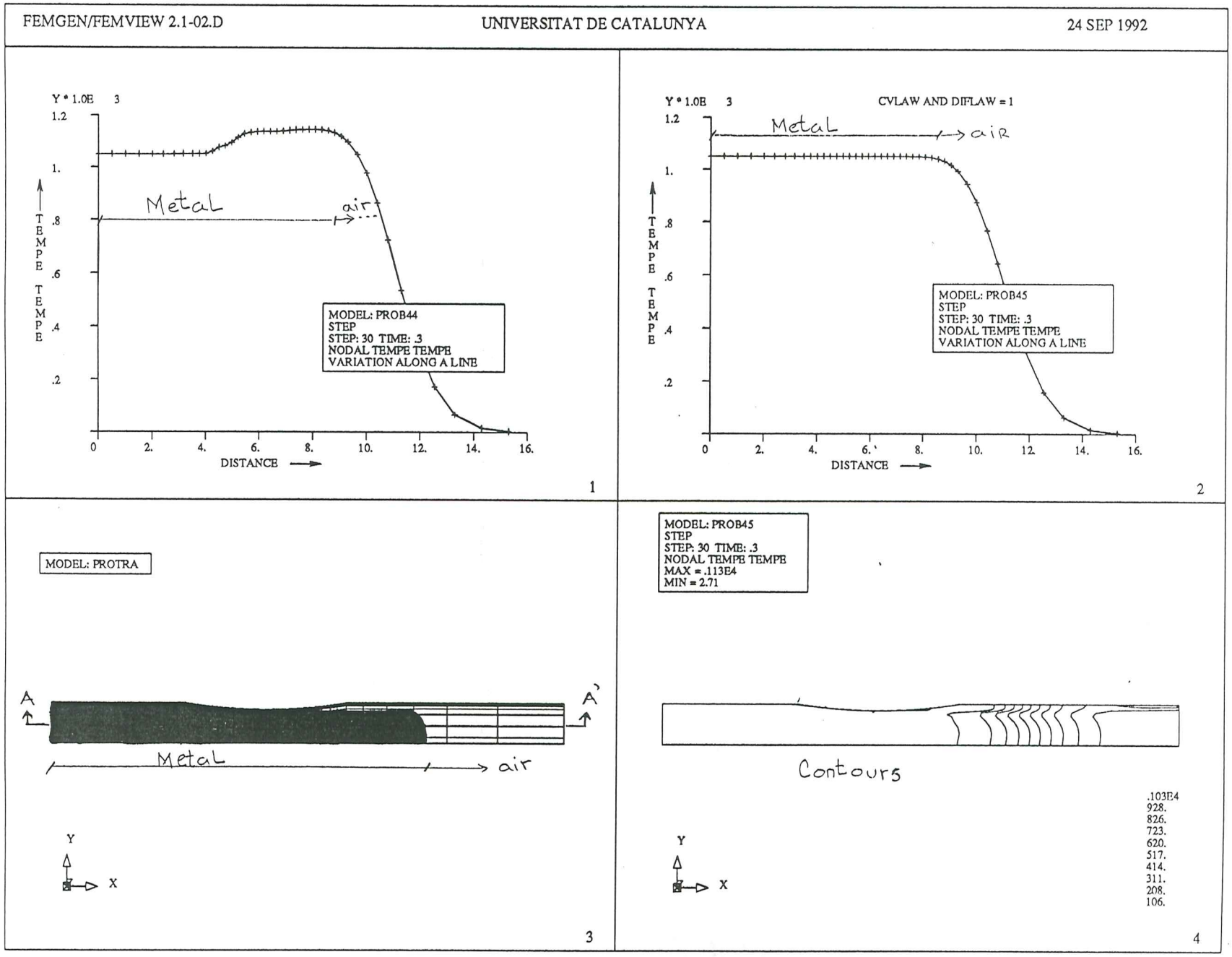

Figure 4.1.3a Numerical temperature (Variation along section A-A').

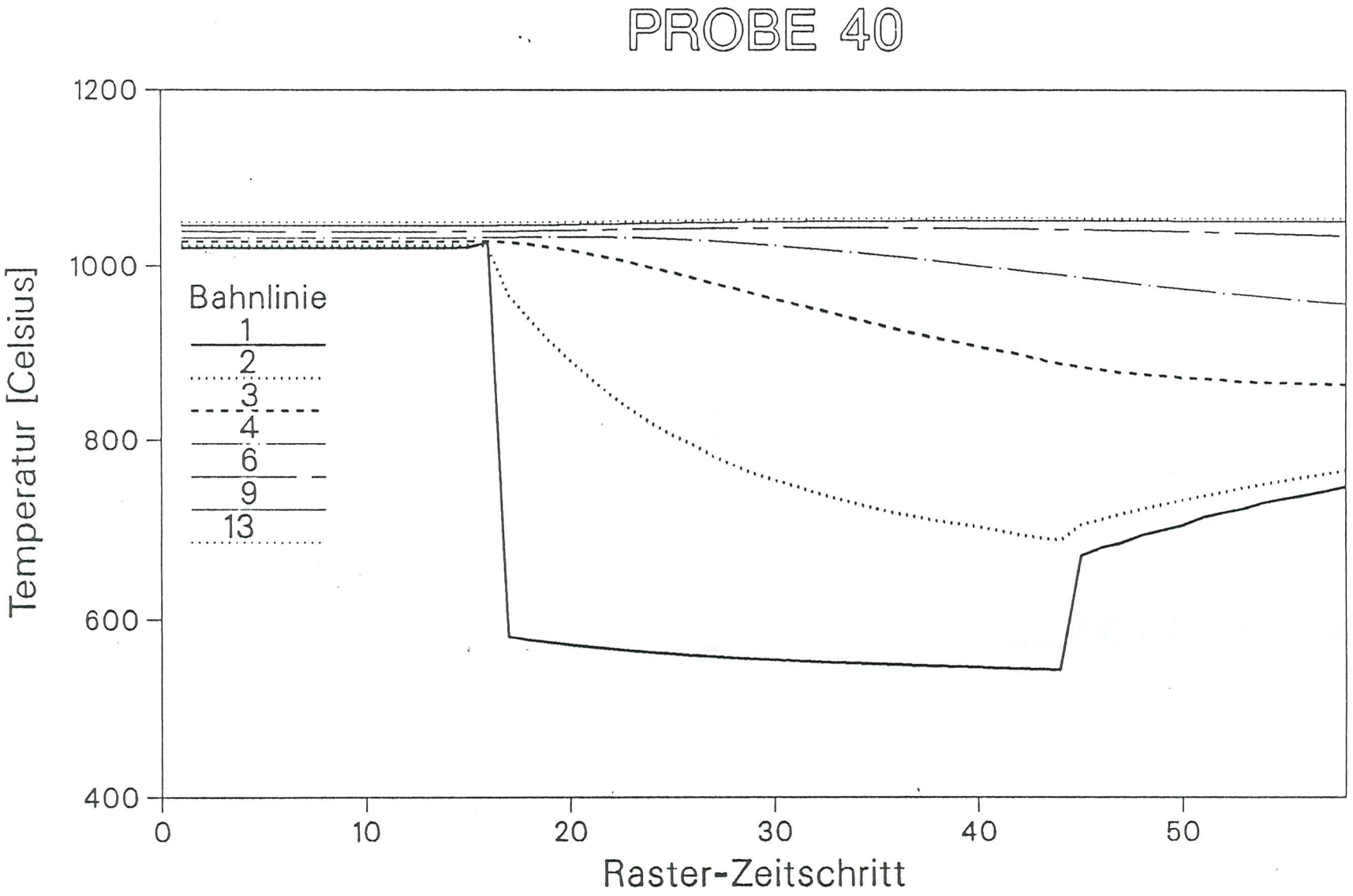

Figure 4.1.3b Experimental temperature.

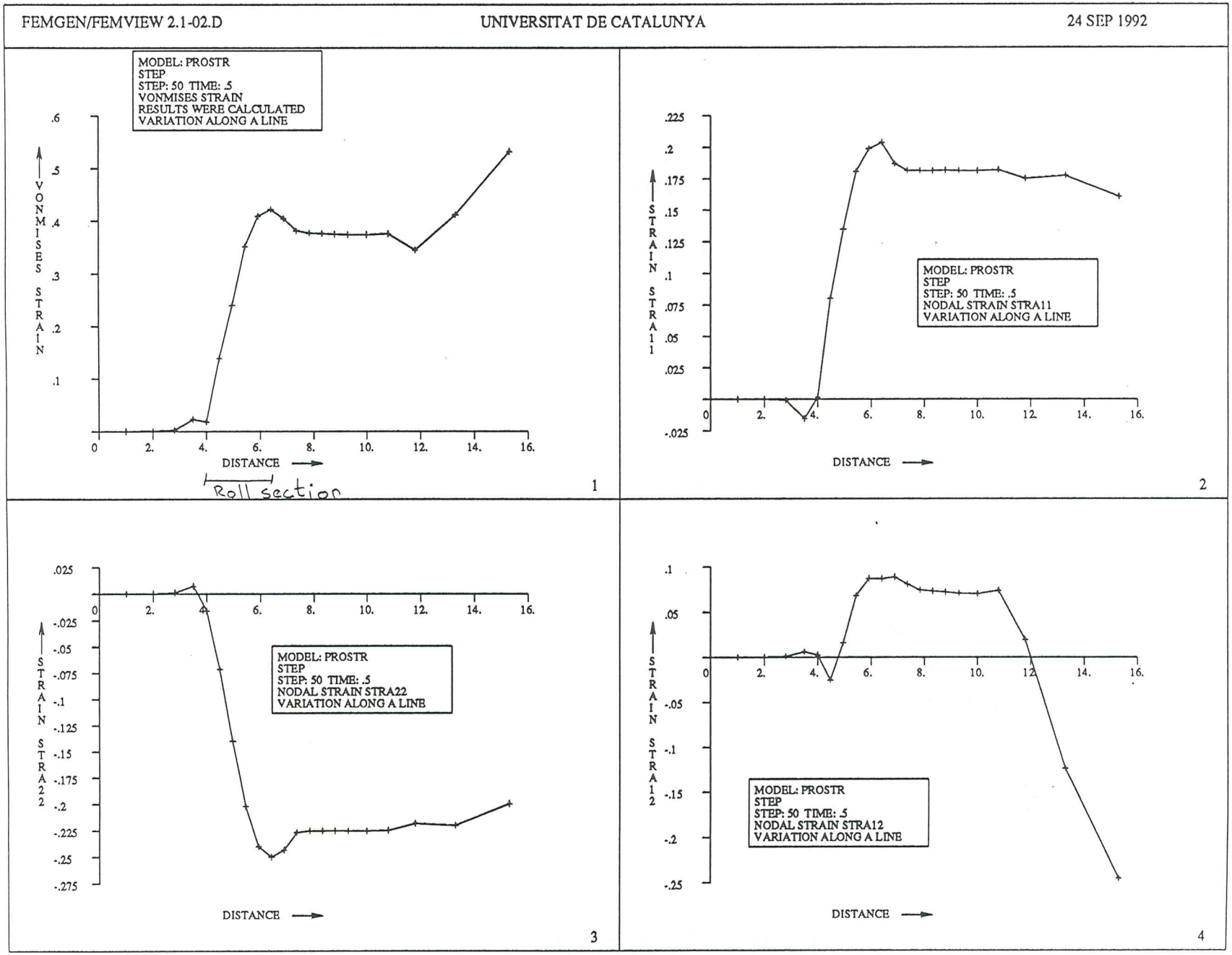

Figure 4.1.4a Numerical strain (Variation along section A-A').

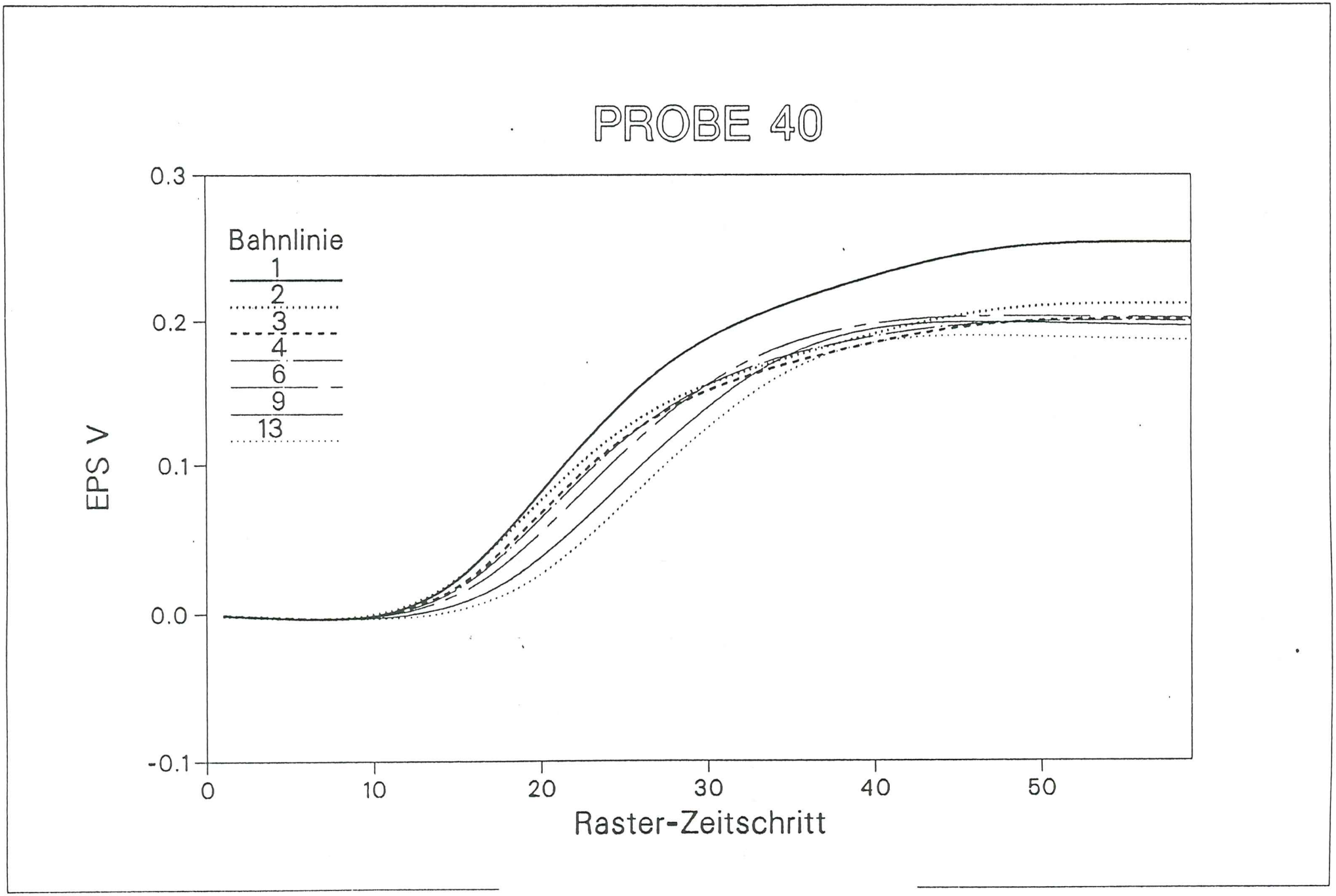

Figure 4.1.4b Experimental effective strain.

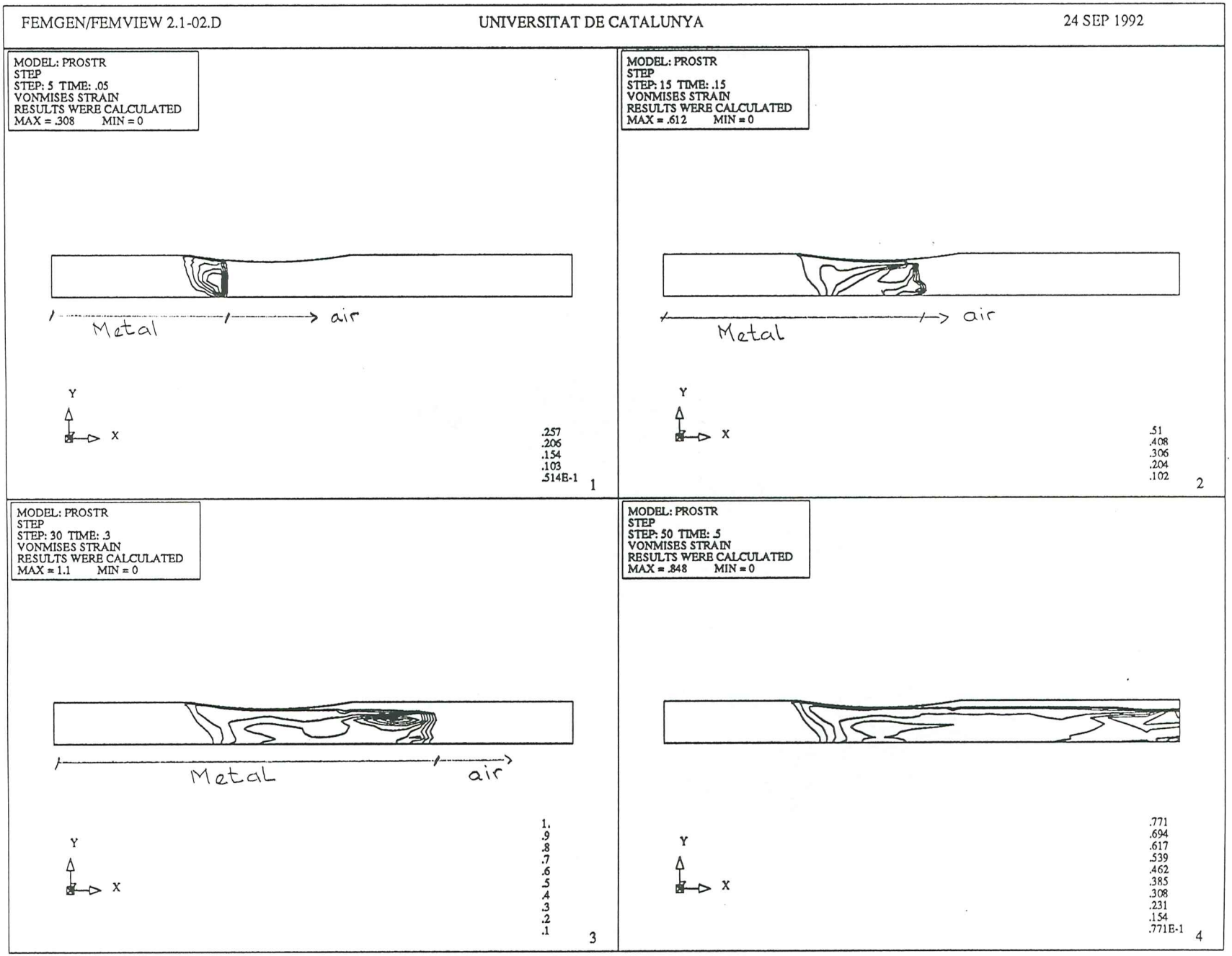

Figure 4.1.4c Numerical Von Mises strain contours (time evolution).

PROBE 40

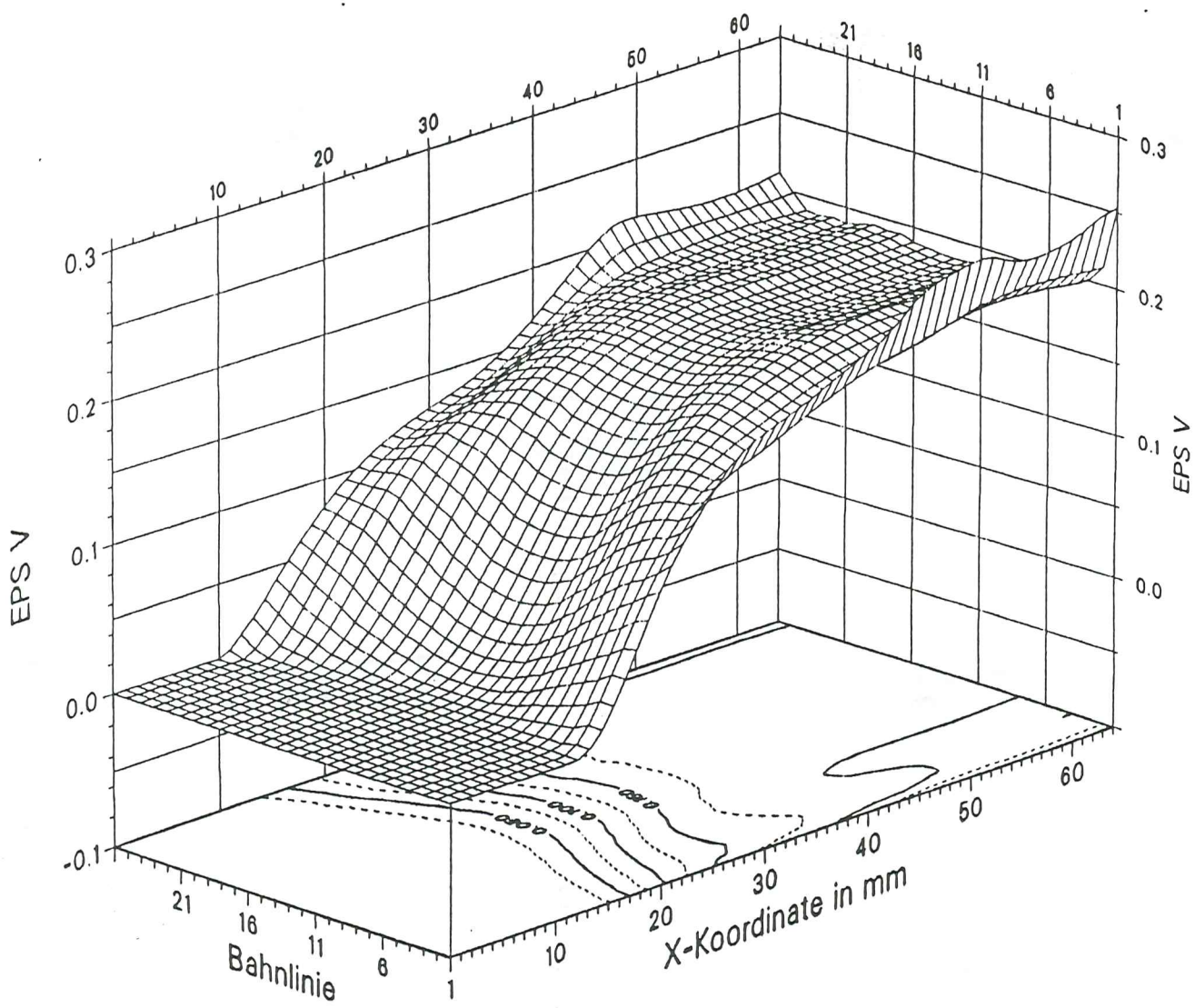

Figure 4.1.4d Experimental effective strain contours.

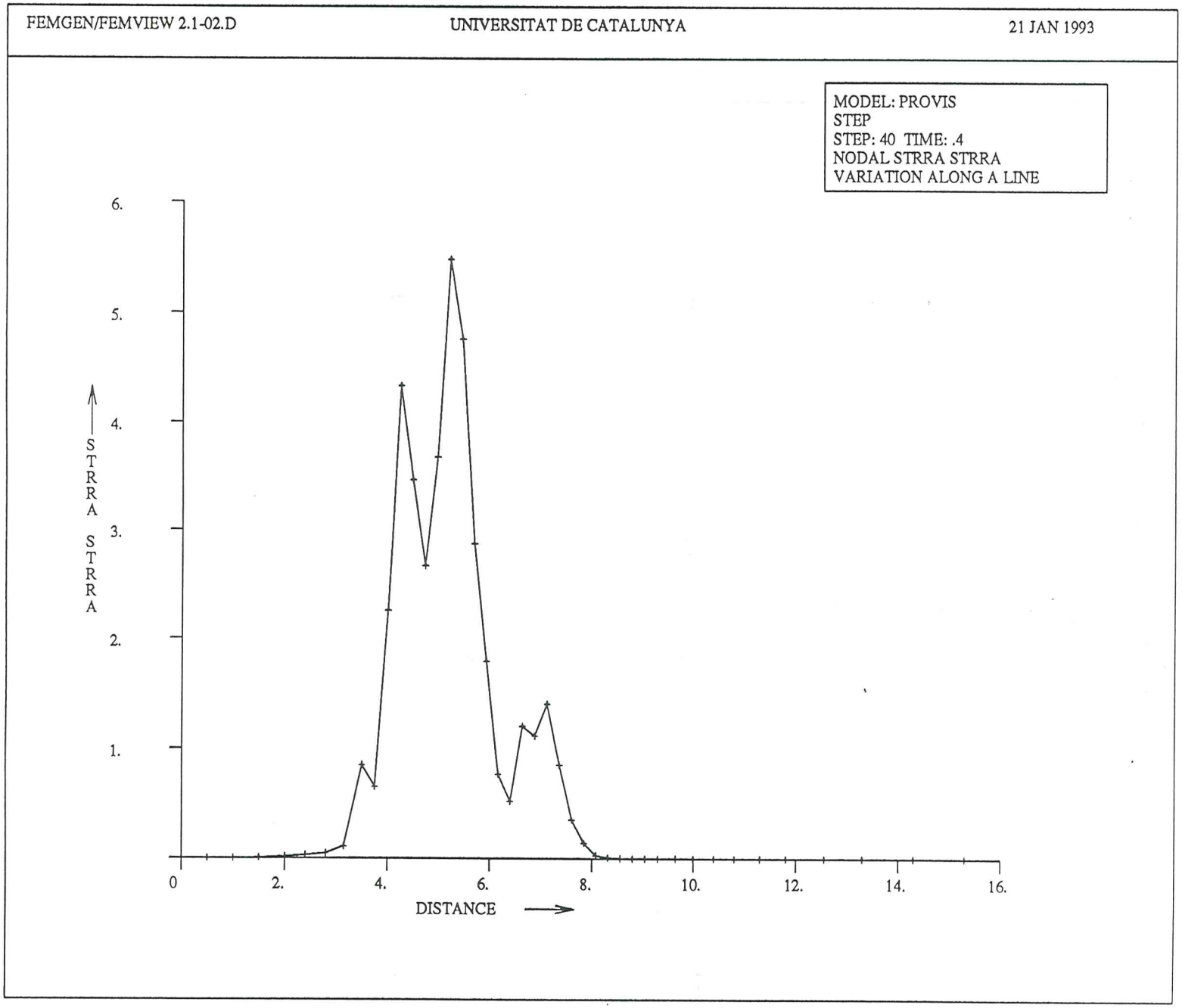

Figure 4.1.5a Numerical Von Mises strain rate (1/seg) (Variation along section A-A').

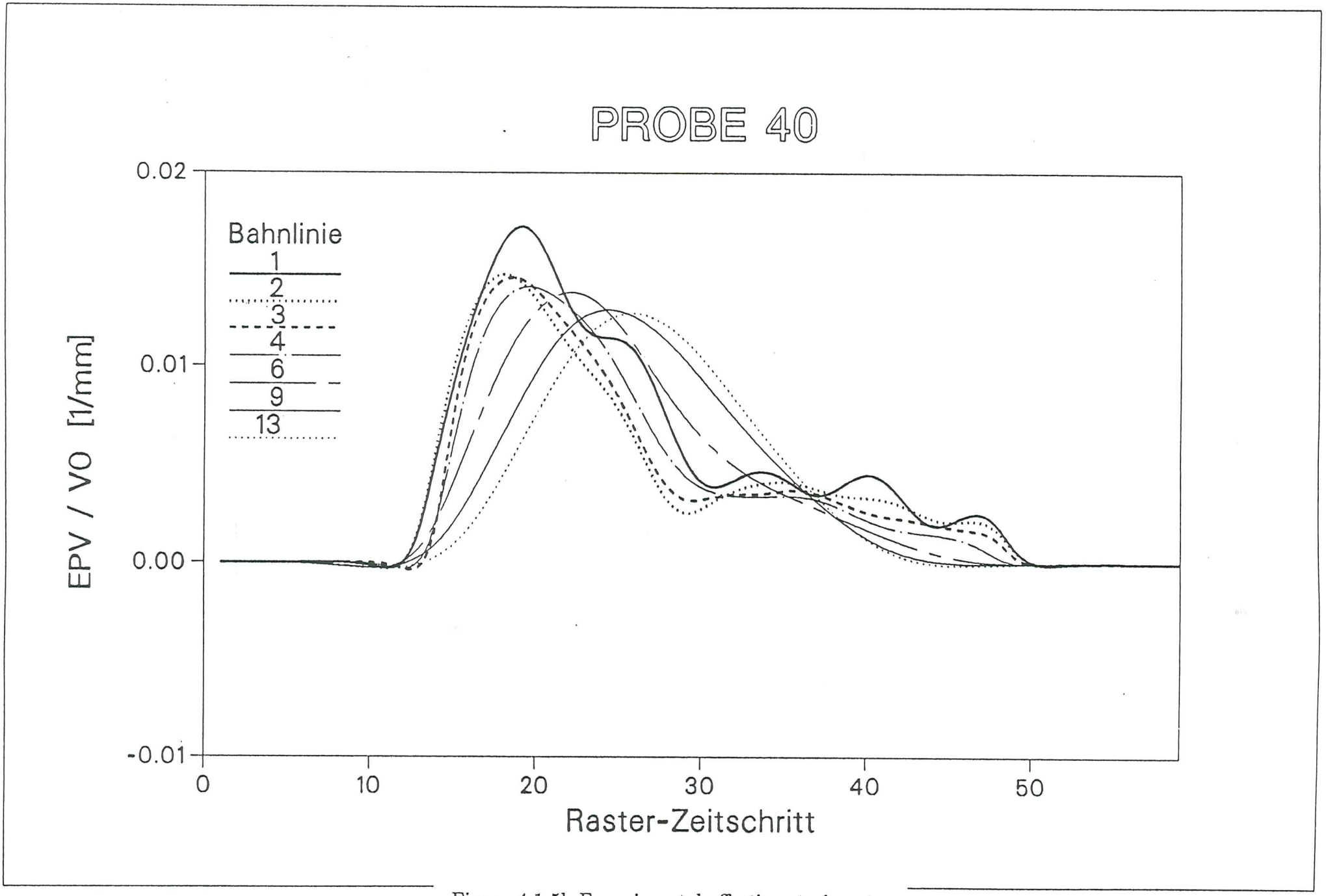

Figure 4.1.5b Experimental effective strain rate.

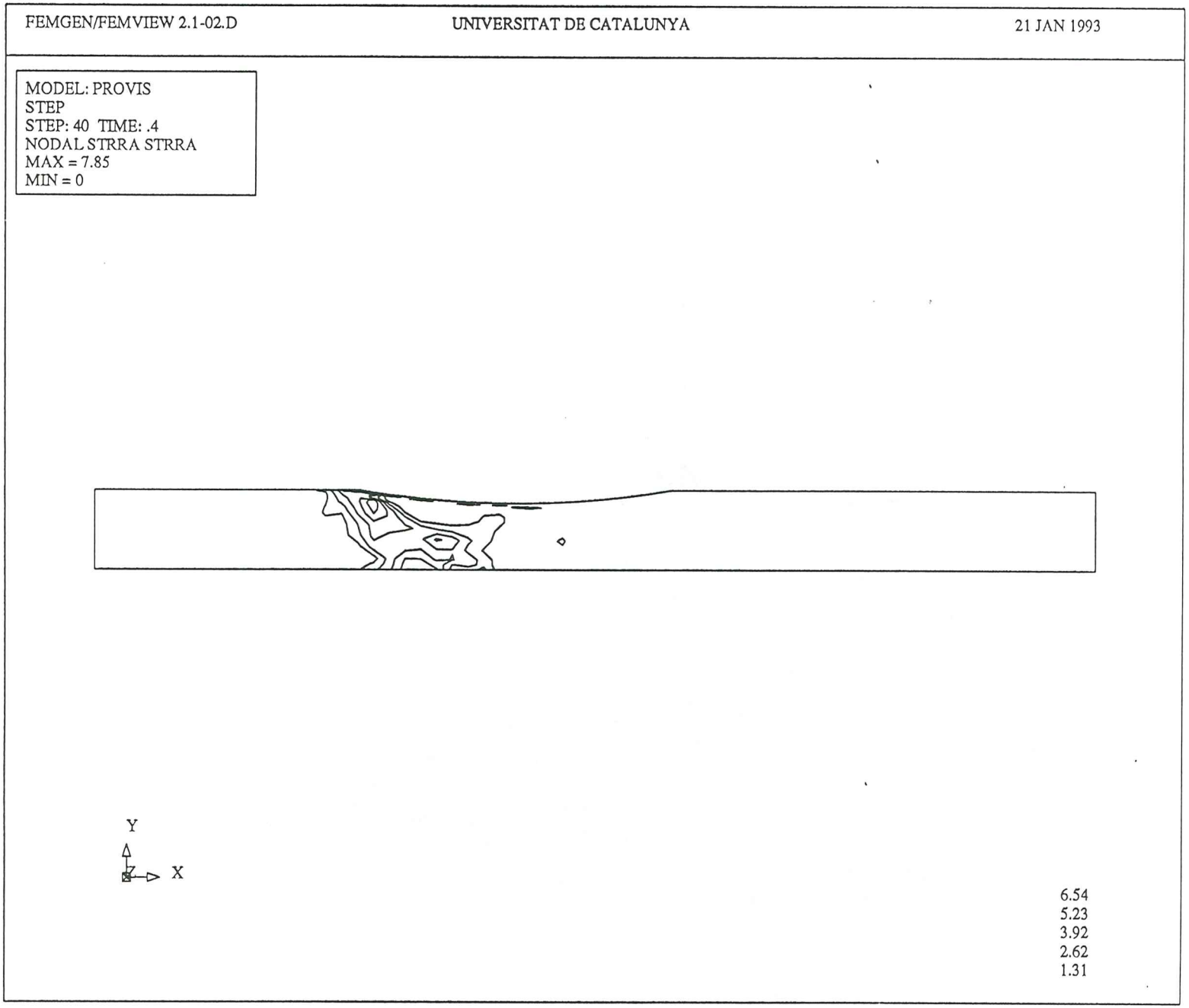

Figure 4.1.5c Numerical Von Mises strain rate contours.

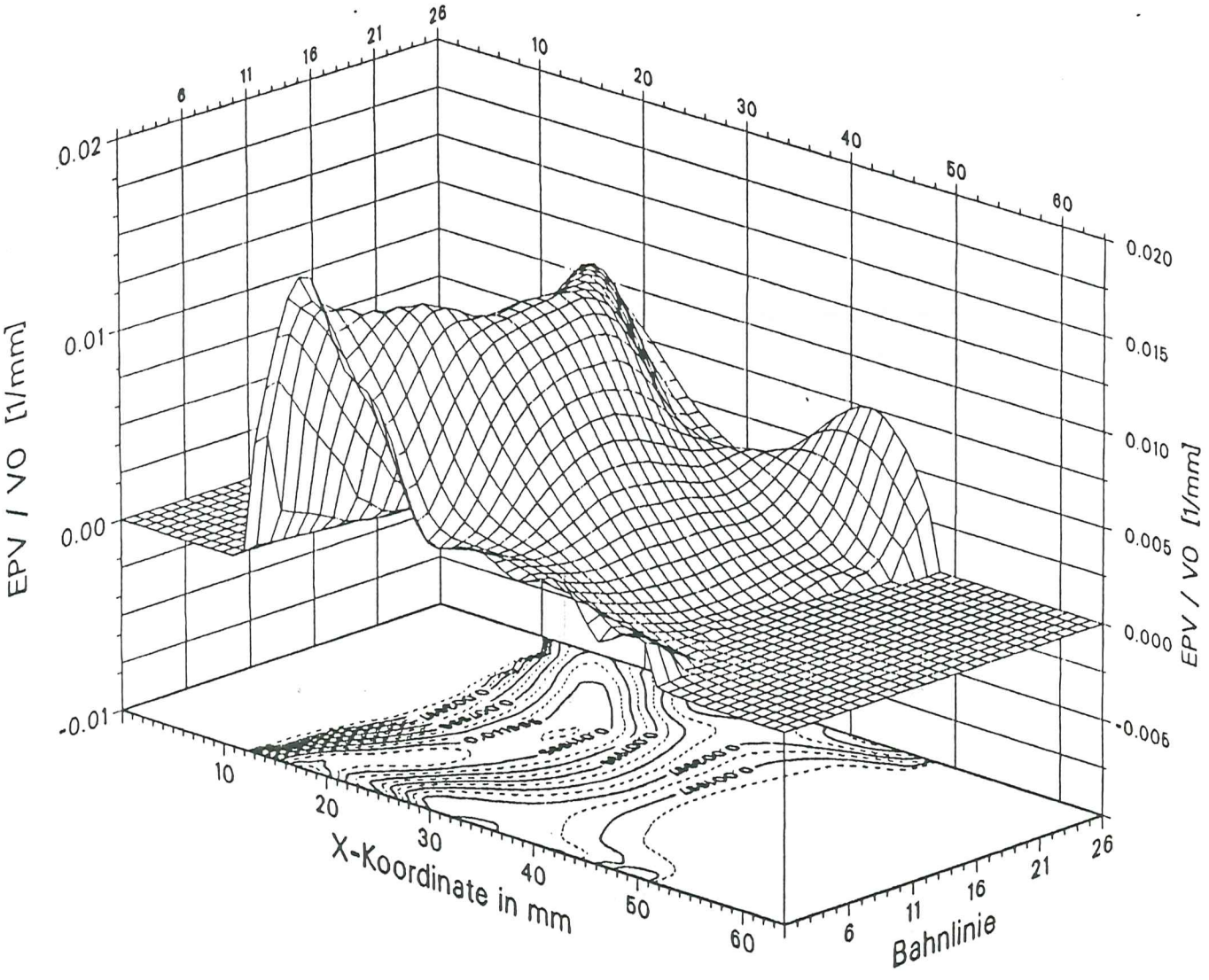

Figure 4.1.5d Experimental effective strain rate contours.

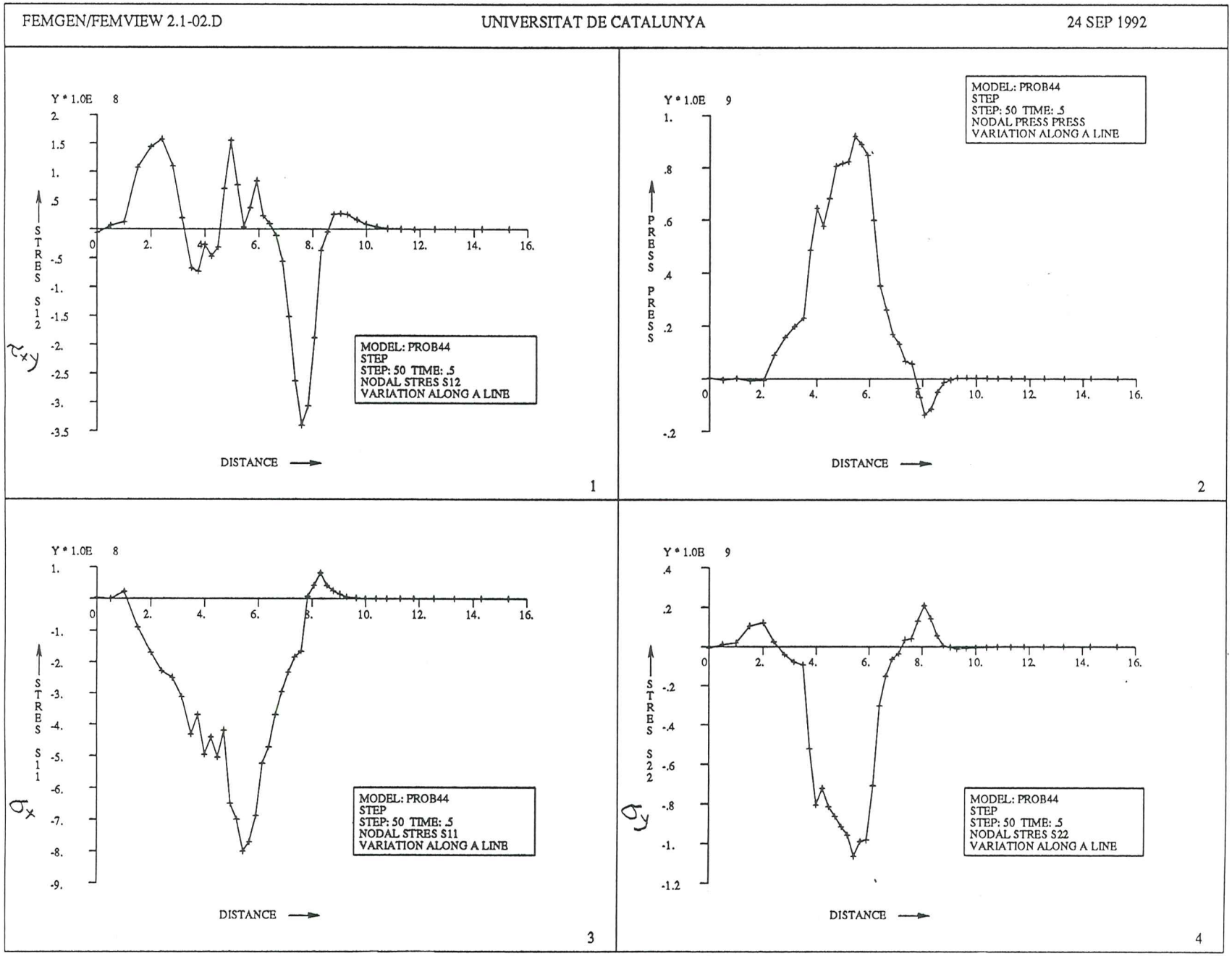

Figure 4.1.6a Numerical stresses (Variation along section A-A').

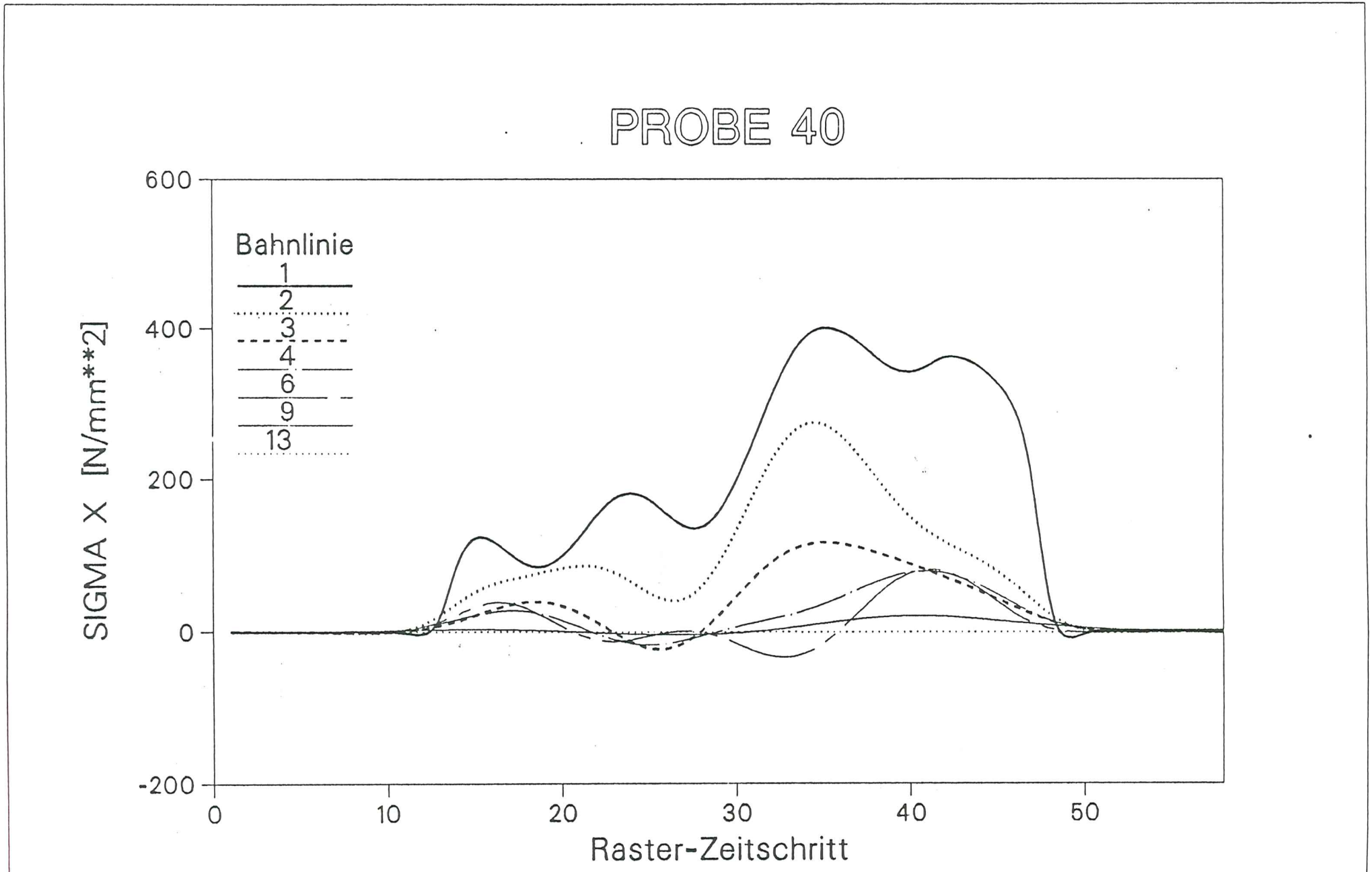

Figure 4.1.6b Experimental horizontal stress.

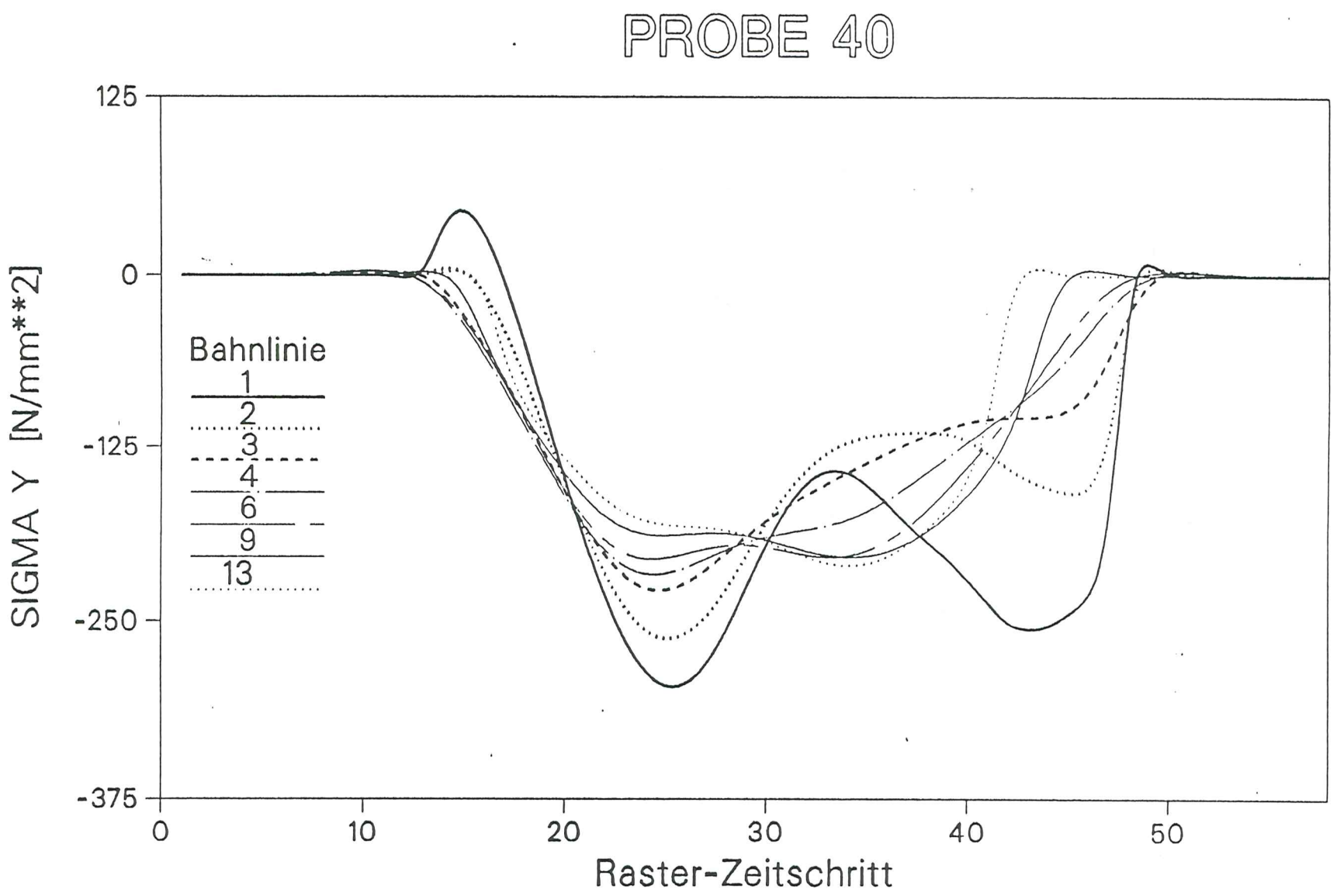

Figure 4.1.6c Experimental vertical stress.

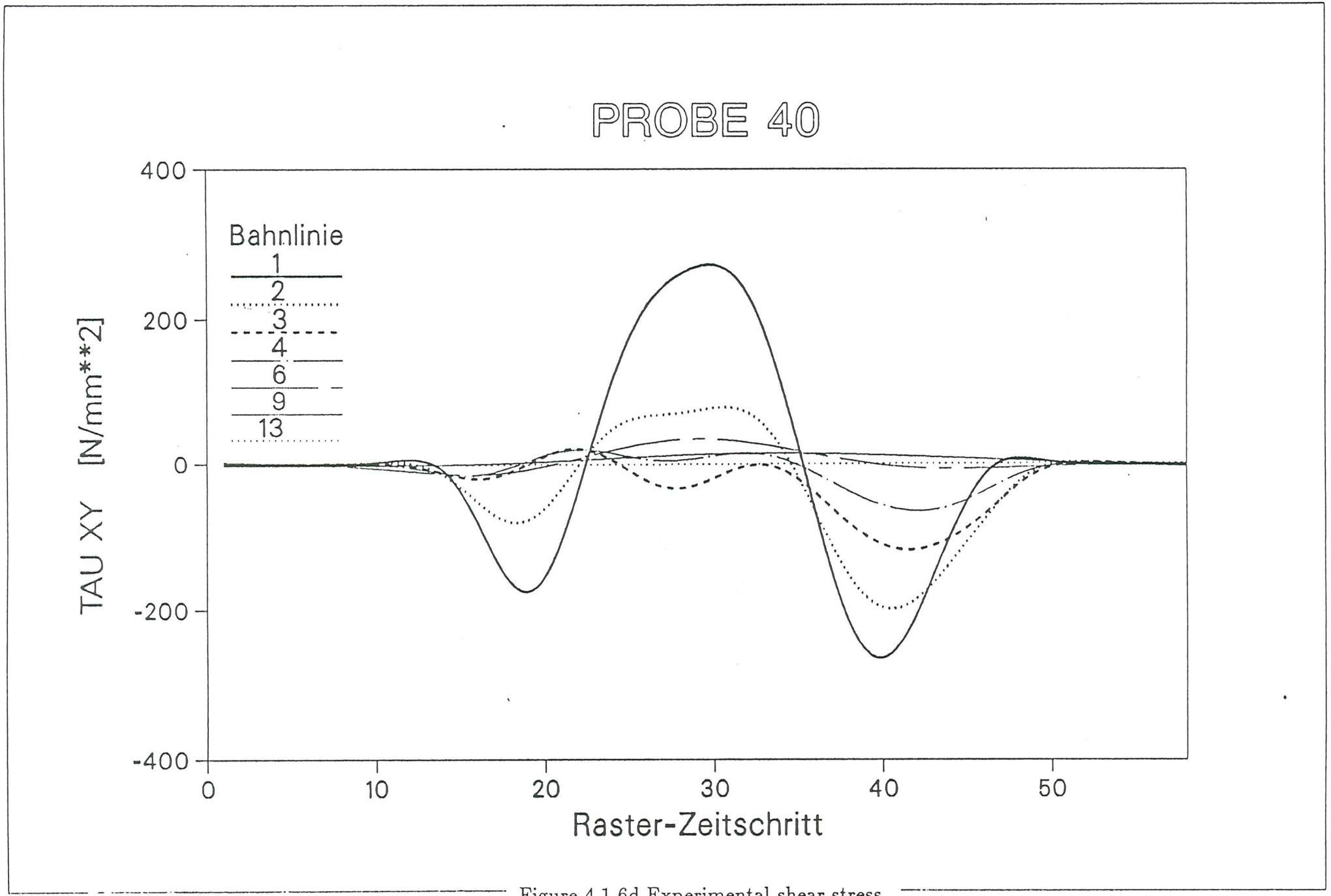

Figure 4.1.6d Experimental shear stress.

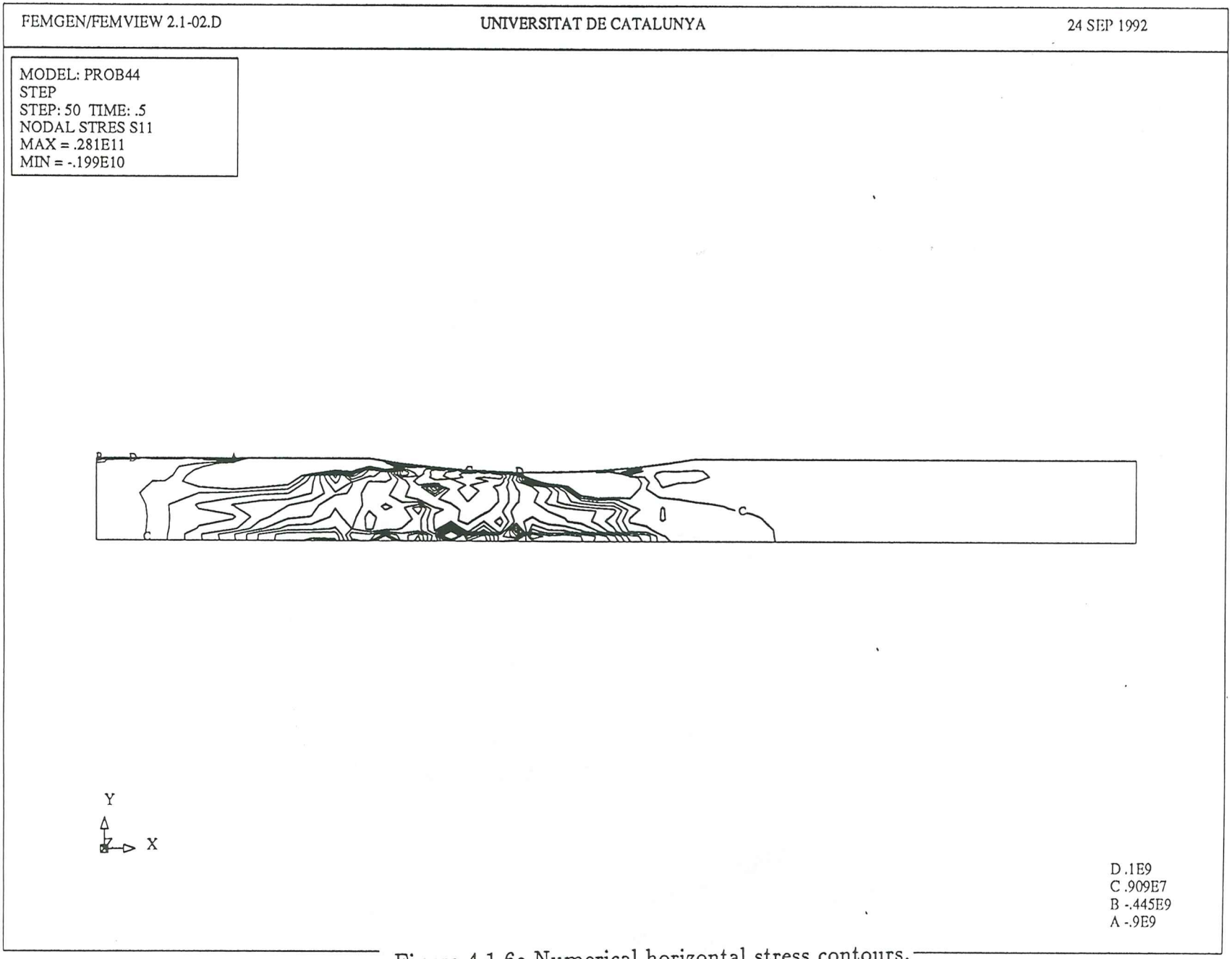

Figure 4.1.6e Numerical horizontal stress contours.

PROBE 40

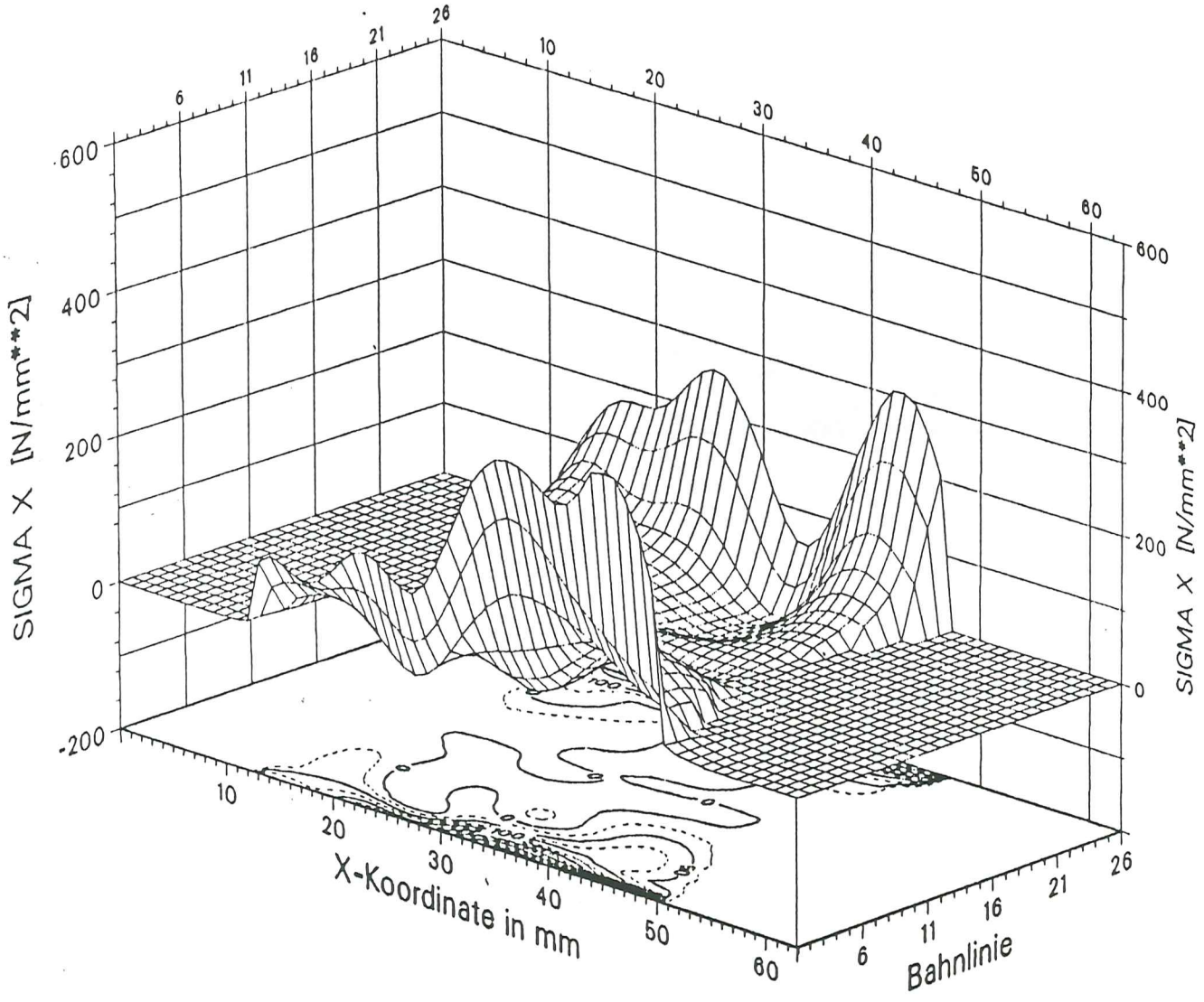

Figure 4.1.6f Experimental horizontal stress contours.

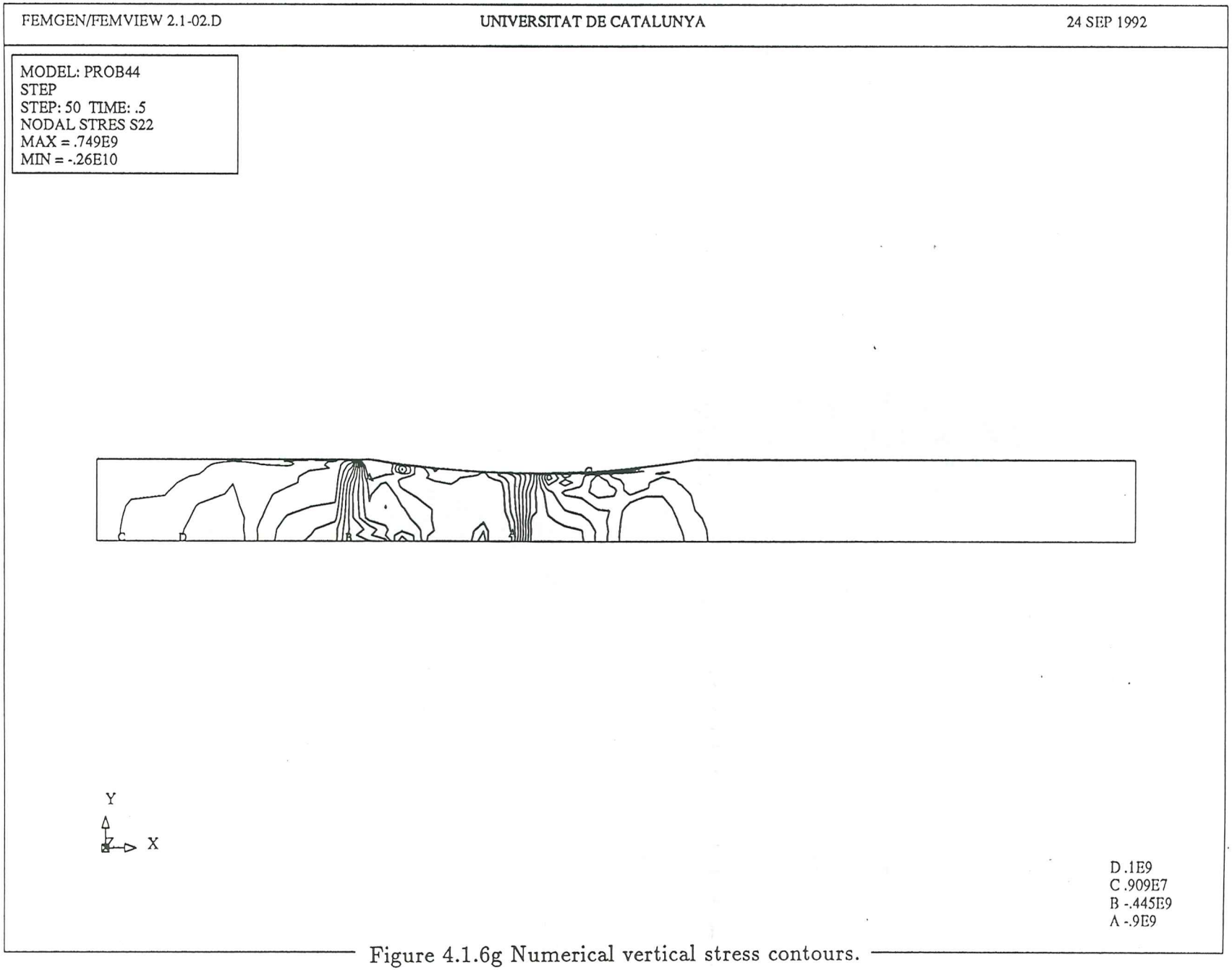

Figure 4.1.6g Numerical vertical stress contours.

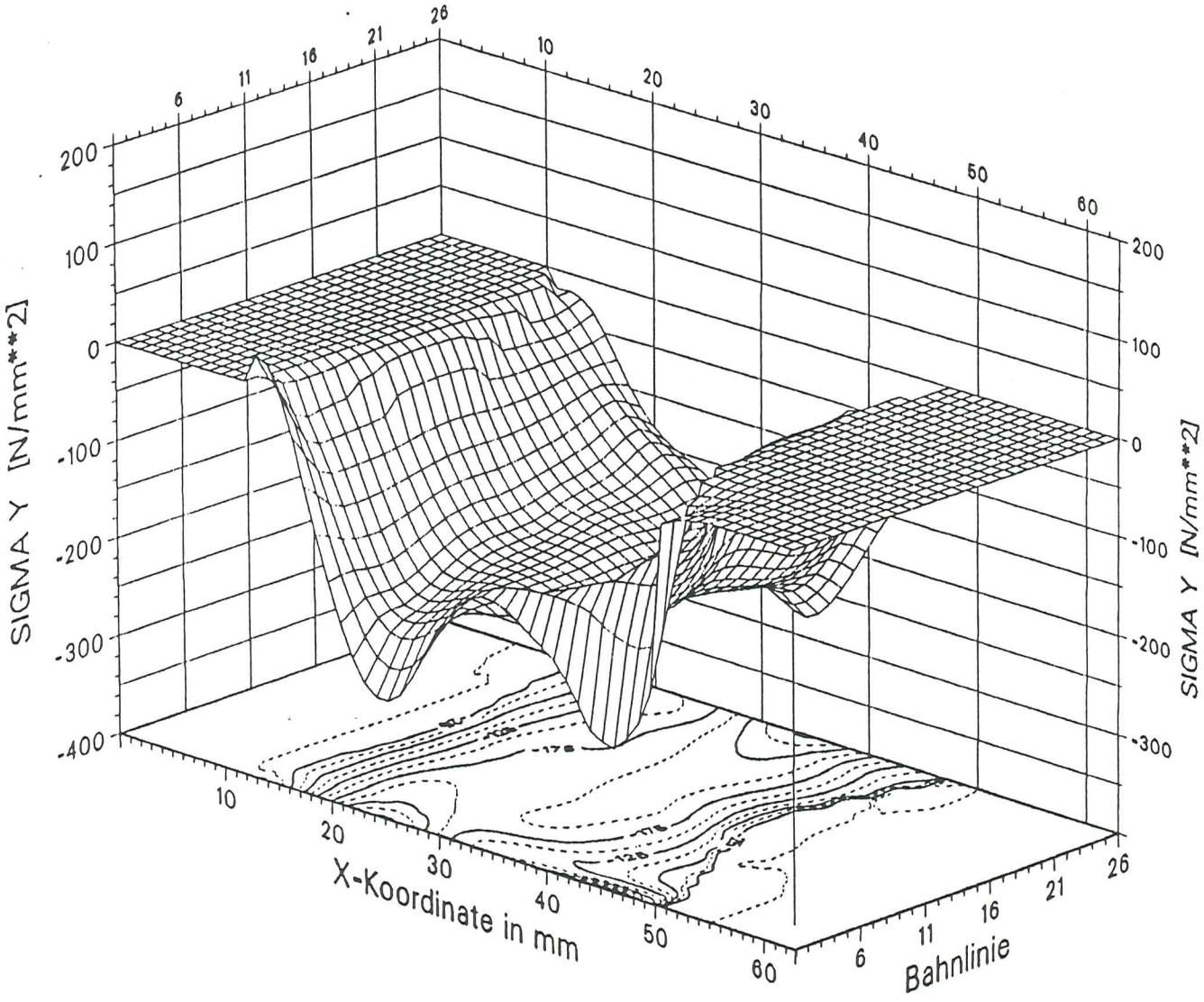

Figure 4.1.6h Experimental vertical stress contours.

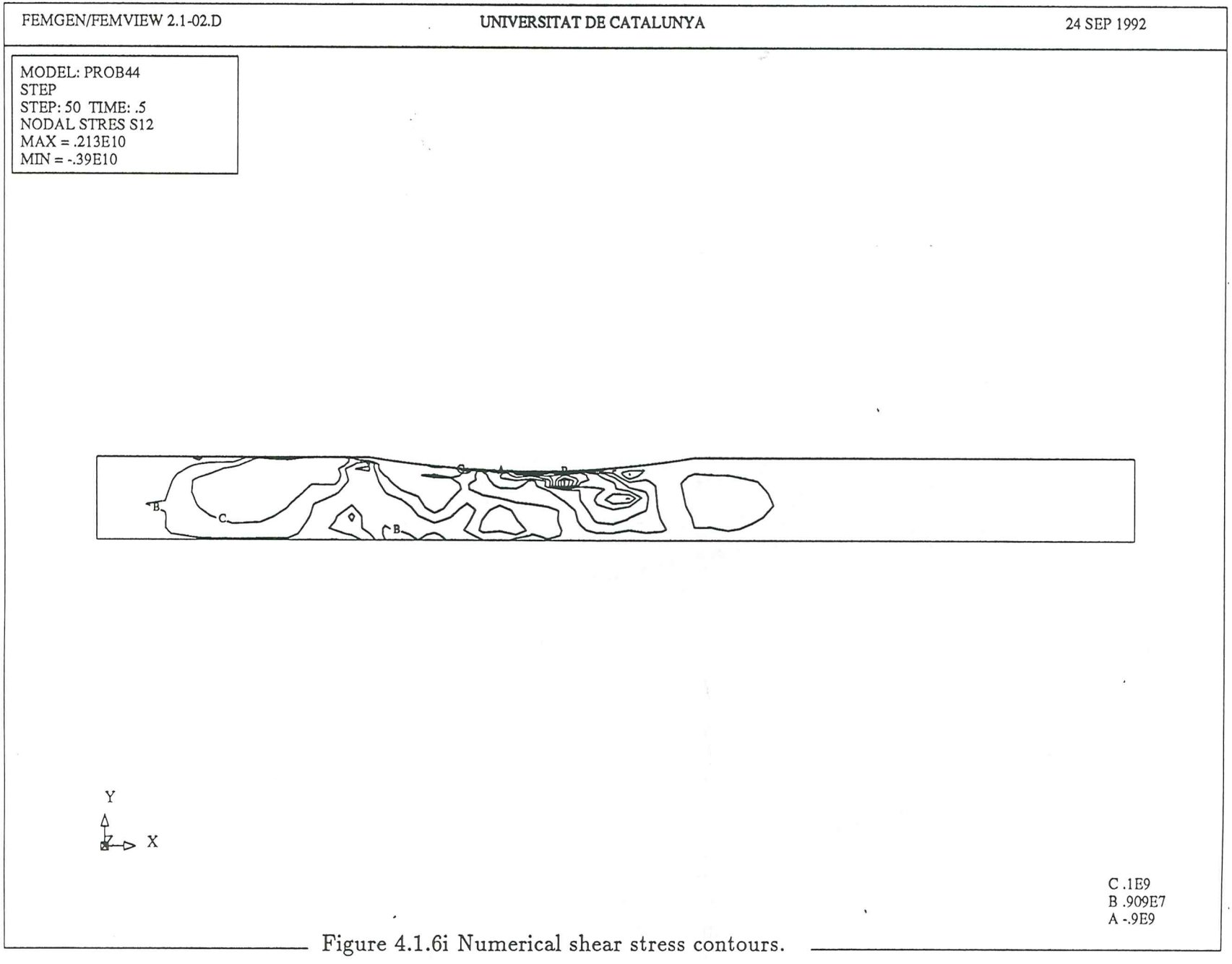

Figure 4.1.6i Numerical shear stress contours.

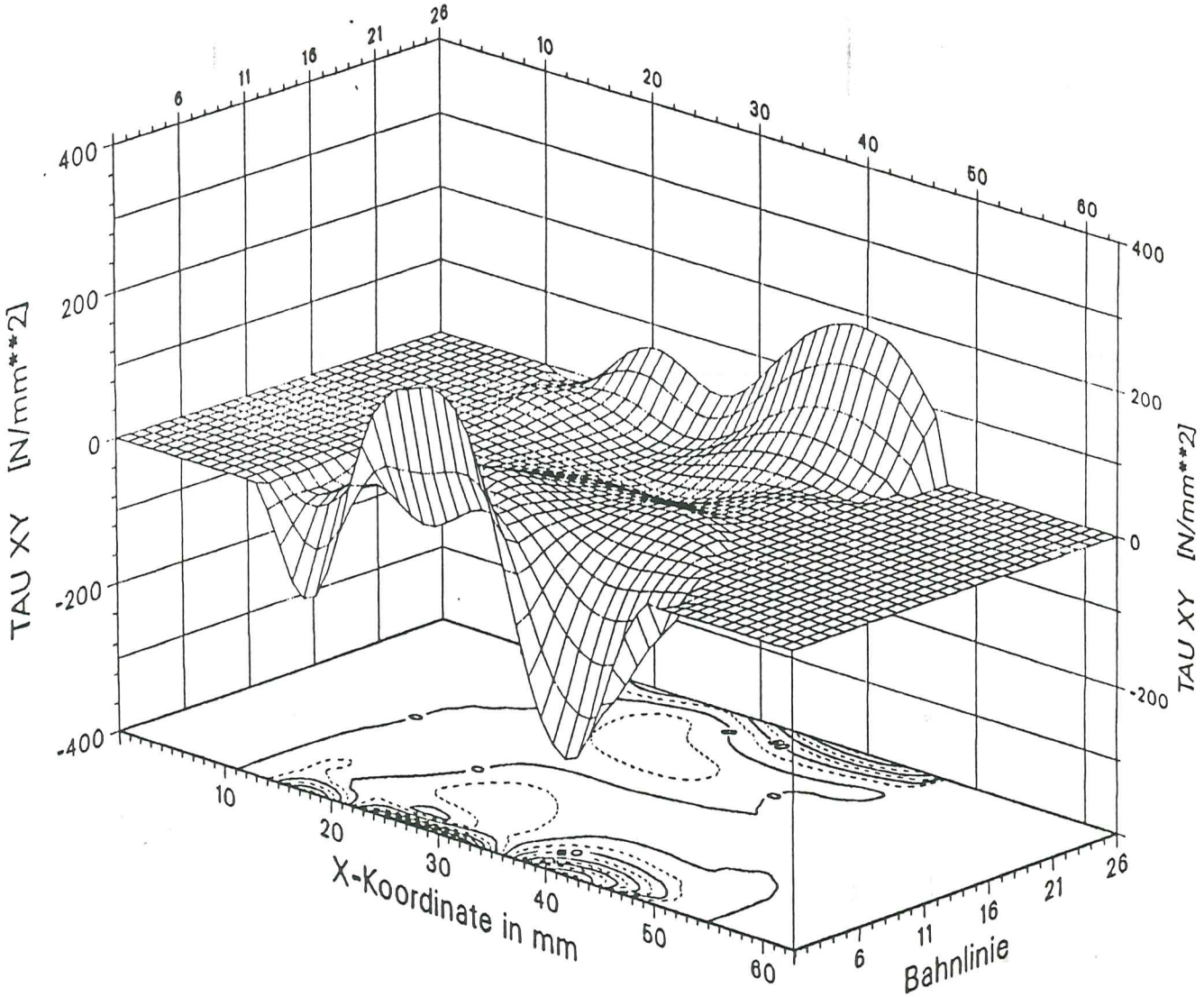

Figure 4.1.6j Experimental shear stress contours.

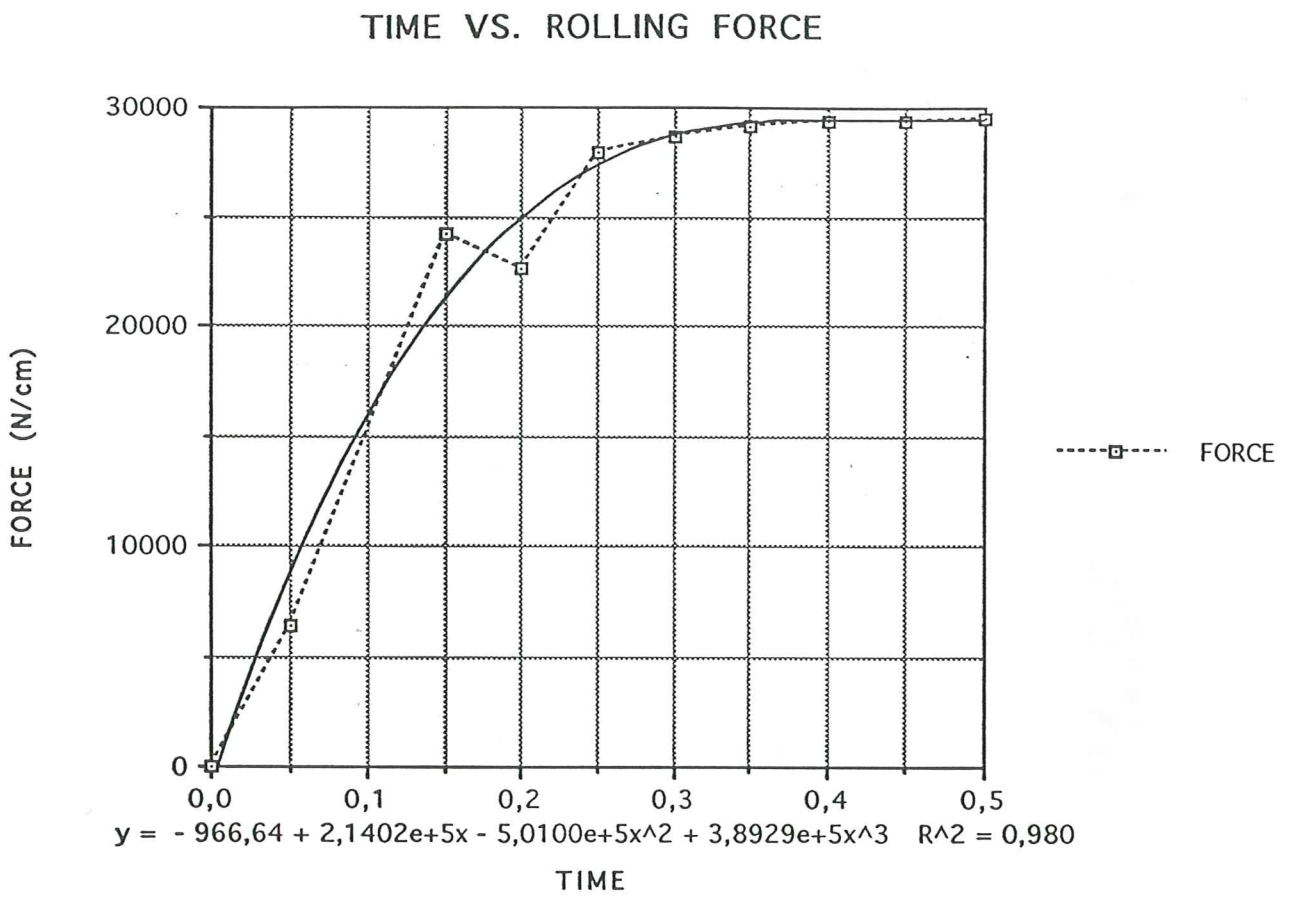

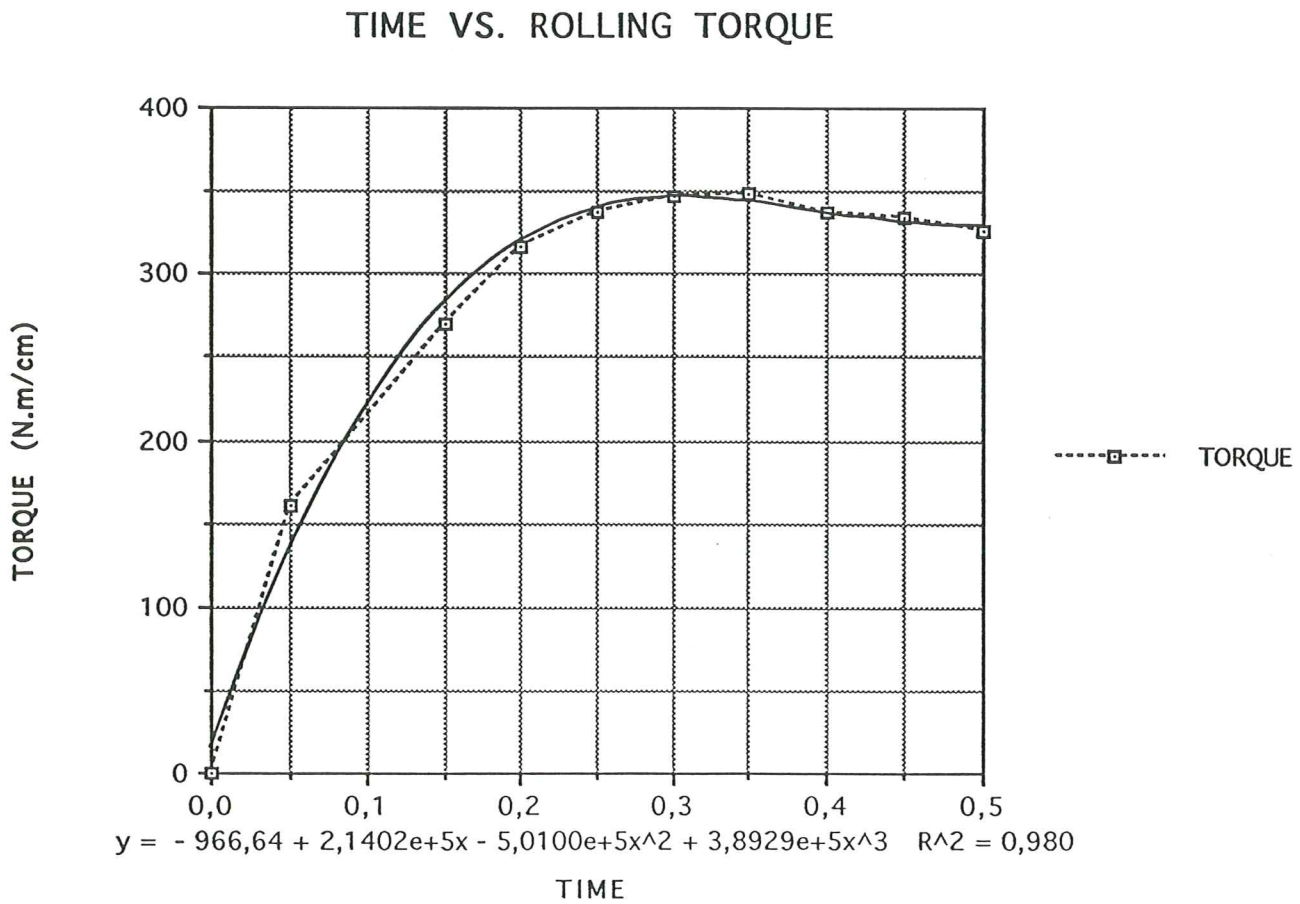

Figure 4.1.7 Force and torque time evolution.

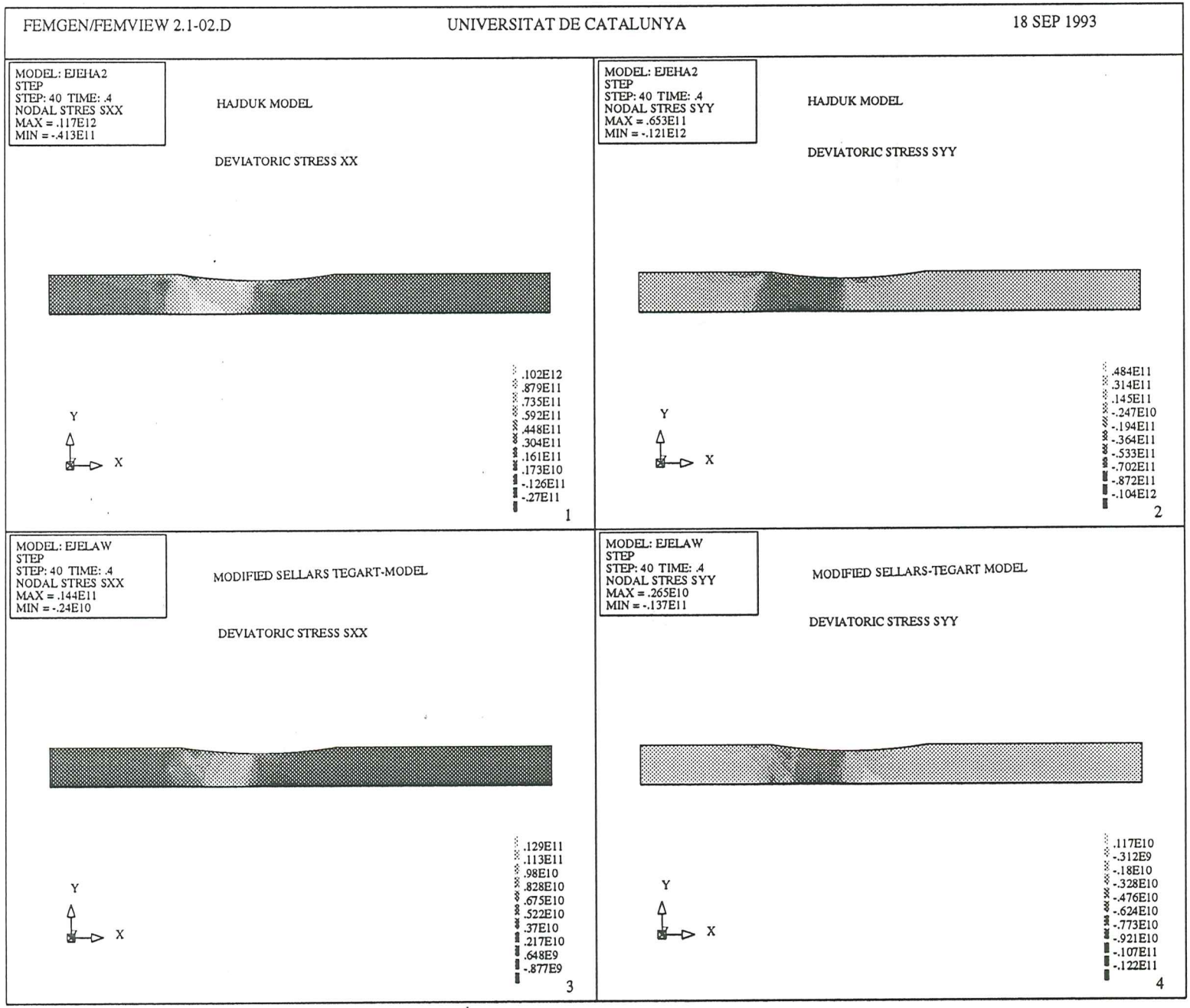

Figure 4.2.1a Stress fields $[dy/cm^2]$ for different constitutive laws.

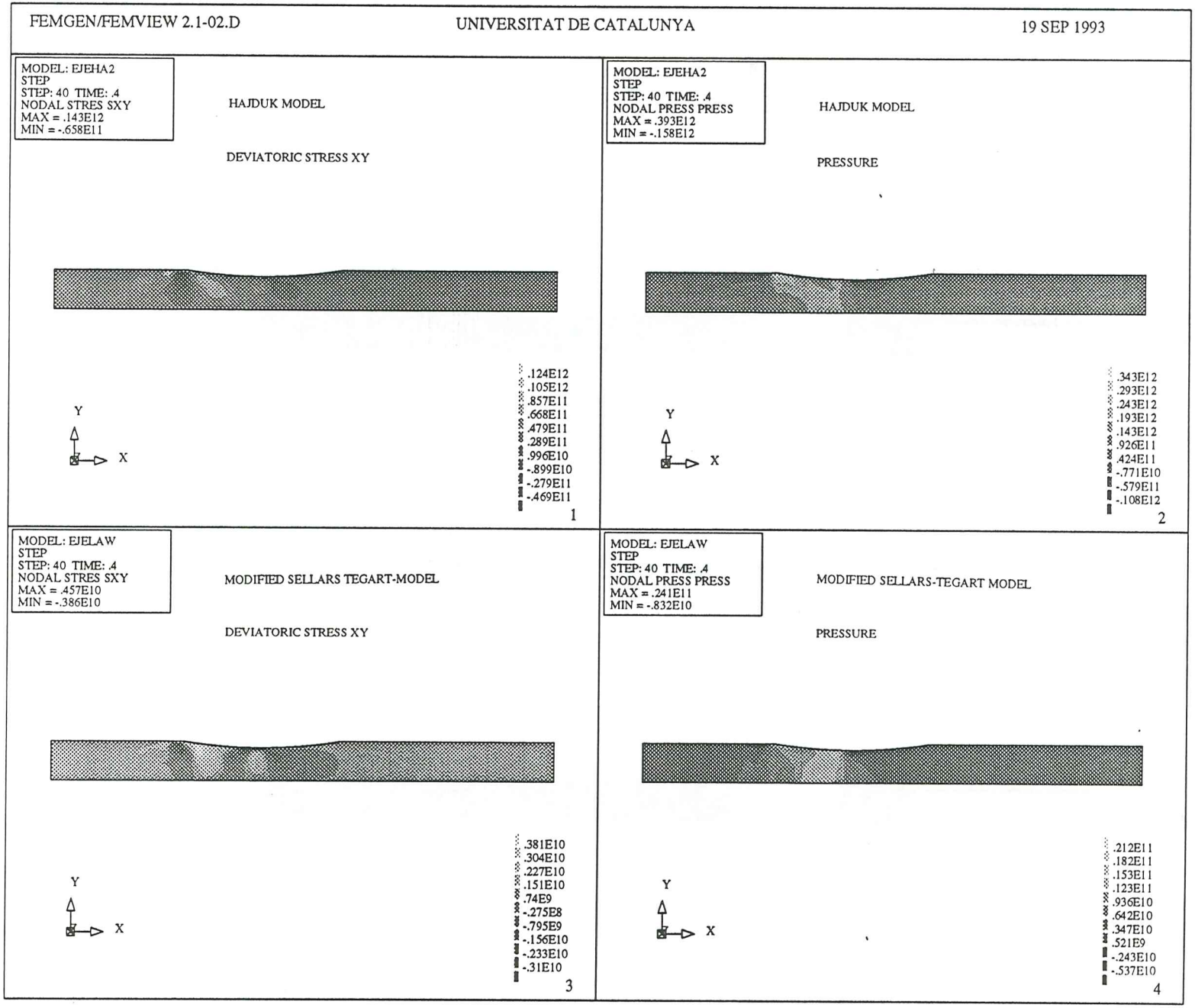

Figure 4.2.1b Stress and pressure fields $[dy/cm^2]$ for different constitutive laws.

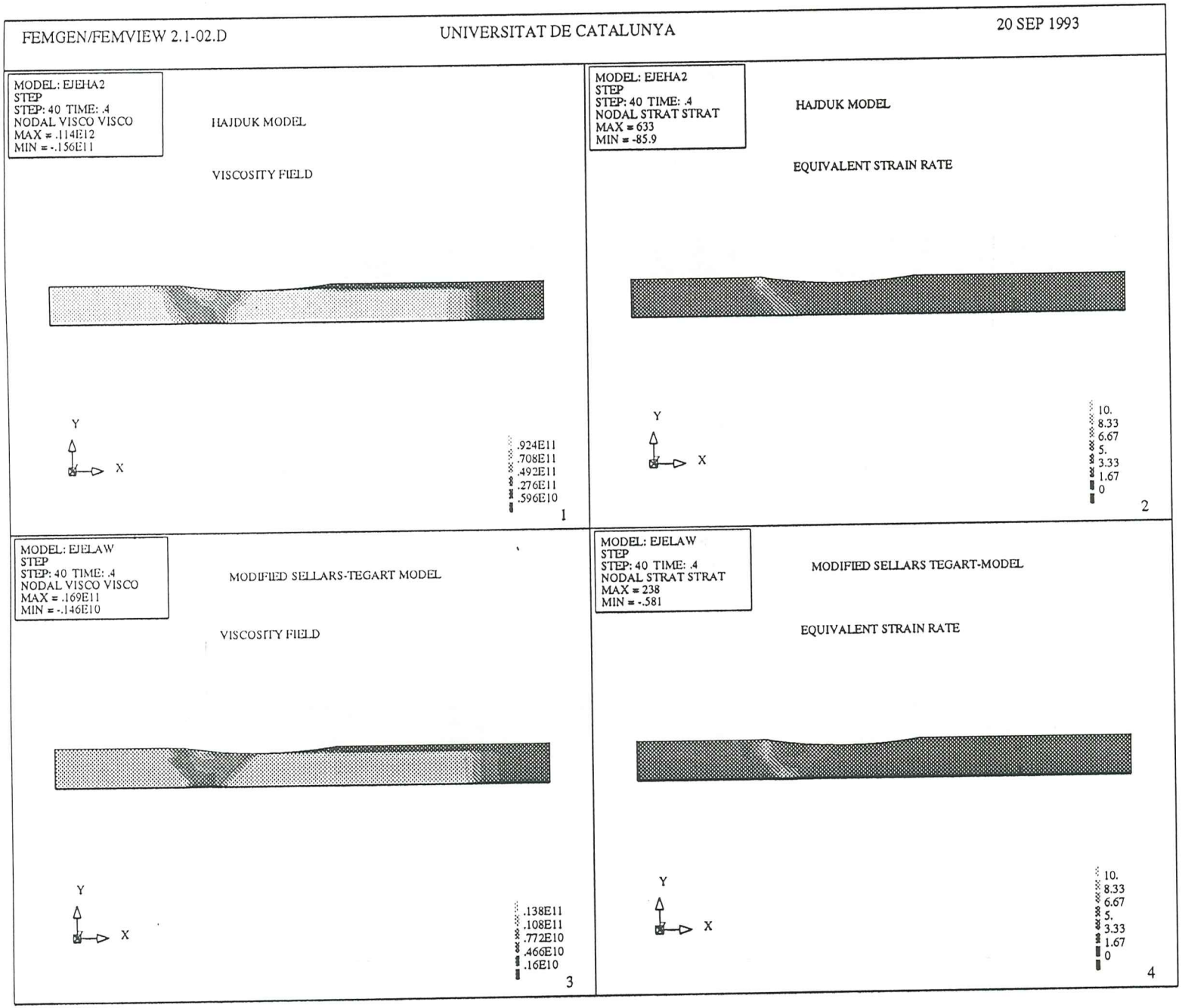

Figure 4.2.1c Viscosity $[dy/cm^2]$ and equivalent strain rate $[s^{-1}]$.

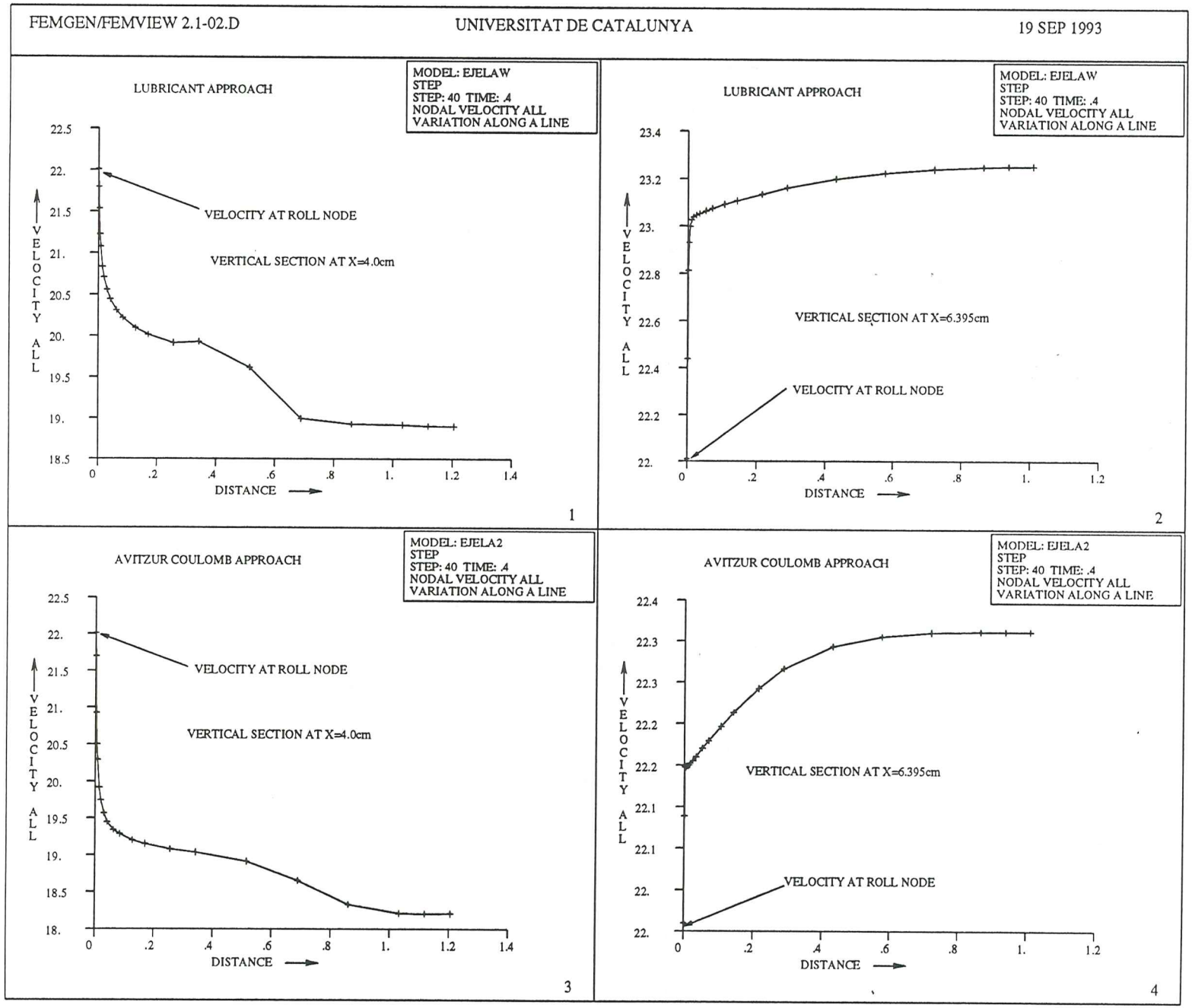

Figure 4.2.2a Velocity profiles for different friction approachs $[cm/s]$. $\xi = 0.1$, $m = 1.0$ and $\mu_0 = 10^7$.

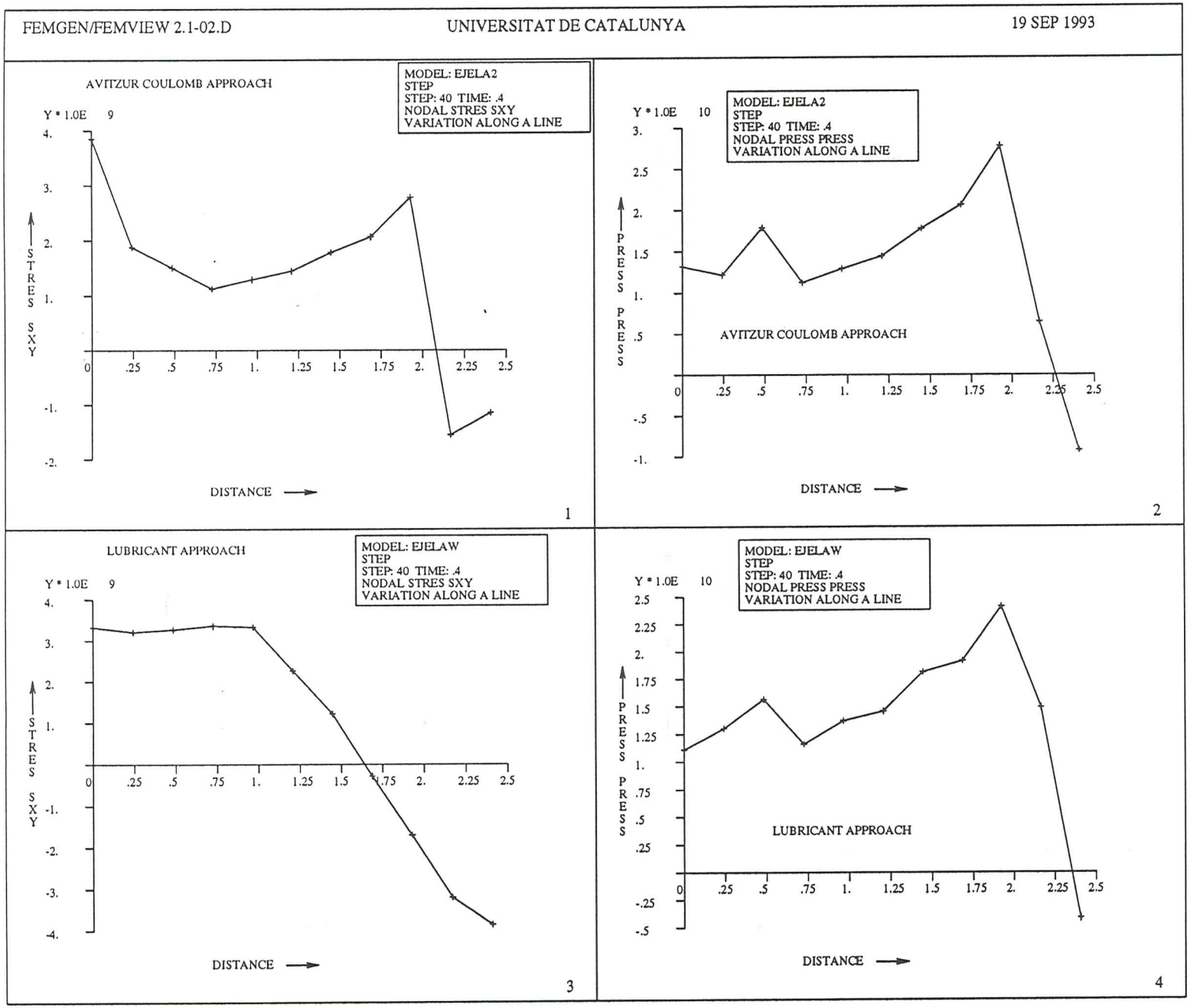

Figure 4.2.2b Shear stress and pressure $[dy/cm^2]$ distribution at roll surface. $\xi = 0.1$, $m = 1.0$ and $\mu_0 = 10^7$.

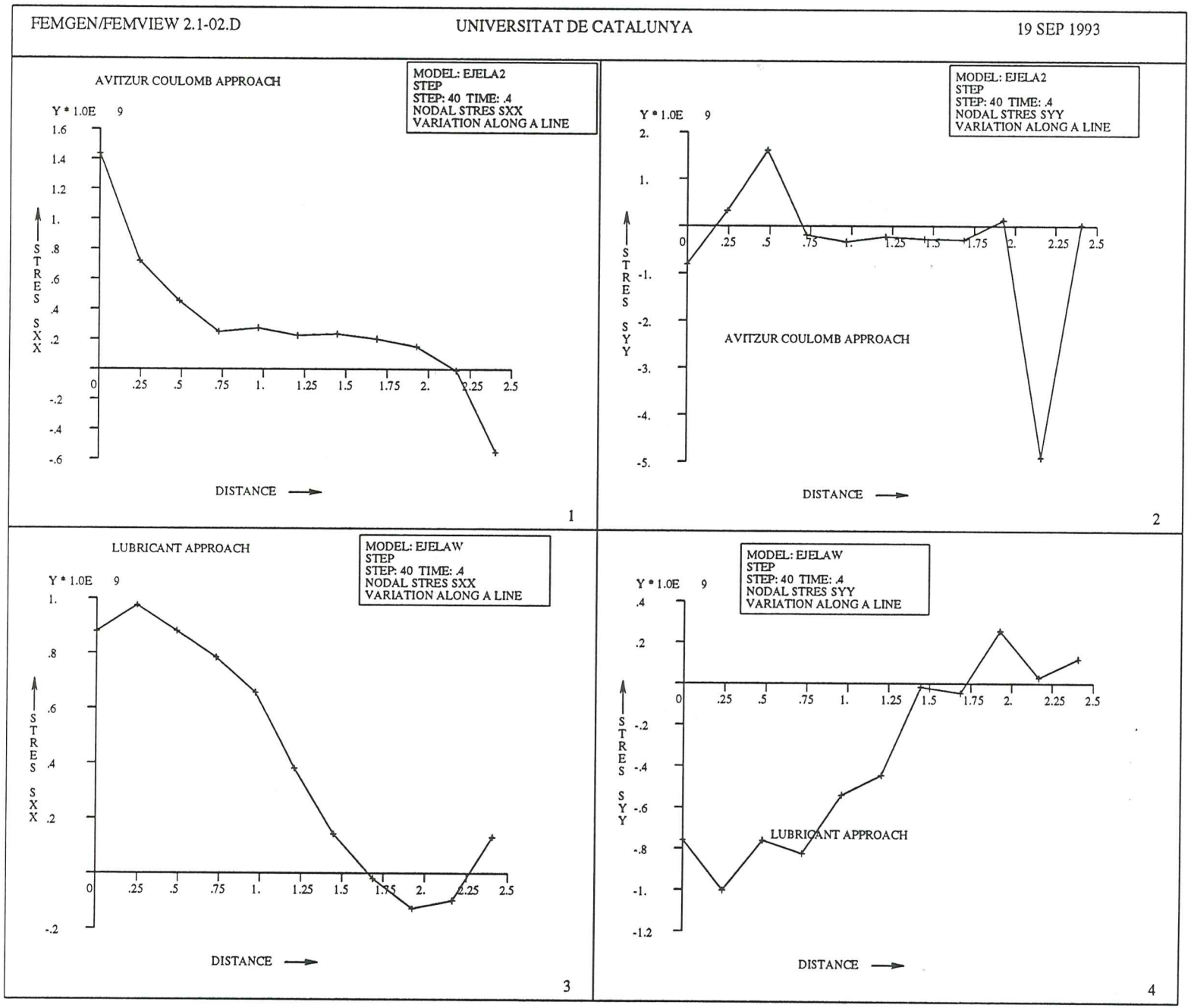

Figure 4.2.2c Stress $[dy/cm^2]$ distribution at roll surface. $\xi = 0.1$, $m = 1.0$ and $\mu_0 = 10^7$.

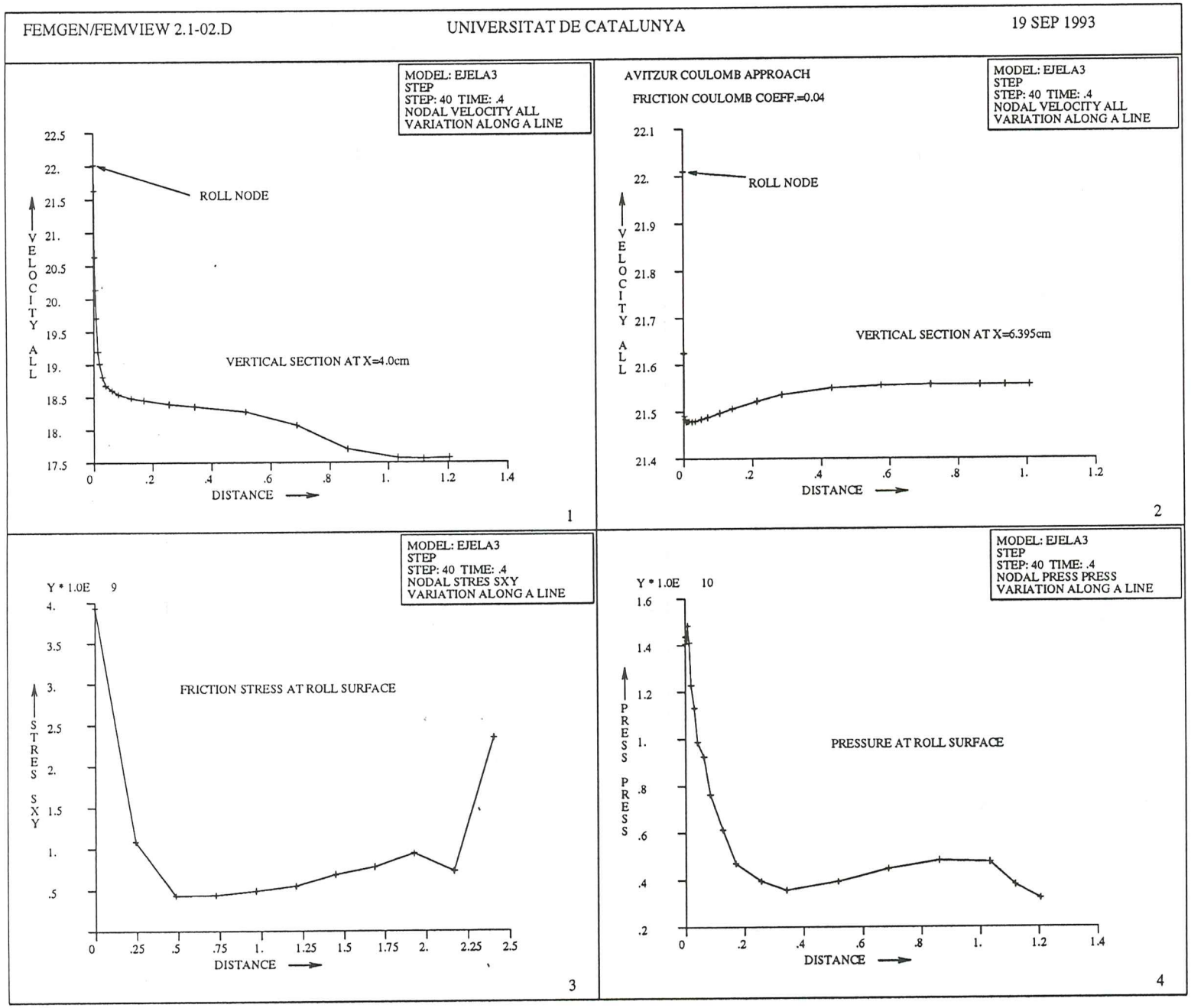

Figure 4.2.2d Velocity profiles $[cm/s]$ and stress distribution $[dy/cm^2]$ at roll surface for $\xi = 0.04$.

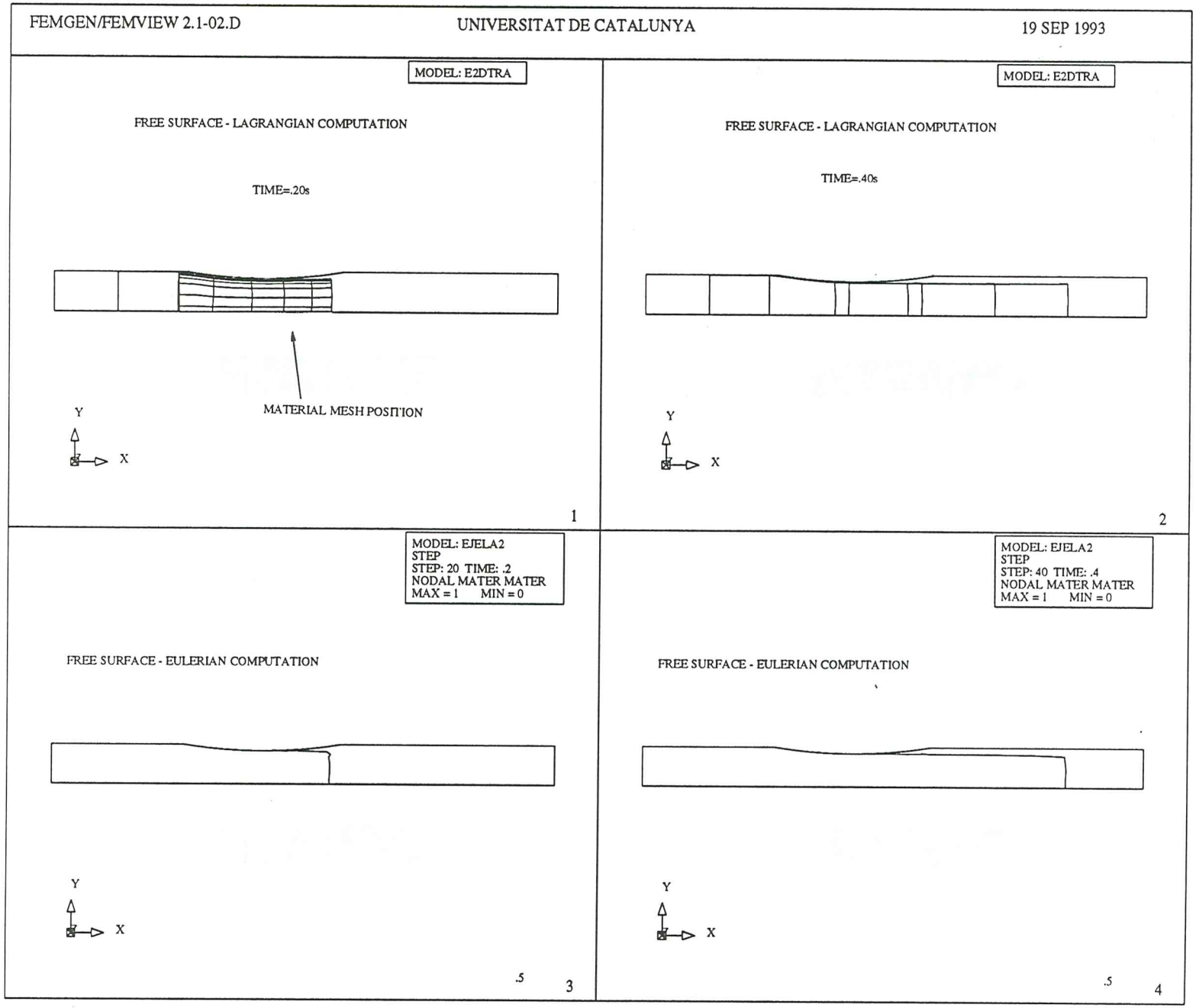

Figure 4.2.3 Free surface time evolution.

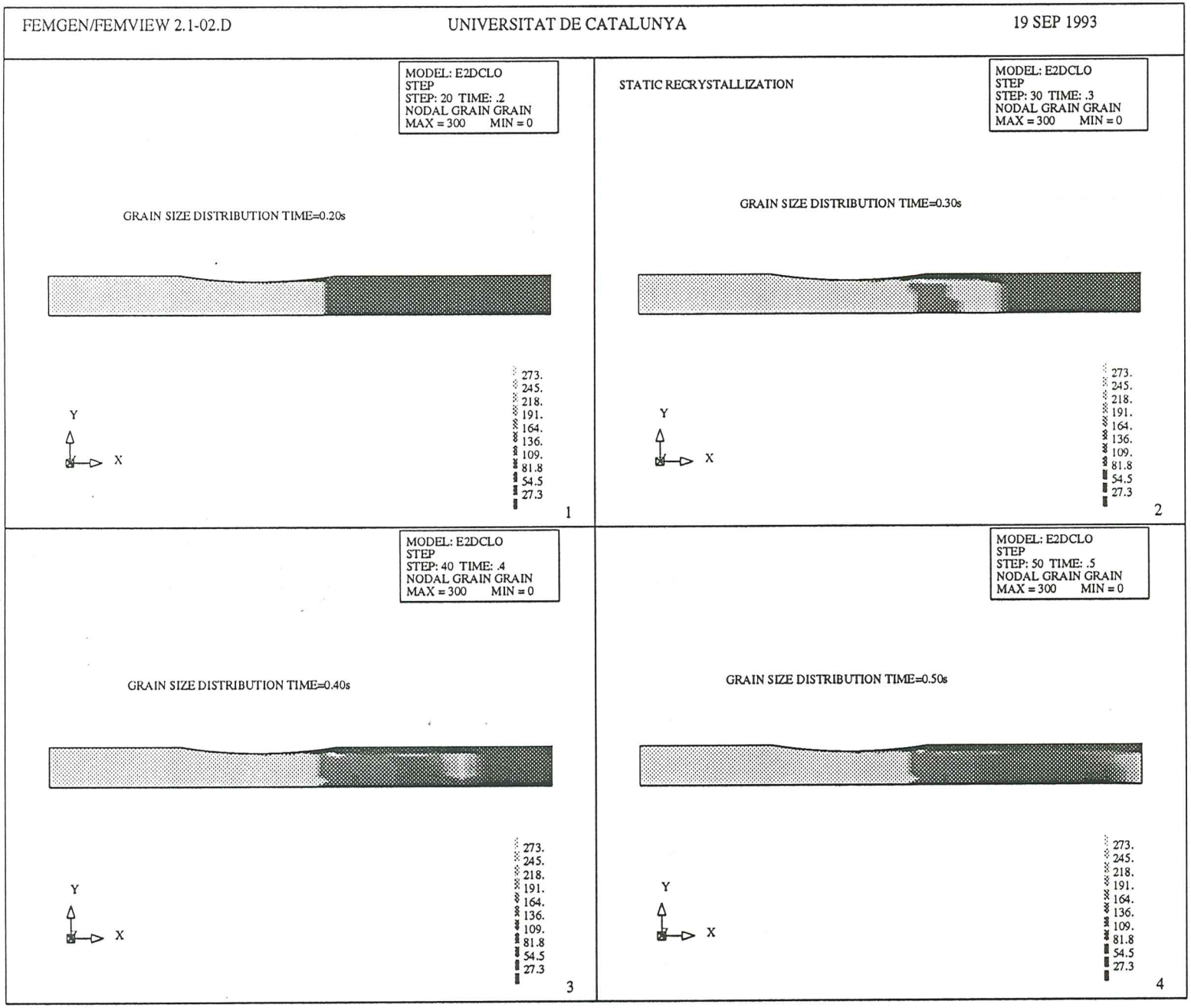

Figure 4.2.4a Grain size $[\mu M]$ time evolution. Initial grain size $300\mu M$ (Note:Fictitious fluid grain size is zero)

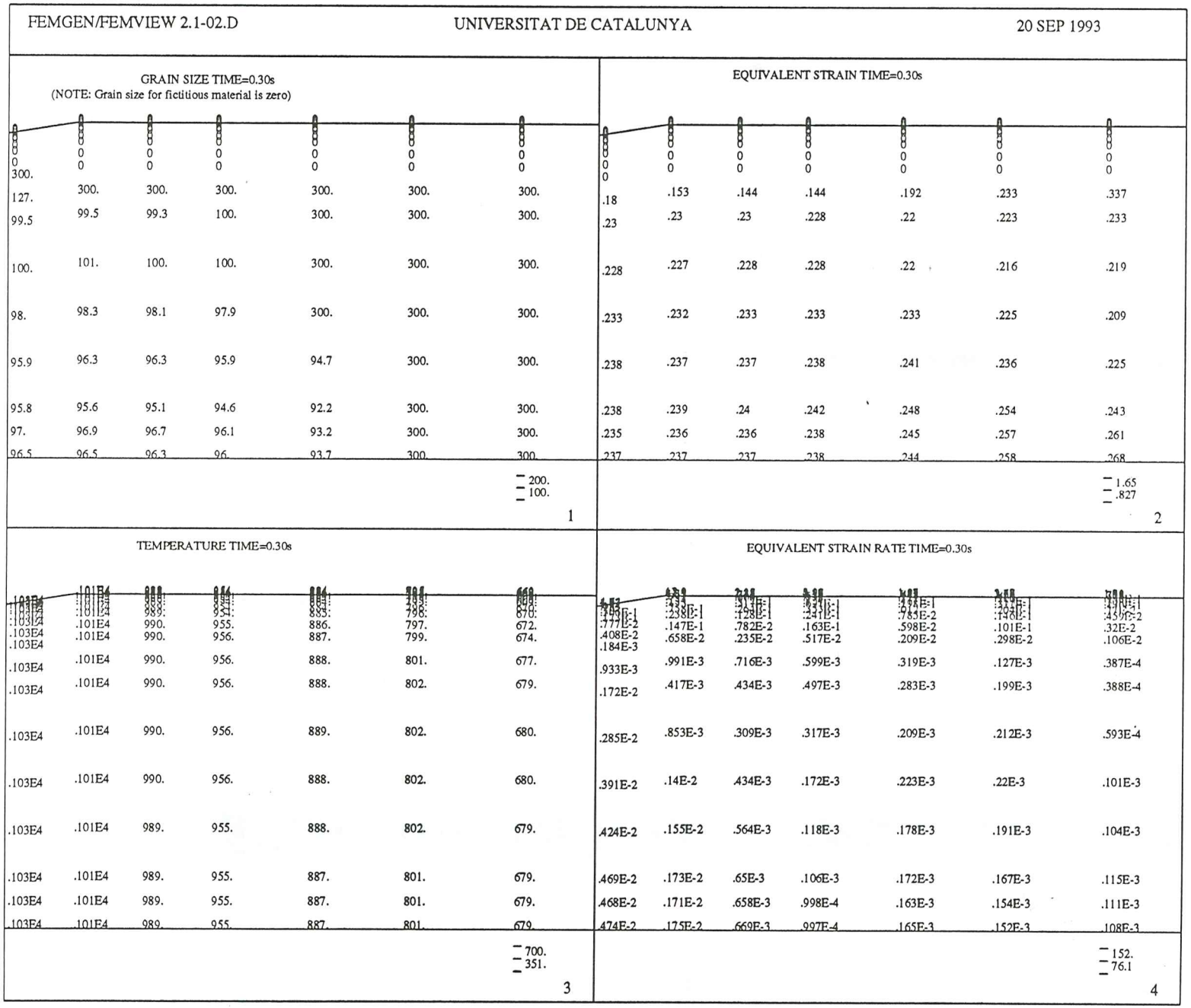

Figure 4.2.4b Numerical values for grain size $[\mu M]$, $\bar{\varepsilon}$, T $[^{o}C]$ and $\dot{\bar{\varepsilon}}[s^{-1}]$ at time=0.30s.

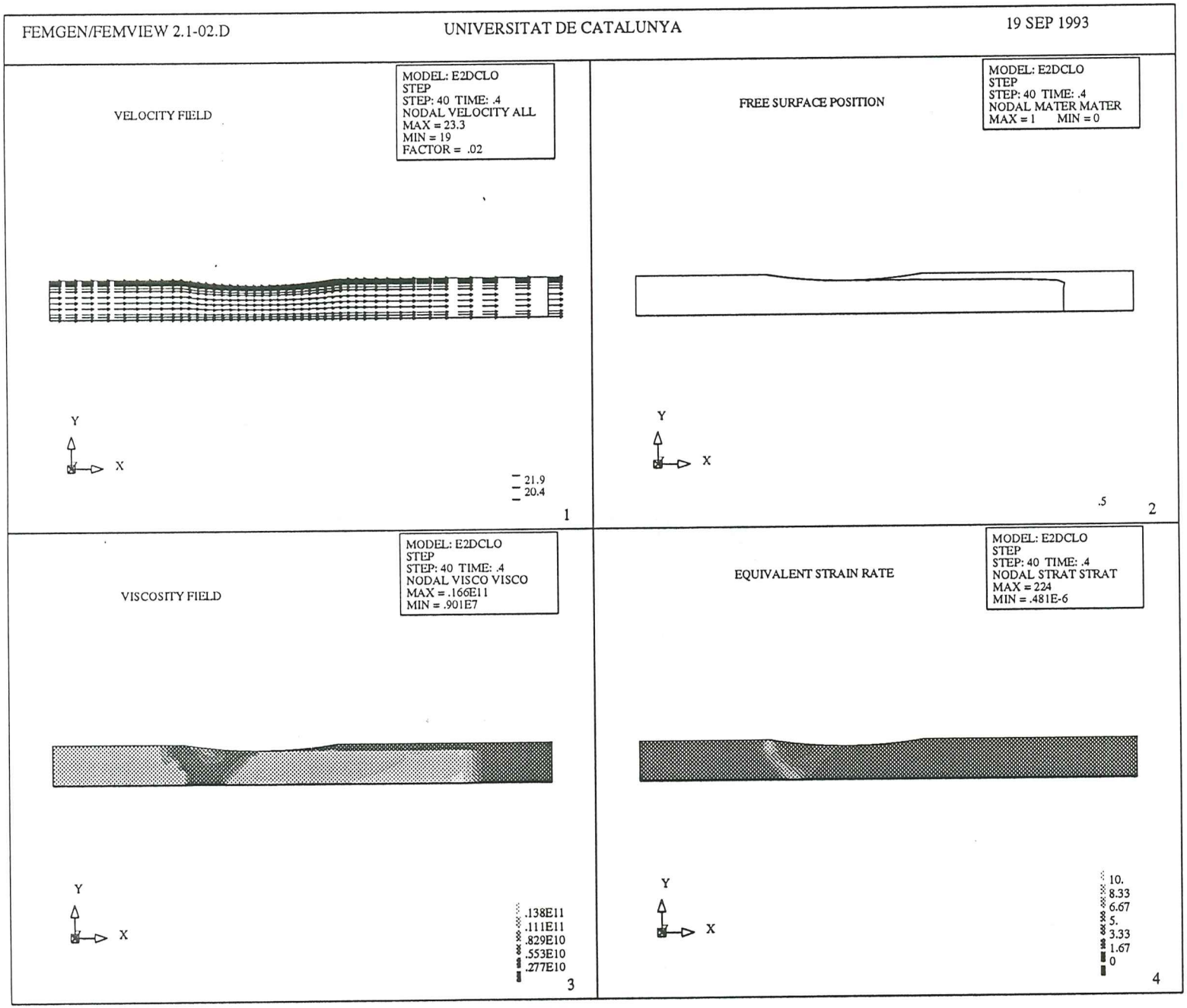

Figure 4.2.5 Velocity field $[cm/s]$, viscosity $[dy \cdot s/cm^2]$ and equivalent strain rate.

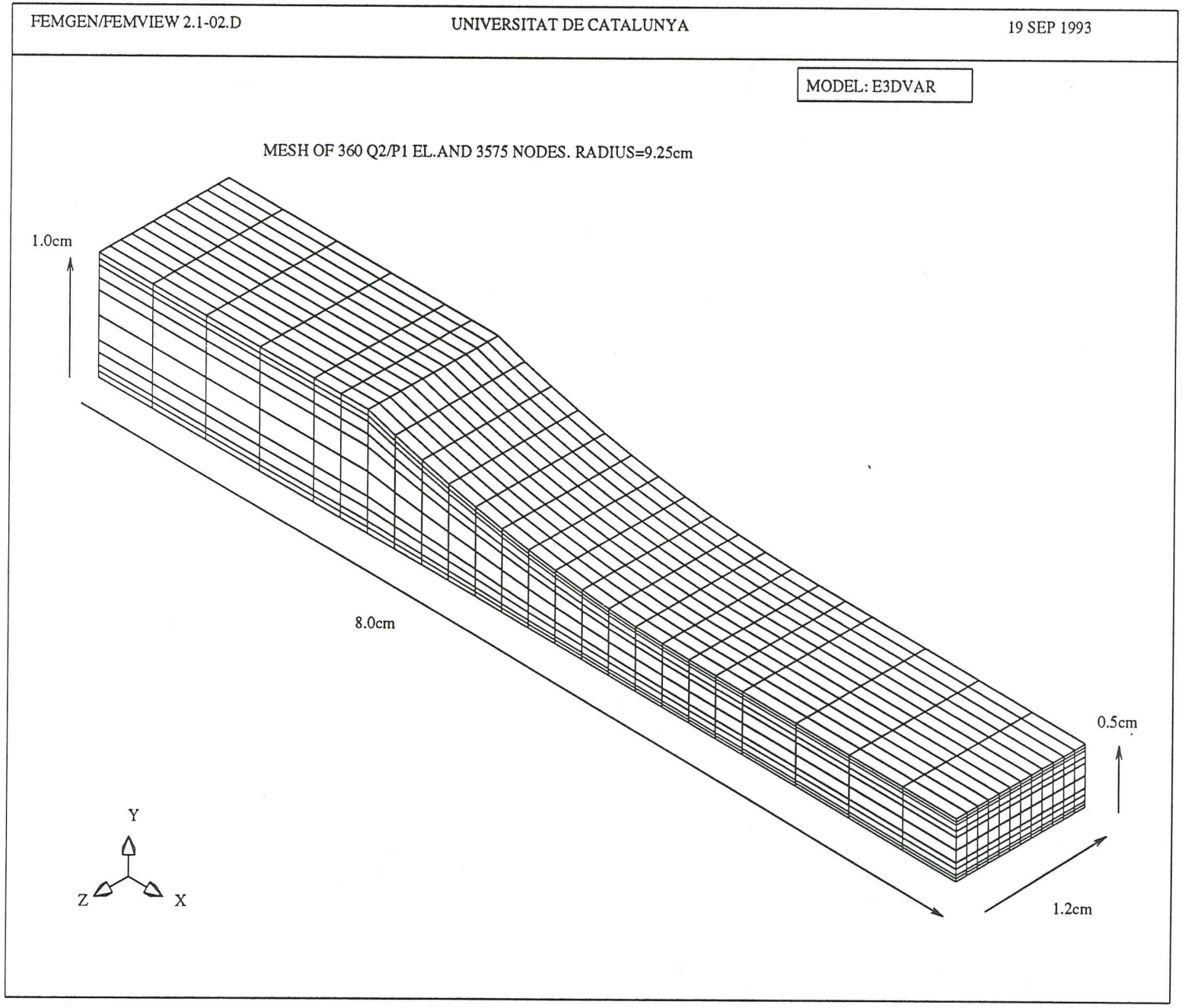

Figure 4.3 Geometry and spatial mesh for Example III.

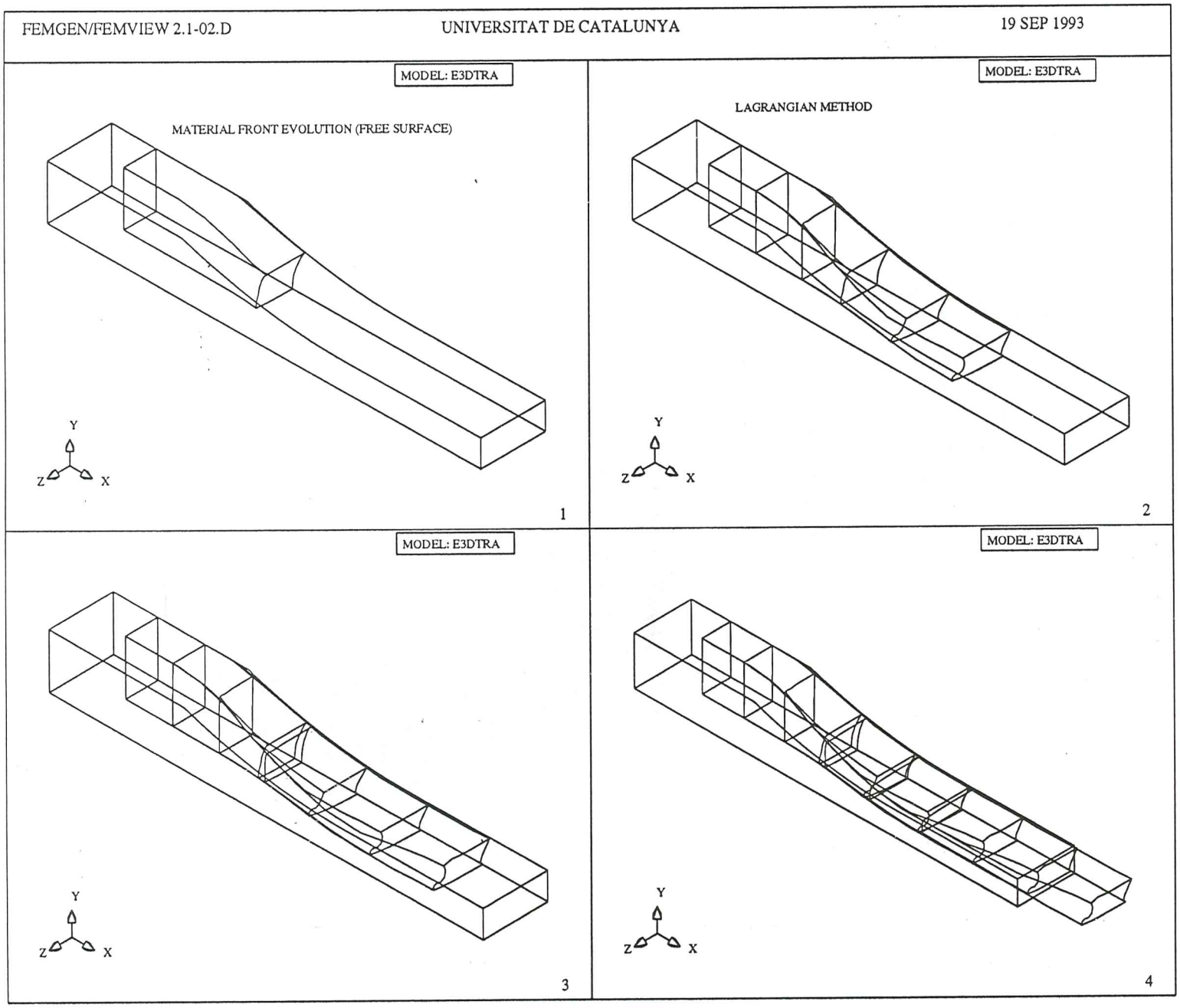

Figure 4.3.1a Free surface with Lagrangian method.

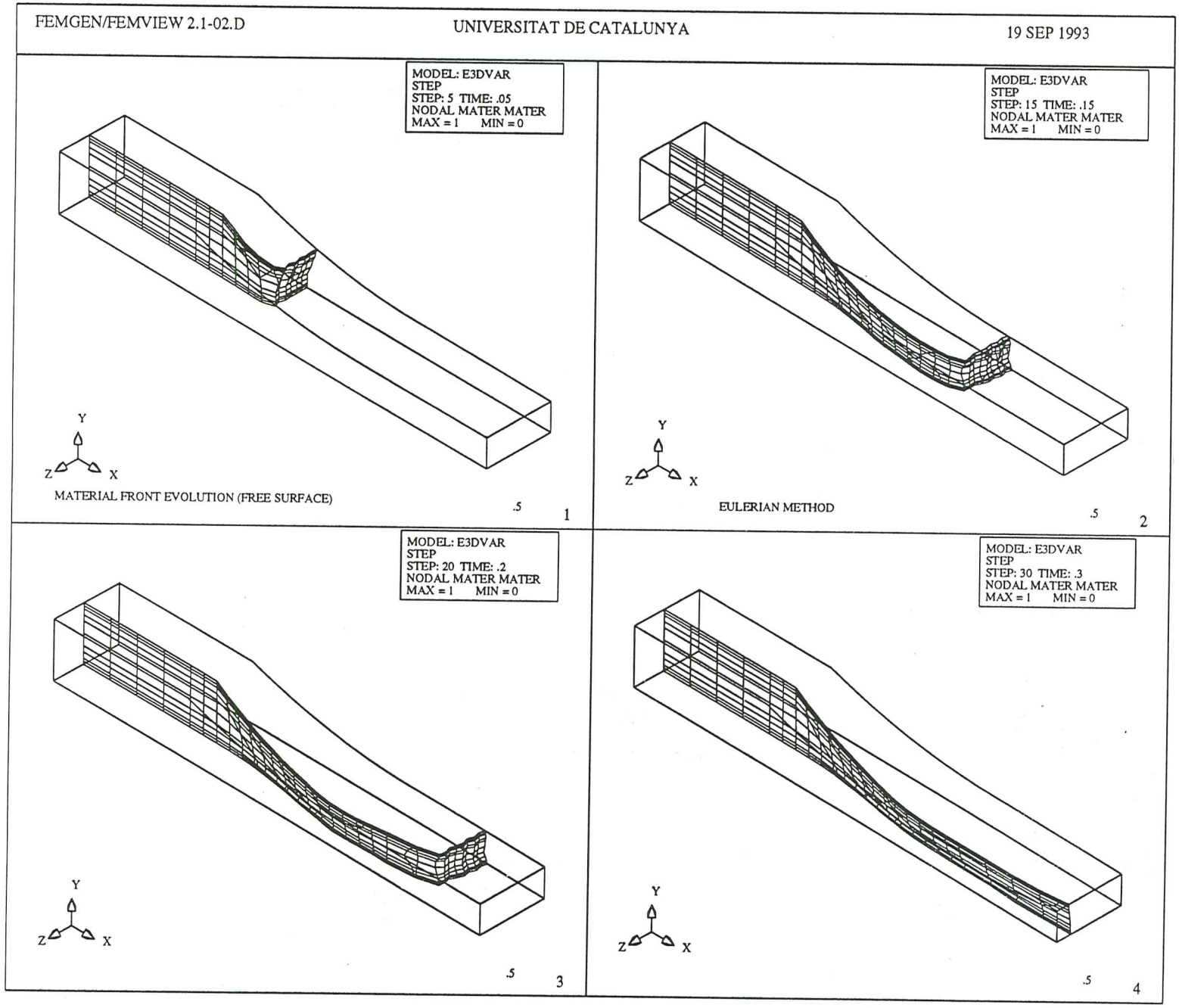

Figure 4.3.1b Free surface with Eulerian method.

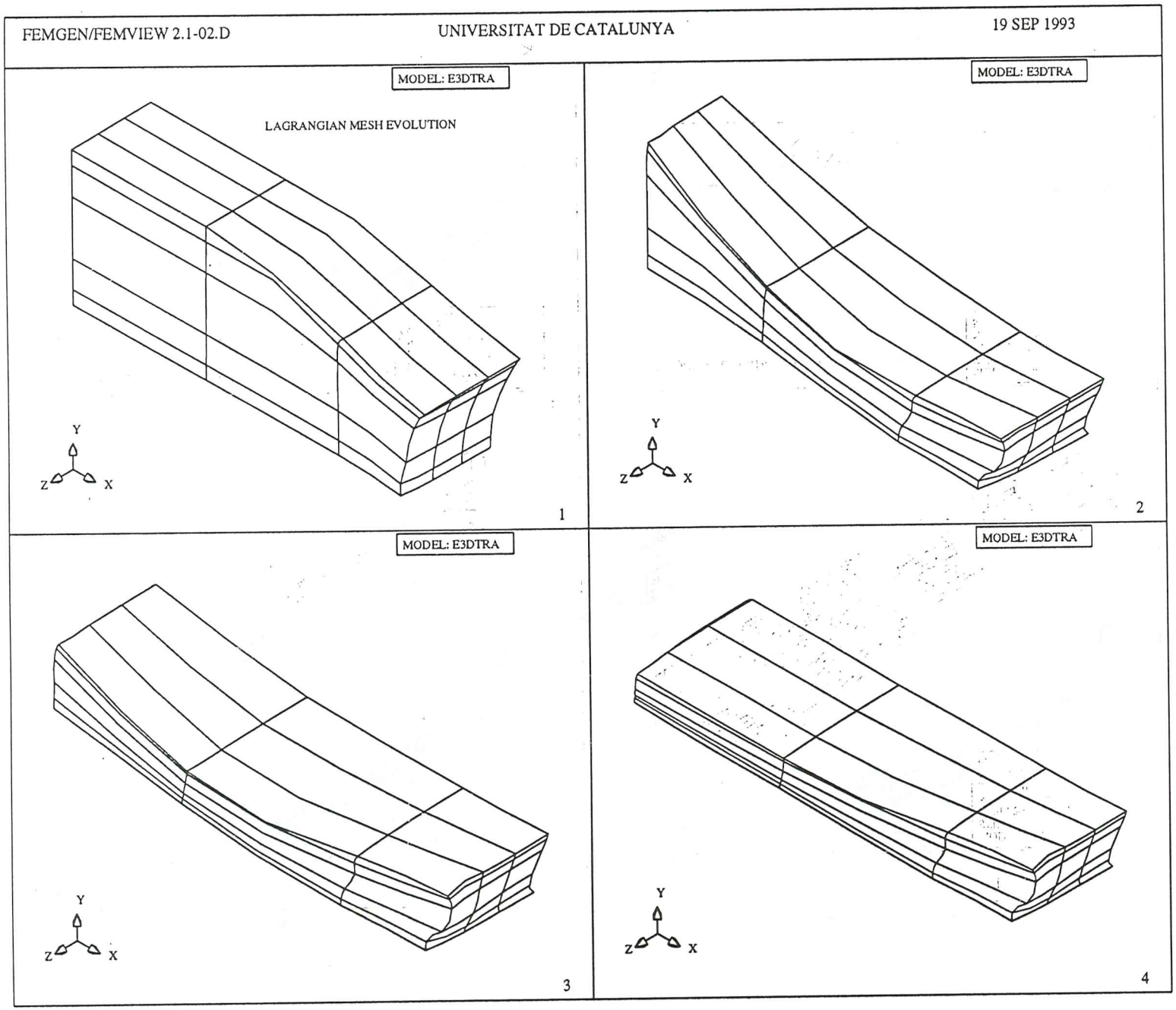

Figure 4.3.1c Lagrangian mesh time evolution.

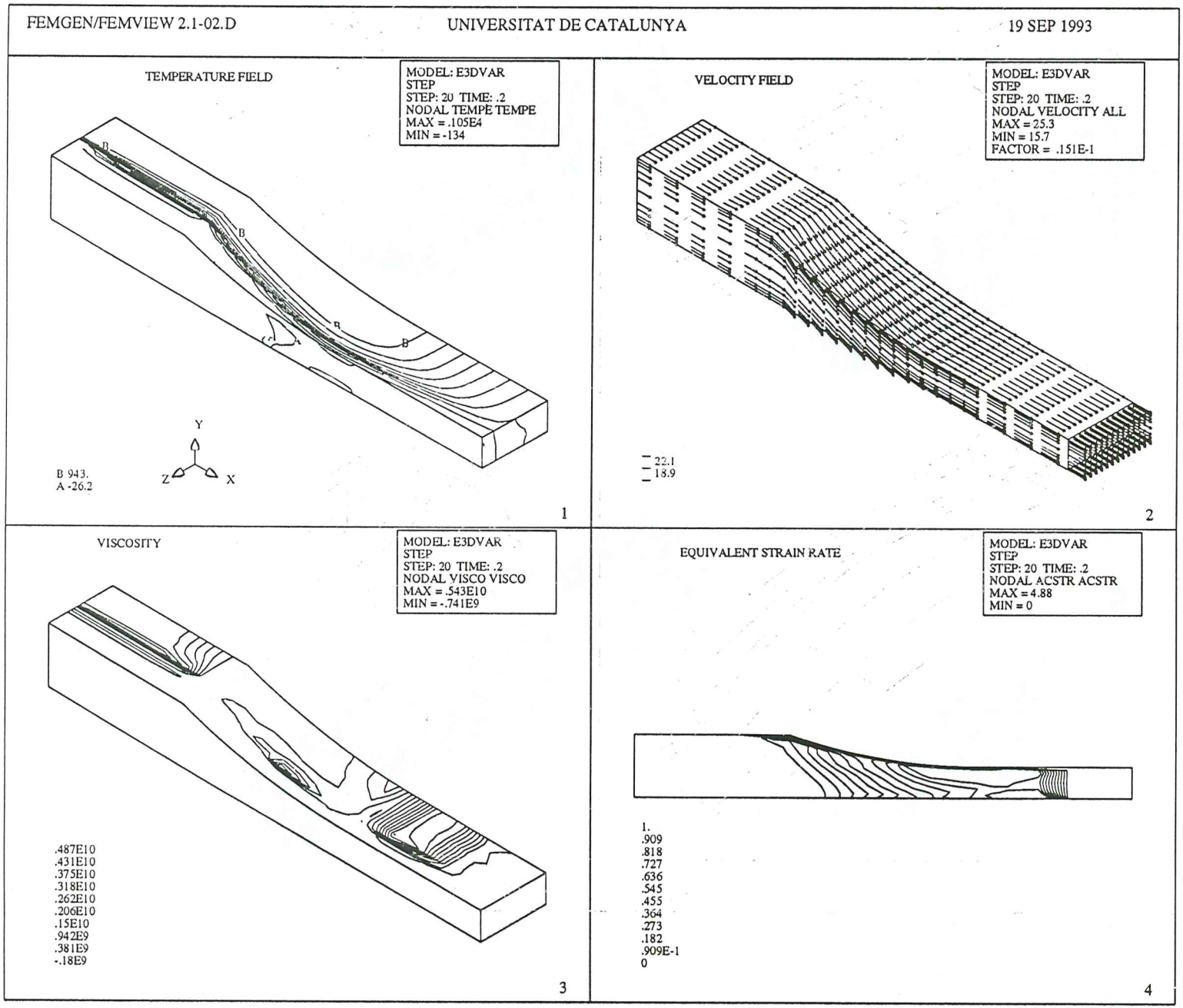

Figure 4.3.3 Temperature $[^{o}C]$, velocity $[cm/s]$, viscosity $[dy \cdot s/cm^2]$ and equivalent strain rate $[s^{-1}]$.

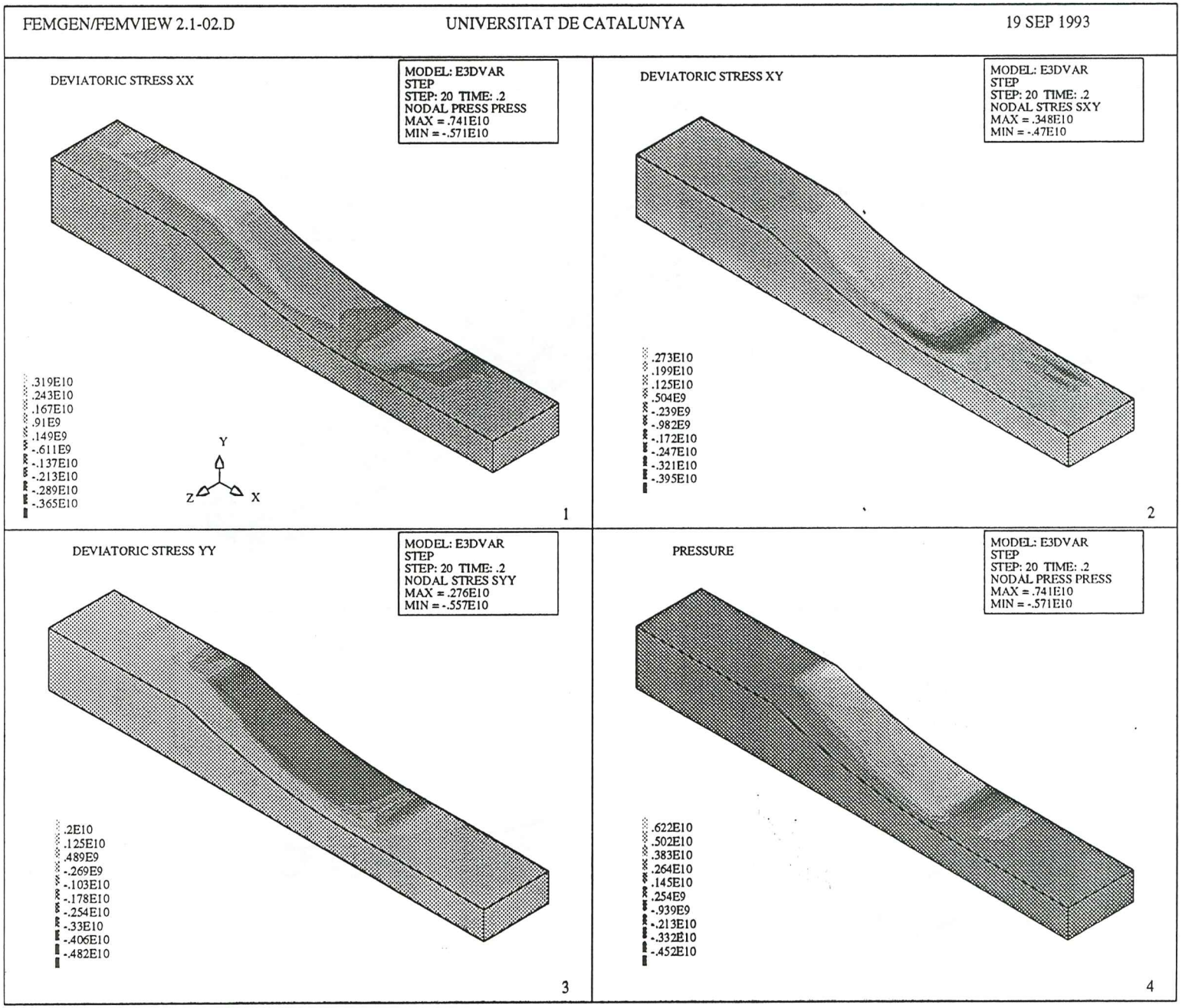

Figure 4.3.2 Stress and pressure fields at roll surface $[dy/cm^2]$.